HZDR

HELMHOLTZ
ZENTRUM DRESDEN
ROSSENDORF

TECHNISCHE UNIVERSITÄT DRESDEN

From 2D CoCrPt:SiO$_2$ films with perpendicular magnetic anisotropy to 3D nanocones
— A step towards bit patterned media —

D I S S E R T A T I O N

zur Erlangung des akademischen Grades

Doctor rerum naturalium
(Dr. rer. nat.)

vorgelegt

an der Fakultät Mathematik und Naturwissenschaften
der Technischen Universität Dresden

von

Dipl.-Phys. David Klaus Ball

geboren am 27. Juli 1974 in München

Die Dissertation wurde eingereicht am 12.11.2012 und verteidigt am 19.04.2013.

Die Dissertation wurde in der Zeit von 01.02.2009 bis 31.08.2012 am Institut für Ionenstrahlphysik und Materialforschung am Helmholtz-Zentrum Dresden – Rossendorf e.V. angefertigt.

Die Arbeit wurde an der Technischen Universtität Dresden am 12.11.2012 eingereicht.

Das Rigorosum und die Disputation fanden an der Technischen Universität Dresden am 19.04.2013 statt.

1. Gutachter:
Prof. Dr. Jürgen Faßbender, Technische Universität Dresden
/ Helmholtz-Zentrum Dresden-Rossendorf e.V.

2. Gutachter:
Prof. Dr. Manfred Albrecht, Technische Universität Chemnitz

dedicated to Mirjam und Joshua

”Why the hell not?”
”How Hard Could It Be?”

Richard S. ”Kinky” Friedman, *11/01/1944 Chicago, Illinois, USA
American Texas Country singer, songwriter, novelist, humorist, politician and former columnist;
Campaign slogans for the governor election of Texas in 2004.

Abstract

Due to the ever-increasing worldwide consumption of memory for digital information, new technologies for higher capacity and faster data storage systems have been the focus of research and development. A step towards achieving higher data storage densities for magnetic recording media is the concept of bit patterned media, where the magnetic recording layer is divided up into magnetically isolated bit units. This approach is one of the most promising technologies for increasing data storage densities and could be implemented by nanostructuring the wafer. Therefore, the fabrication of the appropriate nanostructures on a small scale and then be able to manufacture these structures on an industrial scale is one of the problems where science and industry are working on a solution. In addition, the answer to the open question about the influence that patterning on the nano length scale has on the magnetic properties is of great interest.

The main goal of this thesis is to answer the open question, which magnetic properties can be tailored by a modification of the surface texture on the nanometre length scale. For this purpose the following properties: anisotropy, remanence, coercivity, switching field distribution, saturation magnetisation, Gilbert damping, and inhomogeneous linebroadening were compared between planar two dimensional thin ferromagnetic films and three dimensional magnetic structures. In addition, the influences of the tailored morphology on the intergranular or the exchange coupling between the structures, which is called interdot exchange coupling, was investigated. For the ferromagnetic thin films, the focus of the investigations was on the granular $CoCrPt:SiO_2$ and $[Co/Pd]$ layer, which currently are the state-of-the-art material for magnetic data storage media. These materials are characterised by their high coercivity and high perpendicular anisotropy, which has a low spatial distribution in the preferred direction of magnetisation.

In this work the pre-structured GaSb(001) substrate with self-assembled periodic nanocone structures at the surface are used. The preparation by ion beam erosion of these structures is simple, fast, and highly reproducible and therefore this method is particularly beneficial for fundamental research. To compare the 2D thin films with the 3D magnetic structures, besides the pre-structured specimen, planar samples were also fabricated. The first sample series prepared was coated by Py. Due to the fact that the magnetic properties of this material are well-known, it was also possible to do some OOMMF simulations in addition to the VNA-FMR and MOKE measurements.

Afterwards two planar samples with CoCrPt and $CoCrPt:SiO_2$ were prepared. The planar $CoCrPt:SiO_2$ samples were Co^+ ion implanted to study the influence of such irradiation on the intergranular and interdot exchange coupling, switching field distribution, and in particular on the spin dynamics. Moreover, both samples were measured by TRMOKE in order to obtain information about the spin dynamics.

Subsequently, the perpendicular storage media materials $CoCrPt:SiO_2$ and $[Co/Pd]$ were deposited on a pre-structured GaSb(001) nanocone substrate surface. These sample series were measured by MOKE, SQUID, and vector-VSM. The measurements demonstrate the influence of the periodicity and height of the nanocones on the intergranular and interdot exchange coupling. They also show the reorientation of the magnetisation with respect to the curvature of the substrate template and furthermore, the morphology-induced influences on the magnetic domains.

From the comparison between the results for the planar and the pre-structured samples, a decrease of the interdot exchange coupling was observed, which scales together with the periodicity of the nanocone pattern. In addition, it was shown that for all samples with thin magnetic films on nanocones,the magnetisation aligns along the curvature of the underlying nanocone structure. For Py on nanocones, planar granular $CoCrPt:SiO_2$, and planar granular CoCrPt, measurements by VNA-FMR and TRMOKE could be carried out, which yielded information about the spin dynamics. The results obtained for both of the planar sample are comparable to values from the literature for the Gilbert damping. The results for the Py samples showed that the commonly used 2D model resonance condition is, in case of a 3D magnetic structure, no longer valid due to the alignment of the magnetisation along the underlying substrate structure and therefore an new model has to be derived.

Kurzfassung

Aufgrund des weltweiten, immer weiter steigenden Bedarfs an Speicherplatz von digitalen Information, sind neue Technologien für größere und schnellere Speichermedien im Fokus von Forschung und Entwicklung. Ein Schritt hin zu einer höheren Speicherdichte in der magnetischen Datenspeicherung ist dabei das sogenannte Konzept der "Bit patterned media", das definierte Informationseinheiten auf regelmäßig angeordneten Nanostrukturen beschreibt. Dieser Ansatz ist einer der derzeit vielversprechendsten Optionen die Speicherdichte zu erhöhen. Dabei ist die Herstellung der benötigten Nanostrukturen und deren Skalierung hin zu makroskopischen Dimensionen eines der Probleme an deren Lösung die Wissenschaft und Industrie derzeit arbeitet. Desweiteren ist die Antwort auf die noch offene Frage nach der Beeinflussung der nanoskaligen Strukturen auf die magnetischen Eigenschaften von großem Interesse.

Das Hauptziel in dieser Arbeit ist es, einen Beitrag zur Beantwortung der Frage, welche magnetischen Eigenschaften sich durch eine Veränderung der Oberflächenstruktur im Nanometerbereich beeinflussen lassen, zu leisten. Hierzu wurden die folgenden Eigenschaften, wie zum Beispiel die Anisotropie, Remanenz, Koerzitivität, Schaltfeldverteilung, Sättigungsmagnetisierung, Gilbertdämpfung und inhomogene Linienverbreiterung von planaren zweidimensionalen dünnen ferromagnetischen Schichten mit denen von dreidimensionalen magnetischen Strukturen verglichen. Zusätzlich wurde der Einfluss der angegpassten Morphologie auf die intergranularen- beziehungsweise auf die zwischen den Strukturen wirkende (interdot) Austauschkopplung untersucht. Der Hauptaugenmerk bei den ferromagnetisch dünnen Schichten lag dabei auf den granularen $CoCrPt:SiO_2$ und [Co/Pd] Filmen, die heutzutage ein Standardmaterial für die magnetischen Speichermedien darstellen. Diese Materialien zeichnen sich durch eine hohe Koerzivität und senkrechte Anisotropie, mit geringer räumlicher Verteilung der Vorzugsrichtung der Magnetisierung, aus.

Die hier vorgestellten vorstrukturierten GaSb(001) Substrate mit selbstordnenden periodischen Nanokegeln auf der Oberfläche, sind mittels Ionenstrahlerosion einfach, schnell und sehr gut reproduzierbar herzustellen. Deshalb ist diese Methode besonders für die Grundlagenforschung von Vorteil. Um einen Vergleich zwischen 2D Filmen und 3D Strukturen ziehen zu können, wurden neben den vorstrukturierten Substraten auch planare Proben beschichtet. Eine erste Versuchsreihe wurde mit einem dünnen Py Film präpariert. Da dessen magnetische Eigenschaften wohlbekannt sind, konnten neben den Untersuchungen mit VNA-FMR und MOKE auch einige OOMF Simulationen erstellt werden.

Danach wurden zwei Proben mit planarem CoCrPt beziehungsweise $CoCrPt:SiO_2$ untersucht. Bei den planaren $CoCrPt:SiO_2$ Proben wurden außerdem noch Co^+ Ionen implantiert, um deren Auswirkungen auf die intergranulare Austauschkopplung, Schaltfeldverteilung und besonders auf die Spindynamik zu bestimmen. Bei beiden Probensystemen konnte zusätzlich die Spindynamik mittels zeitaufgelöstem MOKE gemessen werden.

Im Anschluss wurden die beiden senkrechten Speichermedien $CoCrPt:SiO_2$ and [Co/Pd] auf Substraten mit Nanokegeln vorstrukturierten GaSb(001) Oberflächen abgeschieden. Diese Proben wurden mit MFM, MOKE, SQUID und Vektor-VSM vermessen. Aus den Messungen konnnten dann die Einflüsse auf die intergranulare- beziehungsweise interdot Austauschkopplung in Abhängigkeit von der Periodizität und Höhe der Nanokegel bestimmt werden, sowie die Umorientierung der Magnetisierung bezüglich der Substratkrümmung und den Morphologie induzierten Einfluss auf die magnetischen Domänen.

Anhand der Vergleiche zwischen den Messungen der planaren und den vorstrukturierten Proben konnte eine Verringerung der Austauschkopplung zwischen den Strukturen gezeigt werden, die mit der Nanokegelstrukturperiodizität skaliert. Außerdem wurde in allen dünnen magnetischen Filmen auf Nanokegeln gezeigt, dass die Magnetisierung sich in Abhängigkeit der darunterliegenden Struktur ausrichtet. Bei den Py auf Nanokegeln, den planaren CoCrPt und dem planaren $CoCrPt:SiO_2$ Proben konnten außerdem mit VNA-FMR und TRMOKE Informationen bezüglich der Spindynamik gemessen werden. Die erzielten Ergebnisse, der beiden planaren Proben, sind vergleichbar mit denen, aus der Literatur bekannten Werten, für die Gilbertdämpfung. Darüber hinaus wurde durch die Messungen an den Py Proben gezeigt, dass die Theorie, des bisher genutzten 2D Modells, nicht mehr gültig ist, da sich die Magnetisierung entlang der Substratstruktur ausrichtet, und deshalb ein neues Model aufgestellt werden muss.

Contents

Abbreviations and Symbols

$\Delta B^{\text{Gilbert}}$ .... Gilbert damping

$\Delta B_0^{\text{inhom}}$ .... inhomogeneous linebroadening

$\Delta B^{\text{mosaicity}}$ ..... mosaicity

α .... Gilbert damping constant

χ .... susceptibility

ΔB .... FWHM linewidth

ΔB_0 .... inhomogeneous linebroadening

ΔB_{pp} .... peak-to-peak linewidth

ΔE .... energy difference

Δt_{pulse} .... pulse duration

γ .... gyromagnetic ratio

$\hbar$ .... reduced Planck constant

λ .... wavelength

μ_{B} .... Bohr magneton

Ω .... diffusion jump rate

ω .... angular velocity, $\omega = 2\pi f$

$\theta, \theta_{\text{H}}$ .... polar angles

$\tilde{\varepsilon}$ .... dielectric tensor

$\varphi, \varphi_{\text{H}}$ .... azimuth angles

φ_{u} .... uniaxial azimuth angles

$\vec{h}_{\text{rf}}$ .... microwave magnetic field

$\vec{J}$ .... total angular momentum

$\vec{L}$ .... orbit angular momentum

$\vec{n}$ .... normal vector of film plane

$\vec{S}$ .... spin angular momentum

B .... magnetic flux density, magnetic induction

$E_{\text{diffusion}}$ .... diffusion activation energy

E_{exc} .... exchange energy

E_{kin} .... kinetic energy (of sputtered ions)

E_{pulse} .... pulse energy

E_{QH} .... energy of the quasi-homogeneous state

E_{tot} .... total energy

E_{vls} .... energy of the vortex-like state

f .... frequency

$f_{\text{diffusion}}$ .... diffusion probability frequency

F_{L} .... Lorentz force

H .... magnetic field strength

h .... Planck constant

H_{eff} .... effective magnetic field

H_{ext} .... external magnetic field

J^{ex} .... exchange integral

K .... anisotropy

K_{eff} .... effective anisotropy

K_i .... anisotropy constant

l_{c} .... characteristic length

$L_{\text{fit}}(B)$ .... Lorentzian fit function

M .... magnetic moment, volume magnetisation

M_{r} .... remanence

$M_{\text{r}}/M_{\text{s}}$ .... normalized remanence

M_{s} .... saturation magnetisation

$M_{\text{s}}(H)$ .... hysteresis loop

p .... momentum

p .... pressure

R_{rep} .... repetition rate

T_{c} .... Curie temperature

Z .... atomic number, number of protons

2D .... two dimensional

3D .... three dimensional

Å .... Angström $\hat{=} 10^{-10}$ m

g-factor .... Landé factor

A .... Ampére

AFM .... atomic force microscopy

azimuthal .... angle in the surface plane

bcc .... body-centred cubic

BPM .... bit patterned media

CCD .... Charge-coupled device

CFT .... crystal field theory

Co .... Cobalt

CoCrPt:SiO$_2$ .... Cobalt Chromium Platinum Silicondioxide

Cr .... Chromium

CS .... cross-sectional

DC .... direct current voltage

DDI .... dipole-dipole interaction

DPG .... Deutsche Physikalische Gesellschaft

EM .... electromagnetic

emu .... magnetic moment

emu/cm^3 .... cgs-unit for the volume magnetisation

eV .... electron volt

fcc .... face-centred cubic

fct .... fcc tetragonally distorted

Fe .... Iron

FIB .... focussed ion beam

FM .... ferromagnetic

FMR .... ferromagnetic resonance

FWHM .... full width half maximum

FWIN . . . . department of magnetism

G . . . . cgs-Gauss, unit for the volume magnetisation

Ga . . . . Gallium

GaSb . . . . Gallium-Antimony

GUI . . . . graphical user interface

HAMR . . . . heat-assisted magnetic recording

hcp . . . . hexagonal closed-packed

HDD . . . . hard disc drives

hex . . . . hexagonal

HGST . . . . Hitachi Global Storage Technologies

HR . . . . high resolution

HZDR . . . . Helmholtz-Zentrum Dresden–Rossendorf e.V.

IEEE . . . . institute of electrical and electronics engineers

IET . . . . ion beam erosion technique

IIM . . . . institute of ion beam physics and materials research

ILB . . . . inhomogeneous linebroadening

ip . . . . in-plane

KR . . . . Kerr rotation

LL . . . . Landau-Lifshitz equation

LLG . . . . Landau-Lifshitz-Gilbert equation

LMOKE . . . . longitudinal magneto-optical Kerr effect

LMR . . . . longitudinal magnetic recording

m . . . . milli $\widehat{=} 10^{-3}$

MAE . . . . magnetic anisotropic energy

mbar . . . . millibar

MBE . . . . molecular beam epitaxy

MFM . . . . magnetic force microscopy

ML . . . . monolayer

MOKE . . . . magneto-optical Kerr effect

MS . . . . magnetron sputtering

NI . . . . national instruments

Ni . . . . Nickel

NIST . . . . National Institute of Standard and Technology

nm . . . . nanometer

O . . . . Oxygen

Oe . . . . cgs-unit: Oersted

OOMMF . . . . object oriented micromagnetic framework

oop . . . . out-of-plane

PCF . . . . pair correlation function

PMOKE . . . . polar magneto-optical Kerr effect

PMR . . . . perpendicular recording media

polar . . . . angle between surface normal and surface plane

ps . . . . picoseconds

Pt . . . . Platinum

PVD . . . . physical vapour deposition

QH . . . . quasi-homogeneous

Sb . . . . Antimony

SEM . . . . scanning electron microscopy

SFD . . . . switching field distribution

Si . . . . Silicon

SiO_2 . . . . Silicondioxide

SNR . . . . signal-to-nois ratio

SOI . . . . spin-orbital interaction

SQUID . . . . superconducting quantum interference device

SRIM . . . . stopping and range of ions in matter, simualation package

SUL . . . . soft magnetic underlayer

T . . . . Tesla

TEM . . . . transmission electron microscopy

TMOKE . . . . transversal magneto-optical Kerr effect

TR . . . . time-resolved

TRIDYN . . . . TRIM simulation code including dynamic composition changes

TRIM . . . . transport of ions in matter, simulation package

TRMOKE . . . . time-resolved magneto-optical Kerr effect

TU . . . . technical university

V . . . . Volt

VFP . . . . vector field plot

VNA . . . . vector network analyser

VNA-FMR . . . . vector network analyser ferromagnetic resonance

VSM . . . . vibrating sample magnetometry

vVSM . . . . vector vibrating sample magnetometry

W . . . . Watt

Chapter 1.

Introduction and Motivation

Nowadays, due to the ever increasing demands of memory usage in information technology, digital data storage requires a simultaneous increase of density and decrease of access time [see Fig. 1.1(a)]. New ways must be found to improve and adapt the current data storage technologies to the future demand of the consumers. Currently, many of the digital data storage systems available are based on a magnetic data storage medium, such as a thin film of ferromagnetic material, and so the physics of magnetism plays a part in developing this technology. The aim of this thesis is to provide a contribution to the fundamental understanding of the physical processes of morphology-induced effects on the magnetic properties of thin films. These properties are strongly affected by the surface morphology.[1–3] In particular, we study the evolution of effects arising from the transition from a planar 2D ferromagnetic film to 3D magnetic structures (nanocones). This transition could be a crucial point in the improvement of data storage technologies.

The introduction of perpendicular magnetic recording (PMR) media improved storage density over the former longitudinal recording media (LMR) by a factor of at least three and its development has lasted for three decades [see Fig. 1.1(b)].[4] Currently, commercial hard disc drives use a continuous granular PMR media with multiple grains per bit, where an individual grain has a diameter of about $6-8$ nm and one bit is approximately 20 nm long and 100 nm wide [see Fig. 1.2(b)].[1] The boundaries between the bits are determined by the grain boundaries which contain a segregating oxide. Compared to the longitudinal magnetic recording (LMR) media used previously, where the easy axis of magnetisation lays in-plane and the material is magnetically weaker, the data storage density is significantly higher for PMR media compared to LMR media due to the smaller bits and the higher coercivity. A brief summary of the advantages of the PMR media are described as follows:[5]

(a) The pole-head/SUL configuration has a field twice as large as that given by the ring head previously use. This higher field enables the use of ferromagnetic media with higher anisotropy K_u and higher coercivity. Therefore it is possible to make use of granular media (switching units) of a smaller volume, which leads to an increase of the storage density.

(b) The sharp transition between the bits supports the application of thick media. The usage of thicker media enables the areal density to be increased whilst maintaining the volume of the bits, and thus an increase the storage density without comprimising the thermal stability of the system.

(c) PMR media have a strong uniaxial orientation of magnetisation compared to LMR media wich has a random in-plane orientation. Therefore the switching field distribution (SFD) is decreased which allows a sharper written transition. Furthermore, well-defined oriented media are tantamount to achieving a higher signal and a lower noise.

The read heads of hard disc drives (HDD) detect the stray field from the magnetic bits. The scheme of a

---

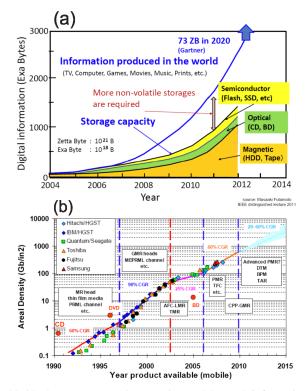[1] Talk of Dr. Olav Hellwig, HZDR e.V., 10/30/2011

Fig. 1.1 (a) Graph of the worldwide data storage supply (capacity) and demand (information produced) from 2004 up to 2012. (b) Graph of the increase of data storage areal density from 1990 to 2015. The data points represent the milestones of the different industrial data storage companies. As well as, the different technologies which have allowed these milestones to be reached. Adapted from the talk of Dr. Olav Hellwig (Hitachi GST), HZDR e.V., 10/30/2011.

current design for a PMR based HDD with a read/write head is shown in Fig. 1.2(a). An important part of the writing system is the SUL which concentrates the flux under the pole-tip where it generates a high intensity magnetic field in the gap between the tip and the SUL. Therefore, within this gap the highly intense magnetic field directly acts on the recording layer, i.e. $CoCrPt:SiO_2$. The higher write field leads to the means to use magnetic materials with a higher coercivity and anisotropy. In such a highly coercive media the magnetisation requires on the one hand a higher switching field but on the other hand the magnetisation is inherently more stable. Moreover, due to the SUL, the read back signal is amplified and in addition decreases the interference from adjacent bits.[6–13]

The state-of-the-art PMR material is a magnetron sputtered weakly exchange coupled granular $CoCrPt:SiO_2$ film on top of a stack consisting of a dual-Ru layer, seed layer, SUL, and a adhesion layer deposited on a glass wafer [see Fig. 1.2(b)]. Typically the entire stack is capped by a carbon layer to avoid further oxidation. The enhanced intergranular exchange decoupling is achieved by the addition of a segregating SiO_2 to the CoCrPt alloy. The $CoCrPt:SiO_2$ grows in columns on top of a stack of several layers, which will be briefly introduced from the top to the bottom in the following.

The first underlayer typically consists of a dual-Ru intermediate growth layer. This approach achieves a well-defined c-axis orientation of the $CoCrPt:SiO_2$ recording layer as well as improved macro-magnetic properties. The first Ru layer below the recording layer was deposited at a high working gas pressure, which leads to a lower mobility of the Ru atoms during deposition, this deposition condition improves the isolation of the grain morphology. This is necessary for an improved coercivity and a larger negative nucleation field. Whereas the second Ru layer beneath, was prepared at a lower working gas pressure and therefore with a higher mobility of Ru atoms during deposition. The benefit from this process step is a well-defined crystalline

texture. Due to the presence of the Ru layer the CoCrPt grows with a hcp structure, where the easy axis of magnetisation points along the (0001)-direction (c-axis) and therefore the magnetisation easy direction is subsequently out-of-plane. The lattice mismatch of 7.3 % (Ru: $a = 2.70389$/Co: $a = 2.5074$[14]) induces the hcp growth due to the lattice strain. The lattice mismatch is therefore crucial to obtain a high perpendicular anisotropy.[15,16] Furthermore the dual-Ru intermediate layer leads to an improved signal-to-noise (SNR).[13] Another function of the dual-Ru layer is to exchange decouple the magnetic recording layer on top from the SUL below. Below the Ru layer an additional intermediate seed layer with a crystallographic texture of hcp(0001), fcc(111), or bcc(110).[17–22] is used to support the epitaxial growth of the Ru. Currently, beneath the growth underlayer and the intermediate seed layer a SUL is prepared which is needed to conduct the magnetic flux of the read/write head. Between the SUL and the carrier substrate (i.e. a glass carrier) another layer is usually deposited as a seed layer to improve the adhesion to the glass carrier substrate.

Usually the entire recording media stack of a conventional HDD stack is more than 40 nm thick. The entire stack has to be optimised for recording on the following three items: the signal-to-noise ratio (SNR), the thermal stability, and the writing field [see Fig. 1.2(c)]. As has been discussed in the literature, both the thermal stability and the writing field, given by K_{eff}, depend on the grain size.[23] The SNR can be improved by decreasing the grain diameter, but this also reduces the thermal stability and if taken too far this leads to superparamagnetism. This takes place, when the energy associated with the anisotropy barrier ($K \cdot V$) becomes comparable to the thermal energy ($k_{\text{B}}T$), this is referred to as the superparamagnetic limit and is the point where the magnetic grains in a material are subject to random thermal fluctuations during the lifetime of the product which leads to data loss.[24,25] Increasing K gives a better stability but then larger fields are required to switch the magnetisation. Thus, a balance should be found between the three parameters (i.e. thermal stability, SNR, and writing field) given above. In this thesis we focus on the investigations of the magnetic properties of the PMR media, issues regarding the writing field will be not discussed.

We have investigated the magnetic reversal behaviour, the switching field distribution and the spin dynamics of granular CoCrPt:SiO$_2$ films and [Co/Pd] multilayers ([Co/(Pd,Pt)] and CoCrPt:SiO$_2$ have a high perpendicular anisotropy[26–31]). We will show that due to the granular nature of the ferromagnetic material, the collective phenomena of intergranular- and/or interdot exchange coupling influences the magnetic reversal process. The interdot exchange coupling is an additional complexity, which appears due to the fact that the pre-structured samples are no longer a simple 2D film, as will be shown in this work. This interdot exchange coupling is defined by the underlying template length scale. Moreover, the curvature of the structure affects the interdot- and the intergrain exchange coupling and the anisotropy distribution. In this thesis, changes of the magnetic properties due to the variation of the length scale of the template pattern will be investigated. The intergrain exchange coupling can be tailored, on the one hand by the SiO$_2$ content in the CoCrPt alloy or on the other hand by ion implantation into the CoCrPt:SiO$_2$ layer. Within this work, former investigations of ion implanted planar, granular CoCrPt:SiO$_2$ films will be extended by investigation regarding the spin dynamics.[32]

Since PMR media for hard disc drives was introduced to the market in 2005, the technology has steadily developed and has almost reached the superparamagnetic limit [see Fig. 1.1(b)] a new approach has to be sought in order to achieve a higher data storage density. One first step was to tailor the intergrain exchange coupling by ion implantation.[32–35] A new approach currently under investigation is heat-assisted magnetic recording (HAMR), where the media is locally heated close to the T_c and thus, the switching of highly anisotropic particles can be achieved with low fields.[36,37] A possible further method is to use discrete isolated magnetic bit units, this concept is called bit patterned media (BPM).[38–45] The drawback of PMR media is that the grains are randomly arranged, so in order to define a bit many individual grains have to be used. In this type of media the grains have to be isolated, so that the bits a properly separated, which means

Fig. 1.2 (a) Scheme of a perpendicular recording system on a current hard disc drive. (b) plane transmission electron microscopy (TEM) image of a triple magnetic layer medium (CoCrPt:SiO$_2$) (adapted from Takenoiri[47]). The false coloured regions represent exemplarily a bit unit. (a) Triangle of the three parameters in a recording media, which have to be optimised (balanced).

the thermal stability is defined by the grain volume. In BPM, there may be multiple grains per unit, but these grains can be coupled because each bit unit is an magnetically separate structure acting as a single domain particle. Thus, the thermal stability is determined by the volume of the entire bit in contrast to the PMR where this is defined by the grains.

The size of the bits and their locations are determined by the preparation method, for instance optical or electron beam lithography.[38] Electorn beam lithography is only suitable for samples for fundamental research and for preparation of templates due to the long preparation time of this technique. Another promising candidate for future application in the BPM preparation might be nanoimprint lithography.[46] For BPM the dimensions of the bit and the material are chosen to yield a thermally stable magnetic unit. Therefore, by reducing the dimensions of the pattern an increase of the storage density is achievable. Here, investigations are presented of media on self-assembled nanostructured GaSb(001) which should be a step toward the BPM.

BPM requires accurately positioned bits in an ordered array that can be addressed by a read/write head. Currently, several methods are being investigated to find a fast and easy to produce surface patterning on the nano length scale.[48] Considerable efforts have been dedicated to fabricating ordered arrays of magnetic nanostructures using various lithography techniques[49] including nanoimprint approaches.[50] However, these methods are multistep, expensive, and involve time-consuming procedures. Other ways to produce patterned templates are self-assembly techniques such as anodisation,[51] electro-assisted deposition,[52] evaporation-induced-self-assembly associated to liquid deposition,[53] phase separation in block co-polymers,[54] self-assembled magnetic particles,[55] or surface instability induced by ion bombardment.[56] In this thesis the latter ion erosion technique to produce a substrate with patterns of nanocones.

The magnetic response of thin films fabricated on such templates is strongly affected by the surface morphology, such as the local surface curvature.[1] These curvature effects result in a substantial modification of the magnetization reversal behaviour of individual magnetic nanostructures.[57] On the one hand, curvature-driven changes can be beneficial in reducing the switching field, which is advantageous
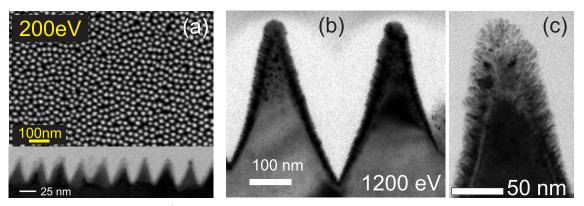
Fig. 1.3 (a) SEM image of an Ar$^+$ ion eroded GaSb(001) substrate surface at an energy of $E = 200$ eV. Below the corresponding TEM image of this nanocone structure is shown. (b) TEM image of two nanocones prepared with an energy of $E = 1200$ eV and coated with CoCrPt:SiO$_2$ on top. (c) Magnification of the TEM image in (b), where the growth of the granular structure is shown with respect to the local curvature.

for magnetic recording applications. However, for films with perpendicular magnetic anisotropy, where the anisotropy lies along the local film normal, curvature might result in a tilt of the grain-averaged easy axis of magnetization, which may tend to follow the geometry of the nanostructured surface. This tilt might be considered as an additional source of noise in media, which has to be minimised.

In this work we want to make a progressive step towards the fundamental understanding of curvature driven changes in the magnetic properties of 3D magnetic films. For this purpose, GaSb nanocone templates were used, which were created from GaSb wafers by ion beam erosion [see Fig. 1.3] and this fabrication method is detailed in the following chapter. [58] This ion beam erosion technique provides a rather fast and easily reproducible way to prepare periodic nanostructures. The ions form a cone-like structure on the substrate surface with a periodicity, width and height which are typically on the nanometre length scale. The cones have an irregular long-range order, however, if higher sputter energies are used then in the short-range regime a hexagonal order is observed. Such order is sufficient for our study of the morphology-induced effects.

To analyse the differences between the measured magnetic parameters such as coercivity, anisotropy, remanence, switching field distribution, Gilbert damping, and inhomogeneous linebroadening, for 2D planar samples and 3D magnetic structures, we prepared the following samples:

- One planar reference sample of GaSb(001) / Cr (5 nm)/Py (20 nm)/Cr (3 nm) thin film and six different pre-structured GaSb/Cr (5 nm)/Py (20 nm)/Cr (3 nm) thin film samples with increasing periodicity of the nanocones;
- Two planar granular CoCrPt films with a different saturation magnetisation deposited on a glass wafer;
- One planar granular CoCrPt:SiO$_2$ reference sample and a variation of eighteen planar granular CoCrPt:SiO$_2$ samples with increasing fluence of ion implanted Co$^+$ deposited on a glass wafer;
- Three different GaSb(001)/granular CoCrPt:SiO$_2$ samples with increasing nanocone periodicity;
- Three different GaSb(001)/[Co/Pd] multilayer film samples with increasing nanocone periodicity.

For the sample series of the Py on nanocones OOMMF simulations were performed to confirm the results obtained. The magnetic characterisation for the samples was carried out by several magnetometry techniques, including ferromagnetic resonance and time-resolved magneto-optical Kerr effect. To investigate the structure of the samples, we used scanning- and transmission electron microscopy.

Chapter 2.

Fundamentals: Theory and Experimental Methods

In this thesis the effects of morphology-induced and ion implantation changes on the properties of ferromagnetic thin films are discussed. A special focus is on recording media like the granular CoCrPt:SiO$_2$ and on [Co/Pd] multilayers. The investigations study the changes in anisotropy, g-factor, remanence, coercivity, damping, switching field distribution, and saturation magnetisation due to the tailored surface structure and the intermixed crystalline film structure. In this chapter the latter concepts will be described first. Afterwards the techniques which were used in the experiments, will be briefly introduced.

2.1. Fundamental Theory

Ferromagnetism is a collective phenomenon which shows a spontaneous magnetisation produced by the parallel alignment of elementary permanent magnets (i.e. spins or magnetic moments).[59,60] The alignment of the spins is due to the exchange coupling between them. Thermal excitation exerts a randomly flucating torque onto the individual spins which has the effect to disorder the spin system. The Curie temperature defines the point where the thermal excitation dominates over the exchange coupling. Below the Curie temperature[61] (T_c) an alignment of the spins exists without an applied external magnetic field, above T_c a paramagnetic behaviour is observed.[62] At room temperature the four elements Iron (Fe), Cobalt (Co), Gadolinium (Gd), and Nickel (Ni) show a ferromagnetic order.[63]

On a microscopic length scale the exchange coupling is usually the dominating energy term, as a consequence of this the spins tend to aligned locally. Whereas on the macroscopic length scale, other energies terms which do not drive a parallel alignment of the spins compete with the exchange coupling. Thus, the spins tend to form domains within the magnetisation is uniform but between them the magnetisation can point in different directions.[1] In nanostructured systems it is common to have small regions which are magnetically decoupled from each other, as a consequence in each of this regions all of the spins are aligned due to the dominance of the exchange energy. This is referred to as a single domain particle. Within the single domain particle due to the alignment of all spins, one can approximate all the magnetic moments by a single net moment of fixed magnitude size. The saturation magnetisation is referring to the to such a situation where all spins are aligned in one direction. In a macroscopic system because the domains can point into different directions, the net moment can be any magnitude between zero and saturation magnetisation.

---

[1] Magnetic domains (also called Weiss domains) dominate the properties of ferromagnets, they form regions, wherein the magnetic moments are coupled. Therefore, the entire spins are aligned parallel, which leads to a uniform magnetisation within the domains. Typically, the alignment of the single domains is trying to reduce the stray field of the shape. The regions separating domains are called domain walls. In these areas a coherent rotation of spins is observable. The underlying theory was developed by Pierre Weiss and can be found elsewhere.[64]

2.1.1. Ferromagnetic Interactions and Energies

Four main interactions have to be considered in a typical ferromagnetic system, which are the following:

- The Zeeman energy describes the interaction between each spin and an external magnetic field;
- The dipole-dipole energy describes the interaction between spins via their dipole fields which give sensitivity to the shape of the sample;
- The exchange coupling energy which was discussed in the previous section describes the interaction between spins
- The spin-orbital energy describes the interaction betwenn spins with their atoms which gives a sensitivity to the crystal structure of the sample.

Niels Bohr has proved that the ferromagnetic phenomena on the atomic scale cannot be described within the classical picture. [65,66]

Zeeman Energy   The Zeeman energy is the potential energy of a magnetised sample inside an external magnetic field. This energy is a function of the direction in which $\vec{M}$ points. The energy term is minimised by the parallel alignment of $\vec{M}$ with $\vec{H}_{ext}$ The energy is described by

$$E_{\text{Zeeman}} = - \int_V \vec{M} \cdot \vec{H}_{\text{ext}} \partial V \tag{2.1}$$

Dipole-Dipole Interaction   The long-range dipole-dipole interaction (DDI) is contributing to both the microscopic behaviour of the magnetocrystalline anisotropy (see 2.1.2), as well as contributing to a macroscopic phenomenom called shape anisotropy (see 2.1.2). The DDI is described by the following Hamiltonian

$$\mathscr{H}_{\text{DDI}}(\vec{r}_{ij}) = - \sum_{i<j} \vec{\mu}_i \cdot \vec{H}_j = \frac{1}{4\pi \vec{r}_{ij}^3} \sum_{i<j} \left((\vec{\mu}_i \cdot \vec{\mu}_j) - \frac{3}{r_{ij}^2}(\vec{\mu}_i \cdot \vec{r}_{ij})(\vec{\mu}_j \cdot \vec{r}_{ij}) \right). \tag{2.2}$$

Due to the fact that in case of solids the atoms are regularly assembled in a lattice, thus the spins are also fixed into said lattice. The vector $\vec{r}_{ij}$ in the latter equation represents the relative position of any two spins within the lattice, and so this energy term is sensitive to the lattice structure. As a consequence in terms of minimizing the energy the orientation of the spins with respect to the lattice is important, this gives rise to an anisotropy effect. This anisotropy effect is minor compared to the SOI, which is discussed below, by an amount determined by the lattice vector $\vec{r}_{ij}^{\,3}$.

In addition, to the microscopic effect the DDI also has a macroscopic impact. This effect is described by classical magnetism, which normally is describes the effect in terms of the diagram (see Fig. 2.1). [67–69] This behaviour results in a so-called demagnetizing field $\vec{H}_{\text{dem}}$, which points in the counter direction of $\vec{H}_{\text{ext}}$. The energy in this system is mathematically expressed by the integral over the product of $\vec{M}$ and $\vec{H}_{\text{dem}}$

$$E_{\text{dem}} = \frac{1}{2} \int_V \vec{M} \cdot \vec{H}_{\text{dem}} \partial V. \tag{2.3}$$

Exchange Coupling Interaction   The long-range parallel orientation of nearest neighbouring magnetic moments mentioned in the previous section requires a strong force to stabilize this state. [62,70] The cause of such strong forces is described by a strong interaction of these moments. The first quantum mechanical treatment of the exchange interaction was published by Werner Heisenberg. [66] The relevant part (exchange

interaction) of the Heisenberg-Hamiltonian is defined by:

$$\mathscr{H}_{\text{ex}} = -2J_{\text{ij}}^{\text{ex}} \sum_{\text{i}>\text{j}}^{\text{N}} \vec{S}_{\text{i}} \cdot \vec{S}_{\text{j}}. \tag{2.4}$$

This general Heisenberg-Hamiltonian $\mathscr{H}_{\text{exchange}}$ includes the summation of all atomic spins ($\vec{S}_{\text{i}}$, $\vec{S}_{\text{j}}$), as well as the exchange integral J_{ex}.[71,72] In the case $J_{\text{ex}} > 0$ ($\vec{S}_{\text{i}} \parallel \vec{S}_{\text{j}}$) it represents the ferromagnetic alignment. Despite this exchange interaction being short-range it can lead to a complete parallel alignment of the entire spin system. Moreover, J_{ex} has a magnitude of 10^3 cm^{-1}, which is four magnitudes larger compared to the dipole-dipole interactions. From the point of view of quantum mechanics, equation (2.4) is an approximation. Surprisingly this model works very well for a broad range of systems.

Spin-Orbital Interaction The spin-orbit interaction[73] can be deduced by using the Dirac equation.[72,74] The complete derivation can be found in the quantum mechanics textbooks.[72] This derivation, from the Dirac equation via the Pauli equation, leads to the following Hamiltonian, where the magnetic moment μ consists of two parts, the orbit- and the spin contribution

$$\vec{\mu} = -\vec{\mu}_{orbit} \cdot \vec{\mu}_{\text{spin}} = \frac{e_0}{2mc}\left(\vec{L} + 2\vec{S}\right). \tag{2.5}$$

The term with $\vec{L} + 2\vec{S}$ represents the so-called Russell-Saunders coupling or LS coupling. This coupling will be explained in more detail in the following discussion about the g-factor. The spin moment has the magnitude $\vec{\mu} = g\frac{e_0}{2mc}\vec{S}$. Here $g_e \approx 2.0023$ is the gyromagnetic factor or the Landé factor of a single electron as determined by the quantum field theory.

2.1.2. Magnetic Anisotropy

Magnetic anisotropy describes a preferential alignment of the magnetisation in a ferromagnetic material without an applied external magnetic field. The magnetic moments align along the energetically favourable direction, which is called the easy axis. Whereas, the hard magnetic axis describes the direction where one needs to apply the highest energy to force $\vec{M}$ to align parallel. In other words, considering the typical experimental setup, in this direction one has to apply the highest external magnetic field to the system.

Causes for the anisotropy are mainly the contribution of the SOI and the DDI, which lead to the magnetocrystalline- and the shape anisotropy.[75,76] There exist also the magnetoelastic- and exchange anisotropy, but these play a minor role for the systems investigated here. The spin-orbital interaction (SOI) leads to the magnetocrystalline anisotropy (MCA). The dipole-dipole interaction (DDI) is responsible for both the shape anisotropy and a minor contribution to the MCA. The effect of shape anisotropy is observed when rotating $\vec{M}$ with respect to the shape of the sample and the effect of magneto-crystalline anisotropy is observed by rotating $\vec{M}$ with respect to the crystallographic axes.[77]

The magnetisation is defined as the moment per unit volume and it depends on the product of the external magnetic field and the volume magnetic susceptibility χ, as shown here:

$$\vec{M} = \frac{\partial\vec{\mu}}{\partial V} \qquad \wedge \qquad \vec{M} = \chi_{\text{mag}}\vec{H}_{\text{ext}}. \tag{2.6}$$

For the macroscopic description of a FM system it is usual to define a thermodynamic function. Therefore, starting with the free energy $F_{\text{free}}(T, M, \vec{e}_M, \varepsilon)$, where M represents the magnitude of the magnetisation,
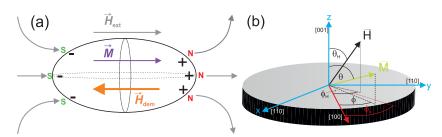
Fig. 2.1 (a) Scheme of a homogeneously magnetised ellipsoid inside an external field $\vec{H}_{\text{ext}}$. The magnetisation creates apparent poles on the surface due to charges distribution. The external field and the magnetisation are aligned parallel. Whereas, $\vec{H}_{\text{ext}}$ points in the opposite direction. (b) Presents the polar coordinate system of the limiting case of the ellipsoid as an infinitely disc.

T is the temperature, $\vec{e}_M$ is the unit vector with respect to $\vec{M}$, and ε is the strain tensor of the system. In a typical experiment, where $\vec{M}$ is rotated by a rotating external field, the magnetisation $\vec{M}$ changes. Therefore, in the free energy the magnitude of $\vec{M}$ is no longer an externally controlled parameter. This leads to the Legendre transformation for the thermodynamic potential of the so-called Gibbs free energy density. The result of the transformation is given by

$$F\left(T, H_M, \vec{e}_M, \varepsilon\right) \equiv F_{\text{free}} - H_M M. \tag{2.7}$$

In the latter equation the H_M represents the projection of H_{ext} along $\vec{e}_M$. Typically the unit vector, as well as H_M is expressed in polar coordinates as it simplifies the problem. The positions of the minima and maxima of the Gibbs [78,79] free energy density (F) of the system defines the direction of the hard magnetic axis (hard axis, maximum F) and the easy magnetic axis (easy axis, minimum of F). The energy which is needed to turn the magnetisation from the easy to the hard axis is called magnetic anisotropic energy (MAE). [80]

Due to the total free energy it is possible to define the so-called effective magnetic field H_{eff}. [81–83]

$$\vec{H}_{\text{eff}} = -\nabla_{\vec{M}} F_{\text{total}}. \tag{2.8}$$

This functional derivative of the Gibbs free energy with respect to the magnetisation defines the effective field H_{eff}, which is the axis about which the magnetisation precession occurs, [84] and it is the resulting magnetic field direction. This means it consists, beside the external magnetic field, of all internal magnetic fields, as well as the external demagnetizing field.

A ferromagnetic system loses its magnetic anisotropy in the case that it enters into a superparamagnetic state. [61] Superparamagnetism has to be taken into account for sufficiently small structures on the nanoscale regime. In that case, $\vec{M}$ randomly switches its direction, due to thermal excitation. [85] There exists a non-negligible probability of switching during the lifespan of a device, which leads to a data loss in magnetic recording media. Hence, one issue of investigations in the field of magnetic recording aims to find ways to overcome this limit. In contrast to the typical transition of ferromagnetism to paramagnetism at T_c, for the case of superparamagnetism this effect occurs at much lower T. This plays a role, when one considers the recording materials, like $CoCrPt:SiO_2$ and [Co/Pd] , which are discussed here. Especially, for the granular films of $CoCrPt:SiO_2$ films the superparamagnetic limit is an essential consideration in the context of perpendicular recording media. These grains have currently reached the superparamagnetic limit, their size being about 6–8 nm. [24] A high anisotropy is crucial to align the magnetisation and to keep this condition

thermally stable.

Magnetocrystalline Anisotropy If one considers an infinitely extended homogeneous ferromagnetic sample, such a sample should show an isotropic behaviour. Nevertheless, in practice there will be a magnetic anisotropic distribution observable. This phenomena can be explained in terms of the SOI and microscopic DDI.[86] Both interactions are coupled to the crystal lattice of a solid state sample. The short-range SOI via the orbital angular momentum and the long-range DDI via the vector $\vec{r}_{ij}$. One has to mention that compared to the Heisenberg exchange interaction (2.4) these interactions are 10 - 100 times smaller.[87] Values for the magnetic anisotropy energy (MAE) obtained using perturbation theory, can be found elsewhere,[80]. Recent ab-initio theoretical calculations were performed which achieve more precise results than perturbation theory.[88]

The geometry for theory and experiment is shown in Fig. 2.1(b).[2] The crystallographic directions are defined by the Miller indices.[89] The crystallographic [001] direction represents the z-axis, which in this case corresponds to the surface normal. Moreover, [110] is chosen to be the y-axis and [1$\bar{1}$0] is the x-axis. There are four corresponding angles to be considered, which depend on $\vec{H}$ and $\vec{M}$. The polar angles θ and θ_{H} are measured with respect to the surface normal. Whereas, the azimuth angles φ and φ_H are measured with respect to [100]. The azimuth angle φ_u represents the easy axis of the uniaxial in-plane magnetic anisotropy.

In most ferromagnetic materials the magnetocrystalline anisotropy is the main source of the magnetic anisotropy-energy density.[90] Typical values for the anisotropy-energy densities, the so-called anisotropy constants are for example 0.5×10^6 ergs/cm^3 for the bcc Fe and 5.0×10^6 ergs/cm^3 for hcp Co. The anisotropy field is given by

$$H_{\mathrm{a}} = \frac{2K_{\mathrm{i}}}{M_{\mathrm{s}}}. \tag{2.9}$$

and has the dimension of a magnetic field. The benefit of the factor 2 in the numerator is to compare the anisotropic field with the coercivity directly, as well as with the applied external field.[70]. The derivation of the mathematical expression of a fcc tetragonally distorted (fct) system, as well as for a hexagonal (hcp) system is presented in appendix A.

Shape Anisotropy The demagnetizing field can be derived starting from Gauss' and Ampère's laws of magnetism from the Maxwell equations.[73]

$$\nabla \cdot \vec{B} = 0 \quad \wedge \quad \vec{B} = \mu_0(\vec{H}_{\mathrm{dem}} + \vec{M}) \quad \Rightarrow \quad \nabla \cdot \vec{H}_{\mathrm{dem}} = -\nabla \cdot \vec{M} \tag{2.10}$$

Therefore, the divergence of the magnetisation is causing the demagnetizing field, which is always directed contrary to $\vec{M}$. Due to the shape dependence of the dipole-dipole interaction the calculation of arbitrary shapes is in most cases very complex because of inhomogeneity. For most geometries the demagnetizing factors have to be determined by numerical calculations. A simple system was derived by Aharoni and Osborn.[61,91] It describes a uniformly magnetised ellipsoid [see Fig. 2.1(b)]. In this case, $\vec{H}_{\mathrm{dem}}$ can be expressed by a dimensionless demagnetizing tensor $\hat{\mathrm{N}}$. Moreover, this tensor is spatially-independent.

$$\vec{H}_{\mathrm{dem}} - \hat{\mathrm{N}}\left(\vec{M}\right) \quad , \text{where } \hat{\mathrm{N}} = \begin{pmatrix} N_{xx} & 0 & 0 \\ 0 & N_{yy} & 0 \\ 0 & 0 & N_{zz} \end{pmatrix} \text{ with Trace}(\hat{\mathrm{N}}) \equiv 1. \tag{2.11}$$

---

[2]For all calculations the polar coordinate system is used: $x = \sin\theta\cos\varphi, \quad y = \sin\theta\sin\varphi, \quad z = \cos\theta$

Considering the limiting case of an infinite two-dimensional cylindrical disc [see Fig. 2.1(b)] the following demagnetizing factors are valid: $N_\parallel = N_{xx} = N_{yy} = 0$ and $N_\perp = N_{zz} = 1$. For the calculation of the shape anisotropy one needs the z component of the magnetisation $M_z = M \cos\theta$. By considering all of the assumptions mentioned previously the general integral for the dipole-dipole contribution of the free energy could be solved as shown here:

$$F_{\mathrm{dipole}} = -\frac{1}{2} \int_V \vec{M} \cdot \vec{H}_{\mathrm{dem}} \quad \partial V = 2\pi M_{\mathrm{s}} \cos\theta. \tag{2.12}$$

In several publications one can find examples of analytical and numerical calculations for the demagnetizing factors for other shapes.[92–99]

2.1.3. *g*-Factor

In section 2.1.1 the electron *g*-factor was mentioned and its value was given as $g_{\mathrm{e}} \approx 2.023$. In a real sample system, one observes, for instance from the FMR experiments a deviation to higher values. Here, some of these values for the materials discussed in this work are listed:

- ▶   Iron g_{Fe} ≈ 2.09 [100,101]
- ▶   Nickel g_{Ni} ≈ 2.17 [102] - 2.21 [101,103]
- ▶   Cobalt g_{Co} ≈ 2.18 [101,102]
- ▶   Permalloy g_{NiFe} ≈ 2.10 [101,104,105]
- ▶   CoCrPt -Ta $g_{\mathrm{CoCrPt\,-Ta}}$ ≈ 2.16 [106]

Obviously, these listed values differ significantly from the g_{e} derived. Attempts to explain this deviation by the anomalous Zeeman effect[107–111] do not work out because the influence of the crystal lattice in a solid cannot be neglected. Therefore, one has to take into account, that the atoms are fixed to a lattice which leads to a description by crystal field theory (CFT).[112,113] This theory combines the fields of neighbouring atoms to a macroscopic average field. In the case of 3d atoms the crystal field (CF) is dominant compared to the LS-coupling, because the 3d electrons are weakly shielded. Moreover, the spherical symmetry is disrupted. Therefore, the expectation value $\vec{L}_z$ is quenched, due to the fact that the $\vec{L}_z$ is not rotationally symmetric anymore. This effect is known as the "quenching of the orbital momenta" ($\Rightarrow \langle 0|\vec{L}_z|0\rangle \equiv 0$). These effects lead to an anisotropic *g*-factor. This can only be described by the perturbation theory,[79] where the spin-orbital interaction and the Zeeman interaction are considered as the perturbation. This leads to the perturbation Hamiltonian for the SOI and the Zeeman interaction

$$\mathscr{H}_{\mathrm{pert}} = \lambda \left(\vec{L} \cdot \vec{S} \right) + \beta \left(\vec{L} + g_{\mathrm{e}}\vec{S} \right) \cdot \vec{H}. \tag{2.13}$$

The spin Hamiltonian of the second order perturbation theory reads:

$$\mathscr{H}_{\mathrm{S}} = \sum_{\mathrm{i}} \langle 0|F_{\mathrm{i}}|0\rangle - \sum_{\mathrm{i,j}} \sum_{\mathrm{n}\neq 0} \frac{\langle 0|F_{\mathrm{i}}|\mathrm{n}\rangle \langle \mathrm{n}|F_{\mathrm{j}}|0\rangle}{E_{\mathrm{n}} - E_0} T_{\mathrm{i}}T_{\mathrm{j}} \tag{2.14}$$

The operator F_{i} acts only on the spatial variables and $T_{\mathrm{i,j}}$ only on the spin variables. After the evaluation of
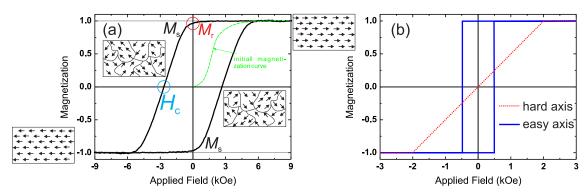
Fig. 2.2 (a) Hysteresis loop for ferromagnetic material. The surrounding boxes depict the behaviour of the magnetic domains. The initial magnetisation curve has been sketched. The black horizontal lines are showing the saturation magnetisation (M_s). The intersection emphasised by the red circle of $H = 0$ and hysteresis is the remanence (M_r). The blue circle shows the intersection of $M = 0$ and the loop, which is the coercivity. (b) Schematic sketch of an ideal measurement along the easy axis in comparison to a hard axis measurement for an anisotropic ferromagnet.

(2.14) and a substitution with the symmetrical tensor

$$\Omega_{ij} = \sum_{n \neq 0} \frac{\langle 0|L_i|n\rangle \langle n|L_j|0\rangle}{E_n - E_0}, \tag{2.15}$$

yields the following spin Hamiltonian:

$$\mathscr{H}_S = -\lambda^2 \sum_{i,j} \left(\Omega_{ij} S_i S_j \right) - \beta^2 \sum_{i,j} \left(\Omega_{ij} H_i H_j \right) + \beta \sum_{i,j} \left(H_i \underbrace{[g_e \delta_{ij} - 2\lambda \Omega_{ij}]}_{g_{ij}} S_j \right) \tag{2.16}$$

The derivation summarised here is described in detail in several textbooks.[114–116]. The tensor Ω_{ij} describes the deviation of the g-factor in a solid from the g_e-factor of an electron. The symmetry of Ω_{ij} is based on the crystallographic symmetry of the solid. Due to the fact, that

$$\frac{|\langle 0|L_i|n\rangle|^2}{E_n - E_0} > 0 \tag{2.17}$$

is valid, the g with respect to g_e gives for the elements with more than a half full occupied d-shell higher values (i.e. Ti, V, Cr). An opposite behaviour is observable for elements with a less than half-empty d-shell occupation (i.e.: Fe, Co, Ni, and Cu). In principle, the components of the tensor could be assigned to a certain orientation. Therefore, it is possible to distinguish between the in- and out-of-plane components of the g-factor by an angular-dependent measurement, e.g. by using a ferromagnetic resonance measurement. All the measurements presented in this work, which were made in order to obtain the g-factor, are showing the out-of-plane component of g. This restriction will be explained there, as well.

2.1.4. Hysteresis Loops and Switching Field Distributions

Hysteresis Loops   Several magnetometry techniques like MOKE, SQUID, and VSM measure a so-called magnetic hysteresis loop where the external magnetic field is swept between a field which saturates the sample in one direction and the same in the opposite direction.[117–119] In the case of a ferromagnetic system, once the material has been saturated, the field can be reduced to $H = 0$ and the system will retain some or all of its magnetisation as a remanence. The following is a description of how a hysteresis loop [see Fig.

2.2(a)] is measured. Starting with a ferromagnet in a demagnetised state, by increasing the external magnetic field, the loop follows the initial magnetisation curve (green) up to a saturated state. The value for this is called the saturation magnetisation (M_s). Subsequently, if one switches the field off, there will still be a remanent magnetisation present (M_r, red circle). To force the magnetisation back to zero, one has to reverse the driving magnetic field to a value, which is called the coercivity (H_c, blue circle). The property of the remanence is why permanent magnets retain their magnetism.[62,67,68]

In a continuous magnetic thin film, where the behaviour is generally dominated by the existence of domains, the hysteresis arises from the energy barriers which are pinning the domain walls from moving.[120,121] Starting from one saturation state where all spins are aligned in one direction, as the field is reduced the domains starts to nucleate in order to reduce the stray field of the sample. Once the field passes zero field the domains start to grow in order to increase the amount of $\vec{M}$ which is aligned with the field. In the case of an ideal continuous film where there are few pinning sides, the domain walls can pass through the entire sample in a relatively small field range which gives rise to sharp switching transition.

In granular recording media where the grains a strongly exchange decoupled and therefore, they can act as single domain particles. When the field is reduced from the saturated state, the single magnetic particles tend to align along their local easy axis. Furthermore, some of the single domain particles start to switch in order to reduce the stray field of the system. After the field has passed zero, single domain particles tend to switch at their individual switching fields.

The typical behaviour of a measurement along the hard- and the easy axis is shown in Fig. 2.2(b) for an idealised case. The reversal of magnetisation is caused due to a shift of the magnetic domains. Typically, when considering measurements with the applied field along the easy axis, there is just one domain wall moving. Therefore, the one jump from one saturated state to the other is observable. This is due to the fact that at a certain field all of the spins switch simultaneously and end up in the saturation magnetisation in the opposite direction. The hard axis is characterised by a linear slope, which originates from the coherent rotation of the magnetisation. Or in other words, the switching is a continuous process of individual magnetic domains. Typically, a mixture of both cases is observable, as will be shown in chapter 3.

Switching Field Distribution   As was previously mentioned, magnetically separated nanostructured or granular ferromagnetic films, as for instance CoCrPt:SiO$_2$ on nanocones, typically behave as single domain particles. Therefore, in the hysteresis loop the switching process occurs over a wide range of fields which are affected by the uniformity of the structures. The effect of the width of the switching transition is directly related to the switching field distribution (SFD) of the magnetic units. The interplay of magnetocrystalline-, interface-, interdot-, as well as shape anisotropy mainly determines the magnetisation reversal mechanism. One should note that for improving a recording media the SFD should be narrowed to avoid errors in the writing process. The analysis of the switching field distributions was done by using the hysteresis branch from negative to positive magnetic saturation field values (ascending branch) [see Fig. 2.3(a) and (b)].[122–125] In some publications it is shown how to analyse the SFD in terms of intrinsic and extrinsic effects. This was achieved by comparing the SFD result of the major hysteresis loop with the SFD result of a minor loop.[126,127] In this thesis, the method was applied to our results, revealing rather small deviation and therefore, we only need to present the SFD analysis of major loops. The shape of the loop branch is fitted by a Gaussian cumulative distribution function, which is given by[128]

$$\Phi(x) = \frac{1}{\sqrt{2\pi}} \int_{-\infty}^{x} e^{(-t^2/2)} dt = \frac{1}{2} \left[1 + \text{erf}\left(\frac{x}{\sqrt{2}} \right) \right], \; x \in \mathbb{R}. \tag{2.18}$$
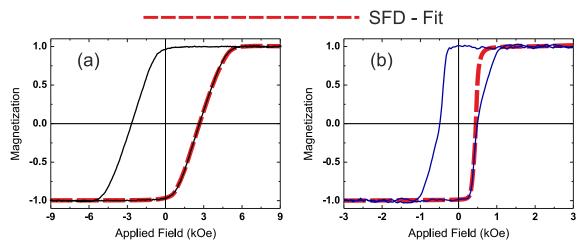
Fig. 2.3 (a) shows a polar MOKE hysteresis loop of an unirradiated granular CoCrPt:SiO$_2$ sample. The red fitting curves are the Gaussian cumulative distribution function. Compared to (b), which shows an irradiated granular CoCrPt:SiO$_2$ sample (40 keV Co$^+$, fluence: 5×10^{15}cm^{-2}), the function has changed to a more pronounced simultaneous switching of all grains. The reason for this behaviour will be discussed in detail in subsection 3.2.2 in the second chapter.

This equation (2.18) could be expressed as[129]

$$F(x, \mu, \sigma^2) = \Phi\left(\frac{x - \mu}{\sigma}\right) = \frac{1}{2}\left[1 + \mathrm{erf}\left(\frac{x - \mu}{\sigma\sqrt{2}}\right)\right]. \tag{2.19}$$

The parameters used are μ as the expected mean value and the σ^2 as the variance. Therefore, the fitting function was obtained by substituting the μ by the value of H_c of the loop, as well as the σ^2 by the SFD^2. In this application of the equation the x-axis it the magnetic field H, and so the resulting fitting equation is:

$$F_{fit}\left(H, H_c, \mathrm{SFD}^2\right) = \frac{1}{2}\left[1 + \mathrm{erf}\left(\frac{H - H_c}{\sqrt{2}\,\mathrm{SFD}}\right)\right]. \tag{2.20}$$

2.1.5. Magnetization Dynamics

Interest in the field of magnetisation dynamics has been revived over the last two decades due to an increasing technical demand for faster magnetic devices.[130–132] The ferromagnetic resonance technique is a well-established technology to investigate dynamical aspects of magnetism like the damping. Furthermore, the topic of ultra-fast magnetisation dynamics is of interest to both research institutes and industry. The time scale of the dynamical processes in magnetism is the pico- and femtosecond time regime.[133–135] Such ultra-fast dynamics can be experimentally investigated by pump-probe setups, like the time-resolved magneto-optical Kerr effect.[136–139] Both of the techniques mentioned above will be introduced in section 2.2. The underlying fundamental physics of the dynamics will be described here.

Equation of Motion without Damping   Here, one will find an introduction to the equation of motion, which describes the precession of the magnetisation around the effective field. In certain systems (for example small single domain particles) where the exchange force dominates and so all spins are forced to be collinear (see section 2.1.1), we can approximate the system by a single magnetic moment

$$\vec{M} = \frac{1}{V}\sum_{i=1}^{N}\mu_i. \tag{2.21}$$

In contrast to an equilibrium situation, where $\vec{M} \times \vec{H} \equiv 0$ is valid, the equation of motion shows a torque due to a change between $\vec{H}$ and $\vec{M}$:

$$\vec{M} \times \vec{H}_{\text{eff}} = \xi, \tag{2.22}$$

where ξ can be described as a torque, in the same manner as for classical mechanics

$$\xi = \frac{\partial \vec{L}}{\partial t} \tag{2.23}$$

The relation between angular momentum and torque is $\vec{M} = -\gamma \vec{L}$. Therefore, equation (2.23) describes the rotation of the sample in the direction of the effective field when there is a change of the angular momentum. Here γ is the gyromagnetic ratio

$$\gamma = \frac{g|e_0|}{2m_e}. \tag{2.24}$$

By substituting the derivative of $\vec{M}$ with respect to time into the equation (2.23) leads to

$$\frac{\partial \vec{M}}{\partial t} = -\gamma \frac{\partial \vec{L}}{\partial t} = -\gamma \tau = -\gamma \mu_0 \left(\vec{M} \times \vec{H}_{\text{eff}} \right). \tag{2.25}$$

Writing the separated Cartesian components x, y, z while the effective field $\vec{H}_{\text{eff}} = (0, 0, H_{z,\text{eff}})$ is applied in the z-direction

$$\frac{\partial M_x}{\partial t} = -\gamma \mu_0 M_y H_{z,\text{eff}} \qquad \frac{\partial M_y}{\partial t} = \gamma \mu_0 M_x H_{z,\text{eff}} \qquad \frac{\partial M_z}{\partial t} = 0 \tag{2.26}$$

one can see, that a pertubation to $\vec{M}$ induces a perpendicular motion to both the effective field, as well as to the moment direction. There is, however, no motion in the field direction.[140] Equation (2.25) can be analysed in more detail by multiplying in sequence by the magnetisation $\vec{M}$ and the effective field $\vec{H}_{\text{eff}}$ (whilst assuming a time-invariant static magnetic field). This leads then to the following:

$$\frac{\partial [\vec{M}]^2}{\partial t} = \frac{\partial [\vec{M} \cdot \vec{H}_{\text{eff}}]}{\partial t} \equiv 0. \tag{2.27}$$

Equation (2.27) proves that the magnetisation remains constant, that it never reaches a parallel alignment with the effective field, and that the angle θ between $\vec{M}$ and $\vec{H}_{\text{eff}}$ [see Fig. 2.4(a)] is a time-invariant function.[105] So, in other words, once such a motion is excited it continues to processes indefinitely. Obviously, this does not describe a real system. A real precessional motion is associated with a loss of kinetic energy due to a counteracting interaction, which leads to a damping effect.

Equation of Motion with Damping   When comparing the indefinite precession mentioned above with experimentally obtained results, one observes a damped precession, which ends up in a parallel alignment of $\vec{M}$ and $\vec{H}_{\text{eff}}$. This final state is the equilibrium state. To reach this state the precessing magnetisation has to transfer kinetic energy to something else. Causal mechanisms for this transfer of E_{kin} are the microscopic interaction between the magnetisation, spins, and lattice.[87] One derivation for the mathematical description of the damping phenomena is the assumption of an effective field with a finite time delay δt. Then equation (2.25) has to be rewritten as

$$\frac{\partial \vec{M}(t)}{\partial t} = -\gamma \mu_0 \left(\vec{M}(t) \times \vec{H}_{\text{eff}}(t - \delta t) \right). \tag{2.28}$$
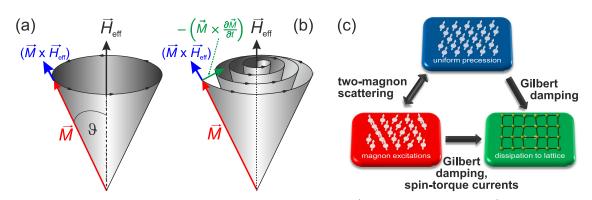
Fig. 2.4 (a) Scheme of the undamped precession of the magnetisation $\vec{M}$ around the effective field $\vec{H}_{\text{eff}}$. (b) Resulting motion including the Gilbert damping term. This term is a phenomenological description of a precession that is reducing in magnitude over time due to a loss of kinetic energy. Moreover, the motion now precesses helically in the direction towards the effective field. (c) Causal interplay for the damping phenomena on the atomic-level. [141]

In order to define $\vec{H}_{\text{eff}}(t - \delta t)$, this term can be expanded as a Taylor series with respect to t, contributions higher than the 2$^{\text{nd}}$ degree can be neglected, By using the derivative of the effective field with respect to $\vec{M}(t)$, one can write

$$\frac{d\vec{H}_{\text{eff}}(t - \delta t)}{d\vec{M}(t)} \frac{d\vec{M}(t)}{dt}. \tag{2.29}$$

By substituting equation (2.29) into the Taylor expansion one obtains,

$$\vec{H}_{\text{eff}}(t - \delta t) = \vec{H}_{\text{eff}}(t) - \delta t \frac{d\vec{H}_{\text{eff}}(t)}{d\vec{M}(t)} \frac{d\vec{M}(t)}{dt}. \tag{2.30}$$

The transformation back into the differential equation leads to

$$\frac{\partial \vec{M}(t)}{\partial t} = \underbrace{-\gamma \left(\vec{M}(t) \times \vec{H}_{\text{eff}} \right)}_{\text{precessional term}} + \underbrace{\frac{\alpha}{M_s} \left(\vec{M}(t) \times \frac{d\vec{M}(t)}{dt} \right)}_{\text{damping term}} \qquad \text{where } \alpha = \gamma M_s \delta t \frac{d\vec{H}_{\text{eff}}}{d\vec{M}(t)} \tag{2.31}$$

This derivation presented here can be found in the literature. [142] This dimensionless constant α is the so-called Gilbert damping tensor, which for most applications is a diagonal tensor, or even isotropic. Therefore, it is mostly written as a scalar coefficient. Equation (2.31) is well-known as the Landau-Lifshitz-Gilbert equation. The derivation can be found in the literature. [81,82,84]

The Gilbert damping can be compared to the viscosity of fluids. The behaviour of the Gilbert damping term is depicted in Fig. 2.4(b) and the interplay of the different damping components in Fig. 2.4(c). This equation of motion describes a ellipsoidal spiral trajectory, where the damping points towards the effective field vector H_{eff}. The damping term, the direction of motion and $\vec{M}$ are all pointing perpendicular to each other. As shown for the Landau-Lifshitz equation the magnetisation magnitude remains constant.

2.2. Experimental Details

The effect of morphology changes on magnetic properties are the main focus of the work presented in this thesis. [2] Therefore, the preparation of nanostructured surfaces and the deposition of FM films on top is a crucial point. The morphology chosen for this work was a nanopattern of cones on a substrate. Therefore, in the following section this structure will be referred to as the nanocone structure. These structures are created by the ion erosion technique, an introduction to this is given in the following subsection. Subsequently, to deposit a three dimensional ferromagnetic structure on top of the nanocones, two different techniques were used: in the case of Permalloy films molecular beam epitaxy was used, whereas the $CoCrPt:SiO_2$ and $[Co/Pd]_8$ films were prepared using magnetron sputtering. Both techniques will be briefly introduced in subsection 2.2.2.

2.2.1. Ion Beam Erosion and Ion Implantation

Fig. 2.5 Sketch of the energy distribution of impinging ions during the ion erosion process. The surface element (a) with concave geometry is eroded faster compared to that (b) with a convex geometry. This is due to higher energy impact (red lines) in the indentation compared to the elevations. [143,144]

Ion Beam Erosion   The modification of the topography of a surface in the nanometre regime requires special techniques. Since 1962 it has been known by Navez et al., [145] that a broad ion beam of 4 keV induces a periodic structure on glass. Subsequently, a theory was derived by Sigmund [146] which describes the diffusion process. For several other materials, e.g. Si, GaAs, and GaSb, the effect could be reproduced. From this beginning investigations into the ion erosion technique have been intensively developed and improved. [56,144,147,148] Of particular note is the Bradley-Harper theory, which combines the diffusion processes and the sputter yield[3] into one model, and which improved the understanding of this process. An important fact is the angular dependence of the ion erosion technique (IET), which means that by shooting the ions at different angle of incidence onto the surface, one will achieve different periodic structures, or will smoothen the surface. At one extreme, applying the ion beam under grazing incidence one will obtain a so-called ripple pattern formation[149–154] and at the other extreme a beam applied perpendicular to the surface will create the nanocone structure. [56,58,155–159]

The formation of self-organised patterns by sputtering is caused by three competing processes: [144,146,148] (i) The roughening is induced by the curvature dependent surface erosion[146] due to the decreased energy deposition at the hillocks as compared to the dents/troughs. This results in a lower sputter yield, hence, a stronger erosion of the troughs than of the hillocks. (ii) The smoothing of the surface caused by surface diffusion and viscous flow of the surface material, and (iii) preferential sputtering in the case of compound

---

[3]The sputter yield describes the relation between the injected and the dislodged atoms of a sputtered sample.
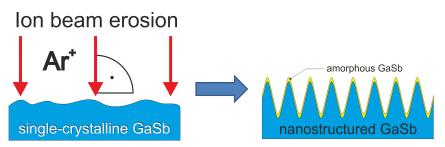
Ion beam erosion

Fig. 2.6 Illustration of the sputtering process of nanocones. The beam has to be applied normal to the substrate. This substrate is a single-crystalline GaSb(001) wafer. The resulting nanocone surface has a few nanometre thick amorphous GaSb cap.

materials.[147,152,157] These three processes lead to a development of nanocones on GaSb as the preferred erosion process as discussed in more detail in [153,156].

Here, the preparation of the nanocones on GaSb (001) by using the IET is described. The experimental setup is a vacuum chamber with a load lock part. The base pressure typically achieved in the chamber is $p = 10^{-8}$ mbar. The sample holder is water-cooled ($T \approx 15$ °C) and a Kaufman ion gun is used to provide a broad ion beam. The sample is fixed by a Cu shield with a hole of about 1 cm in diameter. Due to this Cu shield it is possible to control the temperature of the GaSb sample and to avoid overheating. The Ar partial pressure was typically $2.5 \cdot 10^{-6}$ mbar. To create the nanocones, one has to apply a broad Argon ion beam parallel to the substrate normal. The physical origin of the process is sketched in Fig. 2.5. The substrate surface is never perfectly smooth at the start of the process, this initial roughness is essential to the start of the growth of the nanostructure. The binary GaSb has a different behaviour as compared to the samples of one element, e.g. Si, concerning the energy deposition property. It is worth mentioning, that there is an ongoing discussion in the literature, about how to describe these processes as well as conflicting experimental results which were obtained and need to be discussed.

By tuning the applied kinetic energy of the ions, the distance between the nanocones is tuneable. The distance itself is called the characteristic length and will be further abbreviated by l_c. The fluence of the applied Ar ions mostly affects the height and the diameter of the cones. Besides the flux, the fluence also influences the ordering of the nanocones. The principle of the process is depicted in Fig. 2.6. An ion beam with a certain energy, fluence, and flux creates due to the diffusion, a smoothing effect, and due to the sputter yield, a nanocone structure on the surface. The nanocones have a few nanometres (usually less than 5 nm thick) of an amorphous cap on top. All the process parameters and the dimension of the nanocones achieved will be discussed for all prepared sample series in each section.

Ion Implantation   The aim of the ion implantation is the intermixing and enrichment of the target material with the applied species of ions. In this work the effects on the magnetic properties of a granular CoCrPt:SiO_2 were studied. In contrast to the IET, in implantation the erosion should be avoided. The implanted ions should stick inside the film and penetrate to a desired depth, controlled by the energy. In designing the samples the first step was to determine the right energy and fluence values for the implantation, this was done by using the two simulation packages SRIM[4] and TRIDYN.[160,161] The SRIM package provides a simple way to obtain information about the implantation depth of the ions. Using this information, it is possible to target a specific depth in the sample for intermixing and concentration. Nevertheless, one has to simulate effect of the fluence, as well. This can be achieved by using the TRIDYN simulation software. It takes the effects of both the energy and the fluence into account. There still remains one problem however:

---

[4] http://www.srim.org/

often the exact binding energies of the consisting elements are unknown in the composition used and have to be estimated, which leads to a discrepancy between simulation and experiment. Once all the implantation parameters required to create the desired sample were determined, the ion implantation was undertaken in the ion implantation centre of our institute. For the ion implanted samples presented in this work a kinetic energy of 40 keV was used.

2.2.2. Deposition Techniques

The next step in the preparation process was to deposit a ferromagnetic thin film on top of the sample surfaces. In the case of the patterned samples, the deposited film should completely cover the textured surface of the underlying structure. This leads to a three-dimensional magnetic film. The growth of the granular CoCrPt:SiO$_2$ films was a critical point, which influences the magnetic properties significantly, as will be shown in subsection 3.2.3. For the CoCrPt:SiO$_2$ and the [Co/Pd] sample series, magnetron sputtering was used. This was done by Hitachi GST. The Permalloy samples were prepared at our institute, with the support of Michael Körner and Oskar Liedke using the *molecular beam epitaxy*.

Molecular Beam Epitaxy   MBE is one of the physical vapour deposition techniques used to deposit thin films with single crystalline properties. Before deposition the sample can be cleaned thermally. The deposition phase uses an electron beam evaporator to vapourise the target which can be one of Py, Cr, Co, Cu, or Fe. The growth rate of the evaporated material can be monitored using a quartz crystal microbalance. The pressure during evaporation was $p = 10^{-6}$ mbar. A crucial point for the epitaxy is the previously mentioned amorphous film on top of the nanocones. The thick amorphous layer makes it necessary to grow first a Cr seed layer onto the nanocones, the thickness of this layer was 5 nm. The Cr grows polycrystalline on the amorphous GaSb and was chosen to be at least about 5 nm thick. Due to the presence of a Cr seed layer, the Permalloy is able to grow epitaxially, because the Cr seed layer is polycrystalline, the Py film grows in a polycrystalline manner as well.

A tension occurs caused by the mismatch Σ between the different lattice constants ($a_{Py} = 3.546$ Å, $a_{Cr} = 2.885$ Å).[162–164] To determine the mismatch, one has to derive first the relation between the lattice constant for the fcc structure (Py) and the lattice constant for the bcc crystal structure (Co), which is equal to the bond length. Therefore, the resulting values are $a'_{Cr} \approx 2.234$ Å and $a'_{Cr} = 2.040$ Å and so Σ can be determined from the relation:

$$\Sigma_{Cr,Py} = \frac{a'_{Py} - a'_{Cr}}{a'_{Cr}} = \frac{2.234\text{Å} - 2.040\text{Å}}{2.040\text{Å}} \cong 0.095. \tag{2.32}$$

Due to the presence of the seed layer, the mismatch has only to be considered for Py and Cr. In the beginning the deposited material is growing with the same lattice structure as the substrate. This leads to the tension, which after some monolayers causes defects in the lattice. Therefore, the film splits and island growth becomes dominant.[165–167] Due to the relatively small $\Sigma = 0.095$, the island growth does not need to be taken into account due the thin films which were deposited. Finally, the deposited Py film was coated by a cap layer of 3 nm.

Magnetron Sputtering   All of the CoCrPt:SiO$_2$ sample series, as well as the [Co/Pd] samples presented in this work were prepared by DC magnetron sputtering (DC-MS).[168–171] The CoCrPt:SiO$_2$ samples were prepared at the research centre of Hitachi GST and the [Co/Pd] series at the Chemnitz University of Technology in the group of Prof. Dr. Manfred Albrecht. DC magnetron sputtering takes place under
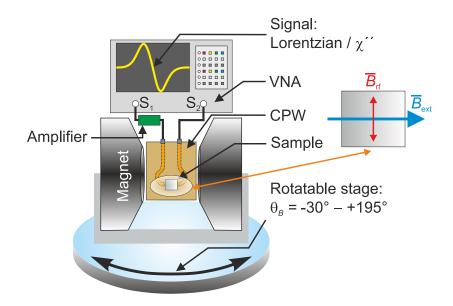
Fig. 2.7 Sketch of the VNA-FMR setup. The geometry of the external magnetic field and the rf field is magnified on the right side.

ultra-high vacuum conditions, where the atoms of a solid target are sputtered by an injected discharge plasma towards a cooled substrate.[172,173] The advantage of DC-MS is the ability to deposit materials with a high melting point and at a much higher rate as compared to MBE. The drawback of DC-MS is that the samples created are usually polycrystalline. That however, was an intentional outcome for the studies in this work.

2.2.3. Magnetometry

The measurement techniques used for this study can be separated in to the following groups: dynamic magnetometry [vector-network-analyser ferromagnetic resonance (VNA-FMR), time-resolved magneto-optical Kerr effect (TRMOKE)], static magnetometry [magneto-optical Kerr effect (MOKE), superconducting quantum interference device (SQUID), vector vibrating sample magnetometry (vector-VSM)], and the structural investigation techniques. Except for the FMR, MOKE, and TRMOKE measurements, all other techniques were provided by co-workers. This subsection is divided into a description of magnetometry and structural investigations. VNA-FMR and TRMOKE were used to obtain qualitative and quantitative information about the change in the magnetic properties due to the morphology modification and the ion implantation.

Vector Network Analyser Ferromagnetic Resonance   VNA-FMR is a microwave spectroscopy technique. In simple terms it is based on the resonant absorption of an electromagnetic wave inside a ferromagnetic material, where $\vec{M}$ precesses around an effective magnetic field $\vec{B}_{\text{eff}}$ (see paragraph 2.1.2), which is applied perpendicularly to the microwave field ($\vec{b}_{\text{rf}}$).[174,175] The ferromagnetic resonance technique measures the integral signal from a volume of material, with a resolution of approximately 10^{11} spins for a common setup.[176] Recently, a new generation of FMR, which utilizes a microresonator, overcame this threshold with a sensitivity of 10^7 spins.[177]

In FMR, due to the external magnetic field, the degeneracy of the energy levels is lifted. A microwave photon with an energy which matches the resulting energy gap can be resonantly absorbed.[178–180] This fact is expressed by the simplest form of the resonance condition $\omega = \gamma \vec{B}_{\text{eff}}$. Furthermore, this expression shows,

that the magnetic resonance spectrum could be obtained by either a field or a frequency sweep.[181–185] A technique that is a close analogue of VNA-FMR is electron paramagnetic resonance (EPR). EPR probes a paramagnet instead of a ferromagnet.[186–190] The basic theoretical description of the ferromagnetic resonance was published by Landau and Lifshitz[84] and the first experimental demonstration by Griffiths.[191] To derive a general resonance condition one has to take a damped equation of motion like the LLG (see (2.31)) and the general relation for the Gibbs free energy (see (2.8)) into account. Smit and Beljers have published an expression showing how the general resonance conditions for different crystallographic systems could be evaluated.[192] The improvement arising from the symmetrical expansion terms introduced by Baselgia made it possible to achieve results for all field angles.[193] The complete derivation for a fcc tetragonally distorted and a hexagonally closed packed system is given in the appendix A. In the following paragraph the experimental setup is introduced.

Due to the design of the setup the measurements can be carried out in an angle- or a frequency-dependent manner. The fitting can subsequently be done by using the general resonance condition [see Appendix A], where the anisotropy constants are included. In order to compare the obtained anisotropy constants with fields, as mentioned earlier in the theoretical section, the values are usually listed in the unit of an anisotropy field, which is given by $2K_i/M_s$. Typically the anisotropy constants are given in cgs-units, therefore all these data obtained in this thesis are presented in G or Oe. This procedure and its interpretation will be discussed after the setup has been introduced.

The setup is shown schematically in Fig. 2.7. The conventional Bruker electromagnet is mounted onto a planetary transmission, and therefore, can be rotated in the polar geometry range of $\theta_B = -30°-+195°$. The power supply for the magnet can supply a maximum current of 60 A, which can generate a maximum field range of $T = \pm 2.2$ T for the minimum pole gap possible. All field values are recorded in Tesla by a Hall probe, which is mounted on the pole of the electromagnets. Therefore the x-axis of the spectra typically shows $B_{res}(T)$. The conversion between these units can be looked up in the section C. Between the pole shoes the polar sample holder is mounted. On this sample holder the grounded coplanar waveguide (CPW) is fixed.[194] To measure in the polar geometry the sample holder is fixed while the magnet is rotated. In addition, this setup has a linear translation stage with an azimuth sample holder. This second sample holder has the capability to measure in-plane in the azimuth angle range $\varphi = 360°$. The CPW is connected to the Agilent E8364B vector network analyser (VNA) by two coaxial cables. The VNA supplies the system with microwaves in the range of 10 MHz to 50 GHz. The maximum power is 6 dBm. The VNA has two ports and therefore, the measurements can be done in transmission and/or reflection modes. Due to the fact that each port can measure and source simultaneously, this leads to four signals which can be recorded at the same time. These signals yield the so-called scattering parameters S_{ij}. The index i represents the port, where the signal leads to, whereas, the index j is the origin of the signal). To increase the power, an amplifier (maximum power amplification = 30 dBm) was interconnected between the VNA and the CPW. This device increases the rf field at the CPW stripline, which is the region on the CPW, where the sample is mounted. The characteristics of the CPW will be discussed in the following. The measurements in this work utilise the transmission signal S_{21}, which is a measure of the power transmission from port 1 to the port 2. The CPW is a flat wave-guide with a dielectric substrate of height h, where rf microwaves in broad range could be fed through three conductive areas on top of the substrate.[195] These areas are separated into the ground conductor which is on both sides of the centre conductor. Both the ground and the centre area (width w) are separated by gaps (g). The current I through the centre runs in the opposite direction to the ground current $-I/2$ on both sides. Therefore, due to this geometry the magnetic fields are oriented in opposing directions as well. Figure. 2.8(a) shows a cross-section through the stripline in the middle of the CPW. The stripline is a narrow area in the middle of the CPW. In Fig. 2.8(b) the narrow stripline is shown in the middle. Its
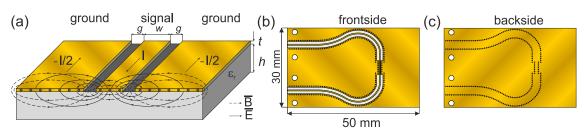
Fig. 2.8 (a) Perspective sketch of a coplanar waveguide. (b) Frontside sketch of a CPW. (c) Backside sketch of a CPW.[105]

purpose is to increase the field intensity outside the CPW which leads to excitation of a larger volume inside the sample. In other words, more spins are driven and therefore this improves the achievable signal. The feedthroughs on both sides are manufactured so that the microwaves can pass through with only a small loss of energy. All components have an impedance of 50 Ω, a value that is typical for most high-frequency electric circuits. Figures. 2.8(b) and (c) illustrate the complete CPW. The shape of the microwave feedthrough is due to the construction of the setup. The metal filled holes (called vias),[195] which connect both of the ground planes with the backside ground plane are crucial to achieve desired quasi-transversal electromagnetic modes (CPW-modes) as well as to avoid higher order modes.[105] They suppress the parallel plate line mode and furthermore, due to a cut-off frequency, the higher order modes as well. On top of the stripline of the CPW the sample can be fixed by a sample holder. The LabVIEW control software for the complete setup was written by Mathias Wieser, Michael Körner, and Kilian Lenz. Using the control software measurements can then be carried out automatically.

In the following paragraph the dynamic susceptibility χ will be derived. A more detailed derivation can be found in the thesis of Bilzer, Kalarickal or Neudecker.[83,196,197] One can start the derivation using the simple precession term in the LLG equation (2.31). The external magnetic field $\vec{H}_{\text{ext}}$ points in the direction of the z-axis, a small time-dependent microwave field $\vec{h}_{\text{rf}}(t)$ is applied ($\vec{H}_{\text{ext}} \gg \vec{h}_{\text{rf}}(t) \wedge \vec{h}_{\text{ext}}(t) \perp \vec{h}_{\text{rf}}(t)$). Therefore, the field and the magnetization is expressed by

$$\vec{H}(t) = h_{\text{rf}}e^{i\omega t}\vec{e}_{\text{x}} + h_{\text{rf}}e^{i\omega t}\vec{e}_{\text{y}} + h_{\text{ext}}\vec{e}_{\text{z}} \tag{2.33}$$

$$\vec{M}(t) = m_{\text{x}}e^{i\omega t}\vec{e}_{\text{x}} + m_{\text{y}}e^{i\omega t}\vec{e}_{\text{y}} + M_{\text{s}}\vec{e}_{\text{z}}. \tag{2.34}$$

Both of these equations can be plugged into the precessional term of equation 2.31, which leads to the following coupled linear system

$$\begin{pmatrix} m_{\text{x}} \\ m_{\text{y}} \end{pmatrix} i\omega t = \gamma \left[\begin{pmatrix} -h_{\text{y,rf}} \\ h_{\text{x,rf}} \end{pmatrix} M_{\text{s}}e^{i\omega t} + \begin{pmatrix} -m_{\text{y}} \\ m_{\text{x}} \end{pmatrix} H_{\text{ext}}e^{i\omega t} \right]. \tag{2.35}$$

This system of equations can be evaluated by some algebraic transformations which lead to the result:

$$\left[(\gamma H_{\text{ext}})^2 - \omega^2 \right] m_{\text{x}} = \gamma M_{\text{s}} H_{\text{ext}} h_{\text{x,rf}} - i\omega\gamma M_{\text{s}} h_{\text{y,rf}} \tag{2.36}$$

By comparing the latter equation with the magnetic susceptibility tensor $\vec{m} = \hat{\chi}\vec{h}$ and with the substitution of the resonance frequency $\omega_0 = \gamma H_{\text{ext}}$ one obtains the tensor components

$$\chi_{\text{xx}} = \frac{\gamma M_{\text{s}}\omega_0}{\omega_0^2 - \omega^2} \qquad \chi_{\text{xy}} = \frac{-i\gamma M_{\text{s}}\omega}{\omega_0^2 - \omega^2}. \tag{2.37}$$

This result can be improved by considering the damping term in the LLG. In this case the equation (2.36)
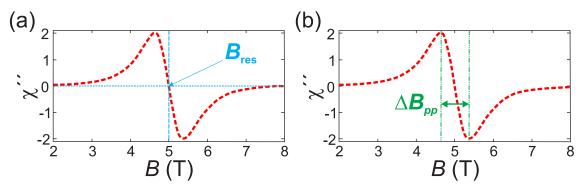
Fig. 2.9 Typical FMR signal with the main parameters (a) B_{res} and (b) ΔB_{pp}

will be as follows

$$\left[(\omega_0 - i\alpha\omega)^2 - \omega^2\right] m_{\mathrm{x}} = \gamma M_{\mathrm{s}} (\omega_0 + i\alpha\omega) h_{\mathrm{x,rf}} - i\gamma\omega M_{\mathrm{s}} h_{\mathrm{y,rf}}. \tag{2.38}$$

Both of the susceptibility relations also change.

$$\chi_{\mathrm{xx}} = \frac{\gamma M_{\mathrm{s}} (\omega_0 + i\alpha\omega)}{(\omega_0 + i\alpha\omega)^2 - \omega^2} \qquad \chi_{\mathrm{xy}} = \frac{-i\gamma M_{\mathrm{s}}\omega}{(\omega_0 + i\alpha\omega)^2 - \omega^2}. \tag{2.39}$$

Now, both components are complex. The real part of χ_{xx} is evaluated using its complex conjugate

$$\chi'_{\mathrm{xx}} = \frac{\gamma M_{\mathrm{s}}\omega_0 \left(\omega_0^2 + \omega^2\right)}{\left(\omega_0^2 - \omega^2\right)^2 - \omega^2 + (2\alpha\omega\omega_0)} \qquad \chi''_{\mathrm{xy}} = \frac{-\alpha\gamma M_{\mathrm{s}}\omega \left(\omega_0^2 + \omega^2\right)}{\left(\omega_0^2 - \omega^2\right)^2 - \omega^2 + (2\alpha\omega\omega_0)} \tag{2.40}$$

Both susceptibilities are representing the mathematical expression of a Lorentzian function, which is typical for resonant processes. Usually, χ''_{xy} is measured by the setup utilised in this work. The typical shape of the χ''_{xy} spectrum is represented in Fig. 2.9 by a yellow Lorentzian curve. Furthermore, this response function includes the dispersion of the FMR signal.

   The final transformation, which will be discussed here, is related to the anisotropy, exchange and demagnetizing fields which were neglected so far. All of them are contributing to the effective field $\vec{H}_{\mathrm{eff}}$. Here, the evaluation will be restricted to the influence of the demagnetizing fields. The static field is represented by $\vec{H}_0 = H_{\mathrm{ext}} - N_{\mathrm{z}} M_{\mathrm{s}}$ and the microwave field extended with $\vec{h}_{\mathrm{rf}}(t) = \tilde{h}_{\mathrm{x,y,rf}}(t) - N_{\mathrm{x,y}} m_{\mathrm{x,y}}(t)$ The parameter $\hat{N}$ is the demagnetising tensor as introduced earlier. The application of these transformations will lead to:

$$\chi_{\mathrm{xx}} = \tag{2.41}$$
$$\frac{\gamma M_{\mathrm{s}} (\gamma H_0 + \gamma M_{\mathrm{s}} (N_{\mathrm{y}} - N_{\mathrm{z}}) + i\alpha\omega)}{\gamma^2 (H_0 + M_{\mathrm{s}} (N_{\mathrm{y}} - N_{\mathrm{z}}))(H_0 + M_{\mathrm{s}} (N_{\mathrm{x}} - N_{\mathrm{z}})) - \omega^2 + i\alpha\omega (2\gamma (H_0 - M_{\mathrm{s}} N_{\mathrm{z}}) + \gamma M_{\mathrm{s}} (N_{\mathrm{x}} + N_{\mathrm{y}}))}.$$

From the above equation one can derive the resonce field/frequency as well as the linewidth. The resonance condition is given by

$$\omega = |\gamma| \sqrt{[H_0 + M_{\mathrm{s}} (N_{\mathrm{y}} - N_{\mathrm{z}})] [H_0 + M_{\mathrm{s}} (N_{\mathrm{x}} - N_{\mathrm{z}})]}. \tag{2.42}$$

and is known as the Kittel formula.[181] This relation is only valid in the case of a uniformly magnetised film,
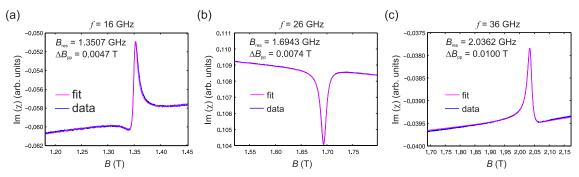
Fig. 2.10 Frequency dependent VNA-FMR measurements of a planar Py film on GaSb: The results measured at: (a) 16 GHz, (b) 26 GHz, and (c) 36 GHz. The fits were achieved with equation (2.43)

a detail which will become important when discussing the results in this thesis. As mentioned before the susceptibility χ''_{xy} shows the shape of a Lorentzian curve. The fitting of the data was done by using a Matlab program using a complex Lorentzian function, which is given by

$$L_{\mathrm{fit}}(B) = A_0 \frac{(2\Delta B)^2 - 2\Delta B \left(B - B_{\mathrm{res}}\right)^2 i}{(2\Delta B)^2 + \left(B - B_{\mathrm{res}}\right)^2} e^{i\varphi}, \tag{2.43}$$

where A_0, ΔB, B_{res}, B, and φ are the signal amplitude, the linewidth, the resonant field, the applied field and the signal phase. The phase is a particularly crucial part in this fit equation, an example of the role the phase plays is depicted in Fig. 2.10(a) - (c). Figure 2.10(a) - (c) shows a frequency dependent VNA-FMR measurement (blue) fitted (magenta) with (2.43). It clarifies that only with the phase φ term included can the significant change of the Lorentzian be fitted. More details about the physical background of the parameters and the Lorentzian fit function can be found in the publication by Celinski. [198] In Fig. 2.9(a) and (b) a typical FMR spectrum is sketched. When applied to such a dataset the fit routine will yield at least two parameters back: the resonance field B_{res} [see Fig. 2.9(a)/blue] and the linewidth ΔB_{pp} [see Fig. 2.9(b)/green]. The resonance field will give information about the static magnetic properties, like the anisotropy and the *g*-factor, whereas by analysing the linewidth data one obtains information about the dynamic magnetic properties, like the damping and the inhomogeneous linebroadening.

The data recorded can be analysed by using the fit program, which was written by Michael Körner and myself. It has the capability to fit first the single spectra to obtain B_{res} and ΔB_{pp} [see Figs. 2.9](a) and (b)] and afterwards it can plot and fit the data obtained from these spectra fits with respect to either polar or azimuth geometry. Moreover, this software can determine the *g*-factor and the linewidth. All of the measurements presented were done in the polar geometry.

Figure 2.11 shows a typical such polar VNA-FMR measurement. The measured sample is a Cr (5 nm) / Py (20 nm) / Cr (2 nm) coated GaSb (001). The graphic shows the field plotted against polar angle. The red squares represent the single spectra results for the resonance field, whereas the blue line is showing the polar angle-dependent fit. At a first glance, one observes the difference between 0° and 90°. This shape is characteristic for an in-plane magnetised FM film. The maximum resonance field value at $\theta_B = 0°$ (out-of-plane) and the corresponding minimum field value $\theta_B = 90°$ (in-plane) reveal that the hard axis of magnetisation is oriented parallel to the film normal, whereas the easy axis lies in the film plane.

In order to understand the reason for the shape of the measurement curve it is necessary to consider the effect of the anisotropy on the sample's internal field for measurements in different directions. When measuring along the hard axis, the applied field must overcome the anisotropy field in order to rotate $\vec{M}$ into this direction. The resulting internal field is then reduced by the applied field so that in order to have the
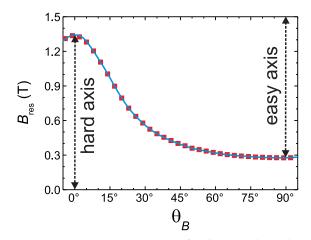
Fig. 2.11 Polar angular-dependent VNA-FMR measurement of a Cr (5 nm)/Py (20 nm)/Cr (3 nm) coated planar GaSb(001) wafer.

sample resonate at same frequency then the internal field must be increased by increasing the applied field, hence the resonance field is higher in this direction.

The next paragraphs explain the analysis of the *g*-factor and the linewidth data. Due to the fact that the field was measured in between the pole shoes, the conversion $\vec{B} = \mu_0 \vec{H}$ is required. Figure 2.12(a) depicts a frequency dependent measurement at $\theta_B = 0°$. The inset shows the process data after the single spectra fits. This geometry is crucial due to a simplification of the resonance condition (Kittel's formula) in the case of a measurement in the [001] crystallographic direction.[199–201] The resonance condition is given by

$$\frac{\omega}{|\gamma|} = \sqrt{B_{\text{res}}\left(B_{\text{res}} + \mu_0 M_{\text{eff}}\right)}, \qquad \text{where } \mu_0 M_{\text{eff}} = \mu_0 M_{\text{s}} - \frac{2K_{2\perp}}{M_{\text{s}}}. \tag{2.44}$$

The substitution $\mu_0 M_{\text{eff}}$ represents the effective magnetisation and is the most dominant contribution from the anisotropy system to the resonance condition. Figure. 2.12(a) shows a plot of f^2 versus B_{res}. The fit of these data will yield the Landé-factor.

Based on equation (2.43) one can also obtain the linewidth, Fig. 2.12(b) shows the linewidth analysis of such fitted single spectra. The transformation from the peak-to-peak field values ΔB_{pp} into the ΔB is $\Delta B_{\text{pp}} = 2/\sqrt{3}\Delta B$. The graph shows a plot of ΔB versus f_{res}. The blue points represent the evaluated data points and the red line the linear fit. The linear correlation of field and frequency reveals that the damping is limited to the Gilbert damping. The analysis of the linear slope will obtain the dimensionless Gilbert damping constant α. The equation for this linebroadening, according to the analysis of the FMR linewidth by Suhl and others[202–205] is given by

$$\Delta B = \frac{\partial B}{\partial \omega} \sum_{i}^{N} \left| \frac{\partial \omega}{\partial x_i} \right| \Delta x_i, \tag{2.45}$$

where x_i represents the different sample parameters which affect the resonance condition, e.g. the local direction of the film normal relative to the applied field. The contributions to ΔB typically used for the
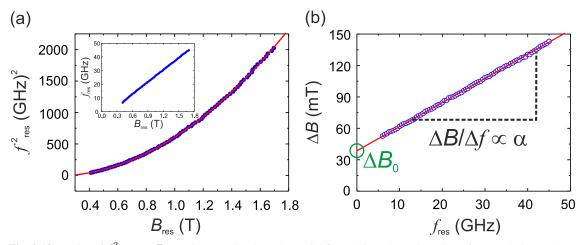
(a)

(b)

Fig. 2.12 (a) Plot of f^2 versus B_{res}. The second order polynomial fit (red line) determines the g-factor. The inset shows the original frequency-dependent VNA-FMR measurement. (b) Analysis of the measured linewidth. The graph depicts ΔB plotted versus the resonance frequency. The linear fit (red line) gives the dimensionless Gilbert damping parameter and the inhomogeneous linebroadening.

systems measured for this thesis are summarised by the following:

$$\Delta B = \underbrace{\Delta B^{\text{inhom}}}_{(1)} + \underbrace{\Delta B^{\text{Gilbert}}}_{(2)}. \tag{2.46}$$

The first two components of this sum consist of the damping parameter α and the inhomogeneous linebroadening ΔB_0 and are expressed by:

$$\Delta B' = \underbrace{\Delta B_0}_{(1)} + \underbrace{\frac{2}{\sqrt{3}} \frac{\omega \alpha}{|\gamma| \cos \beta}}_{(2)}, \text{ where } \beta = \theta_{\text{eq}} - \theta_{\text{B}}. \tag{2.47}$$

The β describes the so-called field dragging, which is defined by the angle between the external magnetic field and the magnetisation. Field dragging enhances the damping, as is shown by the cosine in the equation above. In the case of $\vec{B} \parallel \vec{M}$, which occurs when the field is orientated along the easy- and the hard axis, β is equal zero and, therefore, the cosine equals one.[205] Comparing the slope of the linear fit with (2.47), one can determine the Gilbert damping parameter (2). Moreover, the first term of equation (2.47) shows the frequency-independent inhomogeneous linebroadening ΔB_0 (1).[205] This value is determined by the y-intercept of the linear fit. This parameter gives information about the anisotropy dispersion due to lattice defects and other effects.[203,206,207]

The Magneto-Optical Kerr Effect (MOKE) magnetometry uses the influence of the magnetisation $\vec{M}$ of FM materials on the reflection of polarised light, where $\vec{M}$ changes the reflected intensity, as well as the polarisation. The complete theoretical background can be found elsewhere.[208–212]. In a measurement, a swept external magnetic field $\vec{H}$ modifies the magnetisation $\vec{M}$, which in turn changes the polarization of the reflected light. The computer then records this Kerr rotation angle with respect to the field strength. Therefore, one obtains a hysteresis loop from the measurement (compare with paragraph 2.1.4). The Kerr rotation angle is proportional to the magnetisation $\theta_{\text{K}} \propto |\vec{M}|$.[213–223] There are three main geometries that are used, and which explain the influence of magnetisation $\vec{M}$, normal vector $\vec{n}$, and incident plane $\vec{\Theta}_{ip}$, which is spanned by the incoming and reflected light on the properties of the reflected light.. They are called
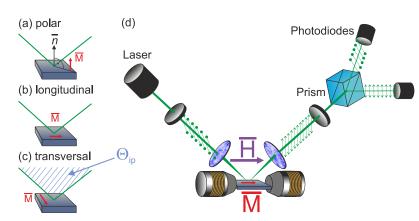
Fig. 2.13 Sketch of the MOKE geometries: (a) polar, (b) longitudinal, and (c) transversal. (d) Scheme of a MOKE setup, with polarisation change.[5]

polar (PMOKE, $\vec{M} \parallel \vec{n}$), longitudinal (LMOKE, $\vec{M} \perp \vec{n}$), and transversal (TMOKE, $\vec{M} \perp \vec{n} \wedge \vec{M} \perp \vec{\Theta}_{ip}$). In section 3.1 the in-plane angular-dependent measurements of the Cr (5 nm)/Py (20 nm)/Cr (3 nm) sample will be presented, which were measured with a LMOKE scan. This setup has the capability to measure the hysteresis loops over the complete cycle ($\varphi_H = 360°$). These MOKE measurements give information about the in-plane anisotropy and coercivity.

Time-Resolved Magneto-Optical Kerr Effect   (TRMOKE) is a technique based on the magneto-optical Kerr effect.[224,225], which detects the precession of excited magnetic moments. Its particular strength are the detection of ultrafast magnetisation processes and switching processes. The high time resolution comes from using an all-optical configuration for excitation of the spins and also for probing (a femtosecond laser can be used). It makes it possible to measure non-linear switching events by using a pump-probe method. In general it is possible to either use a short magnetic field pulse[136] or a laser pulse to excite the sample,[226,227] in the experiments done for this work all-optical excitation was used. Whereas, FMR detects the absorption spectra of a sample in the frequency domain using microwaves,[228] TRMOKE measures the response of $\vec{M}$ to a pulse in the time-domain.[229,230] The spectra can be transformed from the time-domain into the frequency-domain and vice versa by the Fourier transformation.

An technical advantage of TRMOKE is that it is sometimes possible to supply a higher energy to a focussed region of the system, this allows the excitation of even a highly anisotropic system.[231–233] Therefore, given by the equipment available, the CoCrPt:SiO_2 samples which have a high perpendicular anisotropy could be measured by this technique.[133,234,235,235]

The first part of this subsection introduces the setup. In the second part, basic information about the excitation process and the signal obtained, as well as the analysis of this signal will be given.

Figure 2.14 shows the scheme of the setup. Based on this sketch the TRMOKE setup will be introduced. The system used was developed and built by Dr. Christopher Bunce. The laser system is a conventional femtosource™ XL 500 titanium-sapphire laser, manufactured by femtolasers, with a wavelength of $\lambda_{fs} = 800$ nm. Due to the mode-locking regime in which the laser operates ultrashort femtosecond pulses with a duration of $\Delta t_{pulse} \approx 40$ fs were generated. Each pulse has an energy of $E_{pulse} = 500$ nJ/pulse. The output power is $P_{out} = 2.6$ W and the repetition rate is $R_{rep} = 5.2$ MHz. The laser beam is guided through a non-linear BBO (Barium borate oxide BaB_2O_2) crystal. In this optical device a portion of the beam energy is frequency doubled by second harmonic generation (SHG), the beam can now be considered to be composed of a probe beam which has a wavelength of $\lambda \approx 400$ nm and a pump beam of $\lambda = 800$ nm. Both beams leave

---

[5]adapted from http://www.physik.uni-kl.de/hillebrands/research/methods/magneto-optic-kerr-effect-magnetometry-and-microscopy/
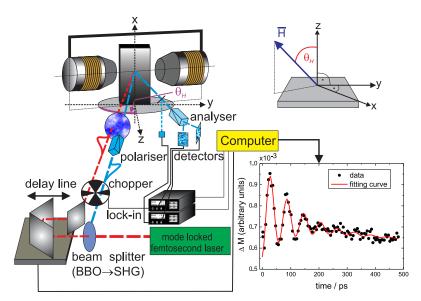
Fig. 2.14 Scheme of the pump-probe TRMOKE setup. [236] On the bottom right a measurement result is shown. In this graph the change of magnetisation is plotted versus time. The resulting data is fitted (red line) by the function (2.49).

the BBO and than a chromatic beam splitter divides them. To achieve a well-defined and adjustable time difference between the pump and the probe beam, a delay line was installed through which the pump beam is guided. Thus, a delay of up to 4 ns can be achieved. The delay line consists of a retroreflector mounted on a translation stage, allowing for a precise variation of the optical path length. This is a crucial point, because the pump beam has to hit the sample shortly before the incoming probe beam arrives in order to heat the region which will be probed. This yields an excitation of a precessional motion of the spins. After the delay line both beams are guided through a dual aperture optical chopper. This chopper is necessary in order to modulate the signal for the lock-in detection of the Kerr rotation and of the change of reflectivity. Afterwards, a pump power control unit is mounted in the pump beam line. This consists of two polarisers and a wave plate, which by their adjustment can be used to tune the applied power of the pump beam. This is important, because appplying a beam with a too high power density to the sample results in a ablation of material from the surface, which destroys the sample. In the probe beam line there is a single polariser mounted to optimize the polarization of the light incident on the sample. Before the probe beam is focussed onto the sample, it is split with one part being used to obtain a reference signal for the reflectivity measurement. Both beams are focussed by a Thorlabs™ AC254-75 achromat onto one spot on the sample. In order to guarantee a uniform excitation, the pump beam spot, which has a radius of 17 µm needs to be larger than the probe beam spot, which has a radius of 5 µm. Then the probe beam is guided to the detector. The pump beam is aligned so, that it will be reflected back parallel from the sample, where it is blocked. Before the probe beam reaches the detectors it is split into two beams. One is guided to an optical analyser, which splits the beam into two orthogonal polarisation parts, which is typically called an optical bridge detector. The two halves of optical bridge detector are connected to the lock-in amplifiers, where the difference signal is measured. The second part of the beam is used for the reflectivity measurement. The maximum external magnetic field that can be applied to the sample is about 1.3 T. This static magnetic field can be changed in both its strength and/or its orientation, which gives the opportunity to make angle-dependent measurements.

Figure 2.15(a) shows a sketch of an all optical TRMOKE system. [236,237] Basically, such a setup consists of a pump and a probe beam. [238,239] The pump beam is focussed onto the sample where it causes heating. The delay between the pump and probe can be varied to measure the magnetisation time-dependently. The energy
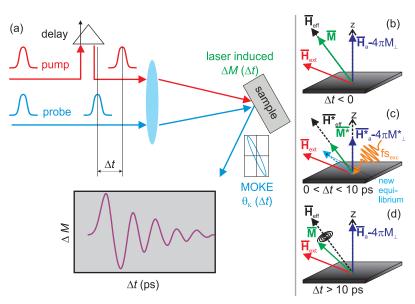
Fig. 2.15 (a) Sketch of an all optical pump excitation in a TRMOKE system. The red parts represent the pump beamline for excitation, whereas, the blue part shows the probe beamline.[230,237] Below, the shape of a typical signal is shown. (b)-(d) shows the TRMOKE optical excitation of coherent precession.[132,240] (b) shows the situation before the excitation ($\Delta t < 0$ s), the magnetisation points in the equilibrium direction, given by $\vec{H}_\text{eff}$; (c) shows the process shortly after the pump laser pulse ($0 < \Delta t < 10$ ps). The magnitude of $\vec{M}$ and the anisotropy is changed due to the laser induced heating, which causes an altering of the equilibrium orientation. (d) shows the damped precession of the magnetisation around the new equilibrium direction ($\Delta t > 10$ ps).[243]

injected by the pump pulse causes a reduction in the magnetisation. An illustration of the optical excitation process of coherent precession is shown in Figs. 2.15(b)-(d).[132,240] Before the excitation ($\Delta t < 0$ ps) the magnetisation $\vec{M}$ (green arrow) is pointing in the direction of the effective field (black arrow) $\vec{H}_\text{eff}$. The direction of $\vec{M}$ and $\vec{H}_\text{eff}$ represents the equilibrium direction (dashed line). In this scheme, $\vec{H}_\text{eff}$ is the resultant vector of the anisotropy field (blue arrow) $\vec{H}_\text{a}$ and the external magnetic field (red arrow) $\vec{H}_\text{ext}$ [see Fig. 2.15(b)]. Subsequently, the exciting laser pulse (orange) hits the sample ($0 < \Delta t < 10$ ps). Due to the injection of energy the system heats up locally. This induces a simultaneous change in the magnetisation $\overrightarrow{M^*}$ and the anisotropy field $\overrightarrow{H^*}_\text{a}$. This changes the equilibrium direction, which induces a torque acting onto $\vec{M}$ [see Fig. 2.15(c)]. This torque causes a change in the direction of $\vec{M}$. After the excitation the material can rapidly cool to the original temperature, this restores $\overrightarrow{M^*}$ and $\overrightarrow{H^*}_\text{a}$ to their original values. The magnetisation will then make a damped precession around the initial equilibrium direction. Therefore, the reflected probe pulse will change its polarisation (Kerr rotation), which can be detected. Below the sketch of a typical measurement result is shown. In this graph the change of the magnetisation is plotted versus time. The shape of the curve is that of an exponentially damped sinusoidal harmonic oscillation.[240–242] A Fourier transformation of such a signal will give a Lorentzian-like absorption curve. Due to the fact that the Kerr rotation is proportional to the change in magnetisation (compare paragraph 2.2.3) one can assume the typical fit equation for the resulting signal to be an exponentially damped sinusoidal oscillation, as was mentioned previously.[242] The resulting equation is then:[134,227,244,245]

$$\Delta\theta_\text{Kerr}(t) \propto \Delta M_\text{fit}(t) \propto \sin(\omega t + \varphi)\exp\left(-\frac{t}{\tau}\right). \tag{2.48}$$
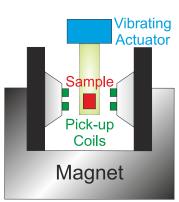
Fig. 2.16 (a) Sketch, which depicts the basic principle setup for a vibrating sample magnetometer. In case where the sample or the magnet is rotatable, the setup provides the property of angular-dependent measurements and is then called a vector vibrating sample magnetometer.

The empirically determined fit equation is the following:

$$\Delta M_{\text{fit}}(t) = A_0 + A_1 \sin\left(\omega t + \varphi\right) \exp\left(-\frac{t}{\tau_1}\right) - A_2 \exp\left(-\frac{t}{\tau_2}\right). \tag{2.49}$$

In this equation (2.49) the following parameters were used: A_i (i=1,2) represents the amplitudes, A_0 is the offset, $\omega = 2\pi f$ is the frequency, t the time, φ the phase, and the τ_1 represent the decay parameter. The second exponential decay term with τ_2 represents the cooling down after the thermal excitation by the pump beam. After the data were fitted the analysis can be continued by evaluating the frequency, decay time, and the damping. The latter can be determined by making use of the relation[234,241]

$$\alpha \cong (\omega\tau)^{-1}. \tag{2.50}$$

One has to keep in mind that this relation is only valid under the assumption of a small angle precession which is circular. This condition is fulfilled in the case of a measurement of an out-of-plane magnetised sample, because of the requirement that the variation in $\vec{M}$ along the direction of $\vec{H}_{\text{eff}}$ to be negligible and that the phase of the x and y component of $\vec{M}$ to be orthogonal. Whereas, larger in-plane magnetisation excitation have a much more complex expression. The values for the resonant frequency obtained from these measurements can be fitted by the same Matlab program that was used for the FMR analysis, which uses the resonance condition derived from the free energy,

Vector Vibrating Sample Magnetometry   With the vibrating sample magnetometer (VSM) one can measure hysteresis loops (see subsubsection 2.1.4).[246–248] These measurements were carried out either by Dr. Gaspare Varvaro, using a vector-VSM (Model 10 EDA-Technologies™),[249,250] which allows one to additionally measure the angular dependence, or by Dr. Denys Makarov, using a conventional VSM setup. When making these measurements a sample is placed between two electromagnet pole shoes inside a uniform external magnetic field. The sample has to be vibrated sinusoidally inside a magnetic field. Pick-up coils are placed in the vicinity around the sample, so that the induced voltage can be measured. This voltage is proportional to the net magnetic moment of the sample. The signal is improved by using a lock-in amplifier with the exciter signal as a reference.[251,252] The angular-dependence is possible due to the rotating of the sample holder. Therefore, it is possible to measure in azimuthal ($\vec{B}$ aligned in-plane), as well as in the polar geometry ($\vec{B}$ aligned out-of-plane, see paragraph 2.2.3). The overview of a VSM setup is shown in Fig. 2.16. The main advantages of this technology are the lower costs and the faster measurements. In comparison to
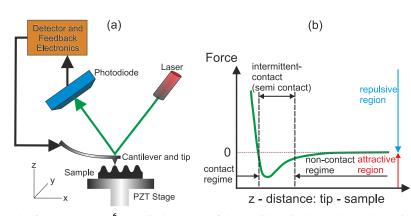
Fig. 2.17 (a) Sketch of an AFM setup.[6] The displacement of the cantilever is detected by a laser via a photodiode. (b) depicts the different operation modes of AFM and MFM.[7]

the SQUID or to the MOKE technology the VSM signal typically shows the lowest sensitivity per spin.

Superconducting Quantum Interference Device The superconducting quantum interference device (SQUID) provides the highest sensitivity magnetometry.[253,254] This technique makes it possible to achieve measurements even down to a change of magnetisation of 5×10^{-18} emu. The operation mode of a SQUID is based on the Josephson effect[255,256] Basically, the SQUID sensor measures the magnetic stray field of a sample. In this work it was mostly used to determine the saturation magnetisation of the samples. The advantage of the conventional setup (MPMS-XL7 from Quantum Design International™) has a maximum applied magnetic field of 7 T due to the use of a superconducting magnet. This field has the capability to saturate even a CoCrPt:SiO$_2$ sample with its high out-of-plane anisotropy along its hard axis.

2.2.4. Structural Investigation Techniques

To obtain structural information about the samples prepared, different techniques were utilised. By using the electron microscopy techniques, one obtains the characteristic length, the height, the diameter, the distribution of the structure, and the quality, as well as the distribution of the coating. Whereas, by atomic- and magnetic force microscopy, one investigates the correlation between the underlying structure and the magnetic domains.

Atomic Force Microscopy (AFM) is a scanning microscopy technique with a resolution in the nanometre regime and below.[257–259] Its advantage when compared to scanning electron microscopy is that one obtains a three dimensional surface image. In principle the AFM consists of a small tip mounted on a cantilever, whose deflection is detected by a laser via a quadrant photodiode. In operation the tip is rastered over the sample surface by a x-y-z piezo drive [see Fig. 2.17(a)].[260] The AFM setup is working in the tapping mode™ [8] (semi- or intermittent contact mode, see Fig. 2.17).[261,262] Using a piezoelectric element mounted in the AFM-tip holder the cantilever is driven to oscillate near its resonance frequency. The surface interactions, like the Van der Waals-, electrostatic forces, and the dipole-dipole interactions cause a decrease in the oscillation amplitude related to the interacting force.[263] Therefore, imaging is caused by the forces between the intermittent contacts of the tip and the surface.

---

[7]adapted from `http://commons.wikimedia.org/wiki/File:Atomic_force_microscope_block_diagram.svg`
[7]adapted from `http://www.nanoscience.com/education/afm.html`
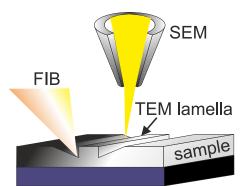[8]Digital Instruments

Fig. 2.18 Principle of TEM lamella preparation by focussed ion beam.

Magnetic Force Microscopy (MFM) has evolved from AFM by using a magnetic tip. In Fig. 2.17(c) the principle of an MFM is depicted. In contrast to the AFM this method provides information about the local magnetisation.[264–266] The scanning mode typically used is non-contact [see Fig. 2.17(b)]. Usually, the measurement scan needs two cycles. The first records the height profile as for a typical AFM. Whereas the second run, at a fixed distance from the surface, records the magnetic interaction of the tip and surface. The reason for this double scan is to avoid the influence of the dominant but short-range van der Waals interaction. The magnetic force is a long-range interaction which is weaker. By using a ferromagnetic tip, which is sensitive to the stray field $\vec{H}$ between the individual domains, one achieves a magnetic stray field map of the surface.[267] The mathematical expression for the force between sample and tip is: $\vec{F}_{t-s} = \mu_0 \left(\vec{m} \cdot \nabla \right) \vec{H}$. Furthermore, the magnetic properties of a 3-dimensional structure can be measured. Note, that the shape and size of the tip limits the resolution.[268]

Focussed Ion Beam and Scanning Electron Microscopy (FIB-SEM) provides direct information about the surface topography. This technology differs from TEM due to the manner in which the beam is applied to the specimen and its detection method. The beam is focussed onto the sample surface and by using a deflection coil the beam scans over the sample in a defined raster. The detector uses mainly the backscattered and the secondary electrons for imaging.[269] Therefore, this technology images the surface topography of a specimen. The focussed ion beam unit in Fig. 2.18 is a crucial device that is used for the TEM specimen preparation. By using a focussed ion beam a thin cross-section specimen could be cut out of the surface by controlling the procedure simultaneously via the SEM.

Transmission Electron Microscopy TEM provides information about the internal structural conditions of a sample.[270,271] The basic operation principle is the following: an electron beam is guided by electromagnetic lenses onto the sample. Usually, this beam is broader than the sample. The electrons pass through the sample, which has to be extremely thin to improve the contrast. Therefore, the sample preparation is a crucial point for this method. Afterwards, the transmitted electrons are collected and imaged onto a fluorescent screen or a charge-coupled device (CCD) camera by electromagnetic lenses, to obtain an image of the structural conditions. In this work most images are so-called cross-sectional high-resolution TEM images, which were obtained by using a FIB [see Fig. 2.18] to create an appropriately thin cross-section which then allows one to take advantage of the high resolution achieved by the aberration correction optics in the TEM. Here, all of the TEM measurements presented were carried out by Monika Fritzsche.
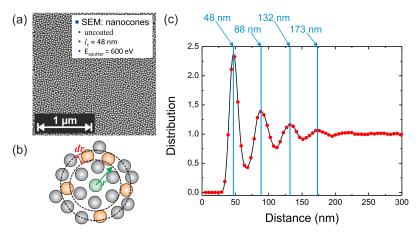
Fig. 2.19 (a) Scanning electron microscopy image of a GaSb(001) sample sputtered with $E_{\mathrm{kin}} = 600$ eV. (b) Sketch of PCF evaluation. It depicts the structures counted (orange) with respect to the middle cone (green).[274] (c) depicts the analysed PCF plot for this sample. Every peak represents the next counted nearest neighbour distance. In addition, the values are shown on top of the plot (blue).

2.2.5. Pair Correlation Function

The analysis of the nanocone distribution of the prepared sample series was carried out using the pair correlation function approach.[272,273] This analysis program was implemented in Matlab by Roman Böttger,[274] and this approach gives both qualitative and quantitative information about the short- and medium-range order of point structures.[275–277] In a first step, one has to input a SEM image to the program and enter the SEM magnification in order to identify length scales in the image [see Fig. 2.19]. Subsequently, the image is automatically processed by the steps of noise reduction, contrast enhancement, thresholding for conversion to a binary image, removal of small objects and identification of pixel-connectivities to finally get the coordinates of the point centres.

In the last step the pair correlation function of these point centres is calculated. This is done for each point by counting how many points are found at a certain distance. The resulting pair correlation function is then the conditional probability density of finding another point at a radial distance r from any other point. Therefore, the PCF of an ideal ordered array will consist of peaks, which are centred at characteristic positions. The integral of these peaks at the characteristic positions is equal to the number of dots that are found at the 1st, 2nd, 3rd, ... nearest neighbour positions. Evaluation of short-range order can be done by comparing the integral

$$P\left(r_i, r_a\right) = 2\pi\rho \int_{r_a}^{r_i} g\left(r\right) r dr \tag{2.51}$$

of the PCF to the value of the ideal array.

For example, the evaluation of a GaSb(001) sample sputtered with $E_{\mathrm{kin}} = 600$ eV is shown in Fig. 2.19. The values determined for the nearest neighbours are 48 nm, 88 nm, 132 nm, and 173 nm. The first one represents the characteristic length l_c. This values leads to the series of relations $r_{\mathrm{PCF}}^{\mathrm{hex}} = 1, \approx \sqrt{3.35}, \approx \sqrt{7.56}, \approx \sqrt{12.99},...$. An ideal hexagonally ordered cone structure would show the following series: $r_{\mathrm{ideal}}^{\mathrm{hex}} = 1, \sqrt{3}, 2, \sqrt{7}, 3, \sqrt{12}, \sqrt{13}, 4,...$. Therefore, the values obtained could be compared and a short-range hexagonal ordering between the two first degrees of the nearest neighbour's radii is observable to within an error of 0.5. The short-range order information can be determined either by analysing the decrease and broadening of the peaks in the distribution, an example of which is shown in Fig. 2.19(c). An increase in the width of the peaks implies a decreasing of the ordering with regards to the radius.

Chapter 3.

Experimental Investigations

In this section we discuss the experimental results with a focus on the changes in the magnetic properties which result from the sample processing, such changes can be due to morphology modifications, or the changes can be caused by ion-induced intermixing effects. The morphology-induced effects were studied on samples where the substrate surfaces were ion eroded in order to obtain a nanocone structure. The following magnetic parameters were measured: the anisotropy, the damping, the inhomogeneous linebroadening, the g-factor, the remanence, the coercivity, and the saturation magnetisation. In addition, the effects on the intergranular and interdot exchange coupling were investigated. The first part of this chapter presents the results of the sample series which has nanocone structured surfaces coated with a Cr (5 nm)/Py (20 nm)/Cr (3 nm) film. Subsequently, the measurements concerning the three different investigations of CoCrPt are presented. This includes the studies of the reference measurements on the planar CoCrPt reference samples. Afterwards, the measurements of the Co$^+$ ion implanted planar CoCrPt:SiO$_2$ will be discussed. The section is concluded by a subsection about CoCrPt:SiO$_2$ on nanocones. The subject of the last part of the chapter is nanocones with a [Co/Pd] coating. Here, we also study the interplay between morphology and magnetic properties.

3.1. Cr (5 nm)/Py (20 nm)/Cr (3 nm) Film on Nanocones

The investigations of the GaSb(001) nanocones coated by a Cr (5 nm)/Py (20 nm)/Cr (3 nm) stack aimed to determine the influence of the morphology modification on the magnetic properties. For this purpose, two morphologies were studied: a two dimensional flat FM thin film which was compared to a 3-dimensional FM structure deposited onto a self-assembled array of GaSb nanocones.

3.1.1. Preparation and Structural Investigations

The GaSb(001) nanocones were prepared using the IET (see paragraph 2.2.1). The particular sputtering parameters used are summarised in Tab. 3.1. In the following we will refer to the samples by their sample number as specified in Tab. 3.1.

The first characterization concerning the cone structure was done using TEM before the film deposition step. The aim was to observe the amorphous surface layer which is formed by the sputtering process [see Fig. 3.1]. Due to the presence of this layer, one has to first deposit a seed layer in order to define a crystallographic orientation for the epitaxially growth of the FM film.

Before the FM film was deposited onto the nanocones, the structural parameters, l_c and the ordering were determined using SEM. The images obtained were analysed using the PCF (see section 2.2.5) program to extract these parameters. The results are shown in Fig. 3.2. An increase of l_c with increasing E is observed. The resulting values range between 35.7(8.8) nm ($E = 100$ eV) and 48.1(6.8) nm ($E = 600$ eV). These values are shown in the first column in Tab. 3.1.
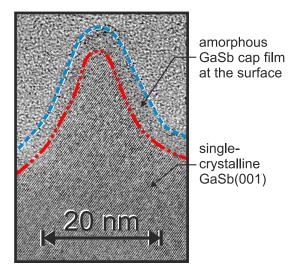
Fig. 3.1 Cross-sectional HR-TEM of an uncoated GaSb(001) sample sputtered at $E = 150$ eV ($l_c \approx 27(5)$ nm). The region between the red and the blue line shows the small amorphous GaSb layer caused by the sputtering process. Below the red curve the single-crystalline GaSb(001) is visible. The lines are just guides for the eyes.

In Fig. 3.2, the first value shown (red) is the result for the analysis of the planar sample NP0. The SEM and TEM measurements show a significantly higher roughness of the planar sample as compared to the sputtered samples NP1-NP6, as depicted in Fig. 3.3. The TEM image of NP0 shows, that the surface is covered by small fragments ($h_{\text{fragments}} \approx 13$ nm, see Fig. 3.3(a)) of GaSb. All these fragments have a similar height, as shown in the TEM image. The origin of these fragments seems to be the cutting process,[1] which is difficult because GaSb is a brittle material. Cleaning the samples after the cutting does not solve this problem. Compared to the size of the nanocones on the structured samples, the height of the fragments is small. But, as indicated by the PCF results, the characteristic lengths are similar ($l_c = 25.8(11.3)$). However, compared to the l_c values of the pre-structured samples, the planar sample has a larger error bar, which indicates the lesser ordering of the fragments. This finding that the NP0 sample seems to have an odering of the fragments is surprising (see Fig. 3.2). One might expect that the fragments should be randomly distributed over the region analysed. This observed ordering process might be interesting for further investigation, as presumably

---

[1]Newer results that have been analysed by my colleague Monika Fritzsche indicate that the fragments might be at least partially caused by oxidation.

Tab. 3.1.: Ion beam erosion preparation parameters for the pre-structured GaSb(001) sample series.

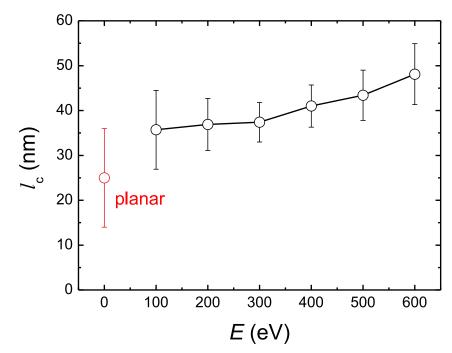| Sample number (N°)	E (eV)	fluence ($10^{17} \frac{\text{Ar}^+}{\text{cm}^2}$)	flux ($10^{14} \frac{\text{Ar}^+}{\text{cm}^2 \times \text{s}}$)	current (mA)	time (min)	characteristic length l_c (nm)
NP0	0	0.0	0.00	0.00	0	25.8(11.3)
NP1	100	4.1	2.00	0.43	33	35.7(8.8)
NP2	200	10.0	5.00	1.10	33	36.9(5.6)
NP3	300	10.0	7.50	1.63	22	37.4(4.4)
NP4	400	10.0	5.00	1.10	33	41.0(4.7)
NP5	500	10.0	5.00	1.10	33	43.4(5.6)
NP6	600	7.5	3.75	0.82	33	48.1(6.8)

Fig. 3.2 PCF Analysis of the SEM images of the Cr (5 nm)/Py (20 nm)/Cr (3 nm) sample series. The l_c increases with an increasing E. The line is just a guide for the eye. The red data point represents the planar sample and gives the roughness of the original GaSb(001) wafer.

it involved some sort of self-assembling effect. In addition to the fragments, one can observe a small surface roughness, as shown in Fig. 3.3.

The FM Cr (5 nm)/Py (20 nm)/Cr (3 nm) stack was deposited onto the structured substrate using MBE (see paragraph 2.2.2). A 5 nm thick Cr film was chosen as a seed layer and the FM film was a 20 nm thick Py layer. The capping layer consists of 3 nm Cr to avoid oxidation. This particular stack was chosen because of its simple composition and for its well-known magnetic properties, the knowledge of which was crucial for subsequent OOMMF simulations of the hysteresis loops. After the deposition, one more TEM image was taken to show how the film had grown onto the nanocone structures. The results are shown in Fig. 3.4(a) and (b). In Fig. 3.4(a) the high resolution TEM image shows the polycrystalline growth of the Cr (5 nm)/Py (20 nm)/Cr (3 nm) deposited stack. The overview in Fig. 3.4(b) shows the uniformity of the underlying nanocone structure. Furthermore, it is possible to observe that the coating is completely covering the structure. The images indicate that the layers of the entire film have a polycrystalline structure, because in the HR-TEM image no change in the crystallography between the different layers is observable.
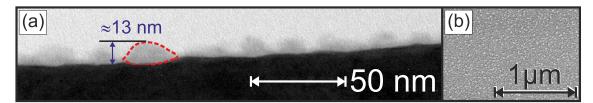

Fig. 3.3 (a) TEM image of a virgin planar GaSb(001) sample (NP0). (b) SEM image of the NP0 sample.

3.1.2. VNA-FMR Measurements

Afterwards, the morphology-induced changes of the magnetic properties were determined. The first measurements were done using the VNA-FMR setup. These measurements were carried out by varying the polar angle θ_B. During such a measurement the electromagnet turns around a sample that is held fixed against the planar waveguide. The magnetic field rotates from $\theta_B = -5°$ (out-of-plane) to $\theta_B = 95°$ (in-plane), due to the symmetry of the anisotropy system this range is sufficient. The samples were measured at a fixed frequency of 15 GHz whilst sweeping the field from -0.01 T up to +1.49 T ($[\mu_0 M_s]$ (Py) $= 1.016$ T[105]). The reason for starting from a negative external magnetic field is to compensate for the remanence of the electromagnet. Subsequently, the results were analysed using the Matlab program, which determines the resonance field B_{res} at each angle θ_B by fitting the corresponding spectra with a Lorentzian curve.

Determination of the Anisotropy. Figure 3.5 shows the resonance field at each angle measured between $\theta_B = -5$ to $95°$. The shape of the curves can be described as follows. Starting with the NP0 (black boxes) curve, which belongs to the planar sample, one observes a clear peak on the left side at $0°$ and the lowest resonance field value at $90°$. Therefore it can be concluded, that the easy axis of magnetisation of this planar sample lies in-plane, which is a well-known result for a flat Permalloy thin film due to the shape anisotropy.[278] Each data point shown in Fig. 3.5 represents the applied field required to satify the resonance condition (frequency is 15 GHz for all measurements). These data points where measured for diffent field direction, for each point the applied field is high enough to saturate the sample in that direction. This means that all spins are directed along the applied field. The value of B_{res} required to satisfy the resonance condition is indicating the restoring force (effective MAE) on the magnetisation. In the case of a isotropic system the restoring force for all angles is the same, therefore B_{res} is angle-independent. As one can observe in Fig. 3.5 from the NP0 to NP6 the variation in B_{res} becomes smaller and so it can be concluded from the graph that with increasing l_c the sample become more isotropic. When comparing the curve of the NP0 sample with the ones for the nanostructured samples NP1–6, one can obeserve a decrease in the resonance field values around the $0°$ angle and an increase of the value at $90°$. This equalization of B_{res} becomes more extreme as the value of l_c increases, this indicates both that the sample is isotropic and that the magnetisation follows the curvature of the nanocones. To expand on the latter statement, this equalisation effect shows that the easy axis of magnetisation is changing its direction. One can condsider the possibilties for the orientation of the easy axis, it is known that Py has an in-plane easy axis and therefore is restricted in orientation. Due to the equalisation of B_{res} with respect to the field angle, this indicates that the easy axis has a spread of angles which has to be in between in- or out-of-plane of the sample. This reasoning leads to the belief that the easy axis follows the local surface curvature. Further justification for the last statement will be provided in the follwing, once more results and simulations relevant to this issue have been presented.

The FMR analysis software provides a further fitting routine, where the polar measurements can be fitted by making use of the general resonance condition with respect to the Gibbs free energy of the analysed system. The derivation of this condition is shown in detail in appendix A. In the case of the Cr (5 nm)/Py (20 nm)/Cr (3 nm) stack we used the resonance condition for an fcc tetragonal distorted system which is suitable because this kind of model has the right symmetry. In Tab. 3.2 the resulting best fit parameters are presented. Furthermore, in Fig. 3.6 the decrease of the effective magnetisation $4\pi M_{eff}$ with respect to an increase of l_c is shown. The $4\pi M_{eff}$ (see Equation (2.44)) is mainly given by the difference extrema of B_{res} (see Fig. 3.5). $4\pi M_{eff}$ is the difference between shape anisotropy and first order magnetocrystalline anisotropy. Because the magnetocrystalline anisotropy is for Py negligible small compared to the shape anisotropy of a thin film and therefore $4\pi M_{eff} = 4\pi M_s$. Also it has to be noted that
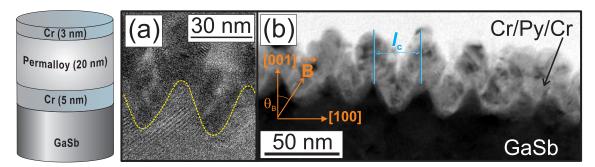
Fig. 3.4 TEM images of the NP2 sample ($E = 200$ eV/$l_c \approx 37$ nm). On the left side the schematic stack is shown. (a) cross-sectional HR-TEM image of the Cr (5 nm)/Py (20 nm)/Cr (3 nm) stack deposited on top of the nanocone structure. (b) TEM overview image. The orange coordinate system shows the orientation of the polar angle with respect to the crystallographic orientation. The blue coloured lines depict the characteristic length.

the saturation magnetisation in the material does not change. The decrease of $4\pi M_{\mathrm{eff}}$ can be explained by the change morphology because the Kittel's assumption of a homogeneous infinite thin film is no longer valid and due to the pattern the demagnetizing tensor is different.

Except for the $4\pi M_{\mathrm{eff}}$ values evaluated, the other $2K_i/M_s$ field values do not yield a correlation between the anisotropy fields and the increasing of l_c. This leads to the conclusion, that only $4\pi M_{\mathrm{eff}}$ can be tailored using this sort of modification to the morphology.

Determination of the *g*- Factor.   This is done using a further measurement, where the sample was orientated in the out-of-plane direction and the frequency was swept in steps of 0.5 GHz from 1 to 40 GHz. For each frequency the field was swept in the range of $B = -0.01 - 2.21$ T. By the use of this geometry the resonance condition is simplified, so that by a linear fit the slope can be determined, which is proportional to the *g*-factor.[113,205,279] The spread in the values determined is random which means that the spread in the *g* parameter is not correlated with the l_c parameter. The averaged value for the *g*-factor is *g* = 2.10(4). This value is similar to values known from the literature.[101,104,105]. This result was expected due to the fact that the dominant influence on the *g*-factor is the crystallography of the deposited film. Had there been a correlation between l_c and *g*this would indicate a change in the way the film grows (due to the morpholgy, e.g. by induced strain).

Determination of the Dynamical Aspects.   VNA-FMR measurements were carried out at $\theta_B = 90°$ and $\theta_B = 0°$ to obtain information about possible differences in the damping constants caused by the underlying nanocone structure. The frequency was swept between $f = 1 - 40$ GHz (steps: 0.5 GHz) and for each

Tab. 3.2.: Table of anisotropy fields and *g*-factors with respect to the cone size obtained by fitting the resonance condition of a fcc tetragonal distorted system to the measurements (see appendix A).
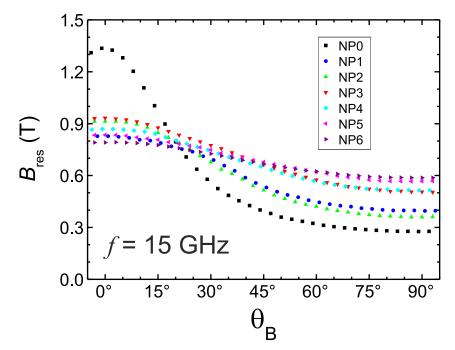
Sample number (N°)	$4\pi M_{\mathrm{eff}}$ (kG)	$2K_{2\parallel}/M_s$ (kOe)	$2K_{4\parallel}/M_s$ (kOe)	$2K_{4\perp}/M_s$ (kOe)
NP0	7.7	0.00	-0.28	0.00
NP1	4.6	-0.02	1.64	-0.38
NP2	4.1	-0.56	-0.02	0.52
NP3	3.7	0.42	0.54	0.00
NP4	2.5	0.00	0.06	0.00
NP5	2.2	0.66	-0.10	0.24
NP6	2.0	0.00	-0.48	-0.42

Fig. 3.5 Overview of the entire polar VNA-FMR measurements of the NP samples.
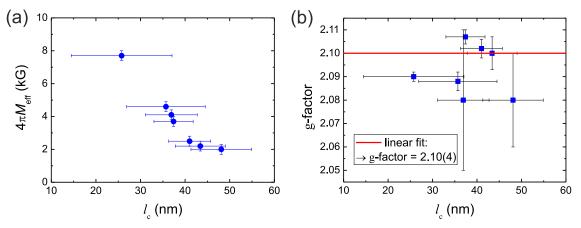

Fig. 3.6 (a) Graph of $4\pi M_{\mathrm{eff}}$ versus l_{c} . (b) g-factors for each sample and the linear fit (red line). The g-factor was determined to be 2.10(4).

frequency the field between $B = -0.01$ — 2.21 T. Subsequently, the spectra obtained were fitted to evaluate the ΔB_{pp}, which describes the peak-to-peak linewidth. [228,280]

The linear increase of ΔB_{pp} with respect to frequency (see Fig. 3.7(a) and (b))indicates a Gilbert like damping. In Fig. 3.7(a) one can find the ΔB_{pp} versus f_{res} plotted for the out-of-plane measurement geometry ($\theta_B = 0°$). Figure 3.7(b) shows the same measurement for the in-plane geometry ($\theta_B = 90°$). The intersection of the fitting curves and the y-axis defines the value of the inhomogeneous linebroadening (ΔB_0). Contrary to typical behaviour, the values for the slopes and the spread in values of ΔB_0 of the measurements shown here reveal a different picture. Obviously, the slope and ΔB_0 is changed significantly by changing the morphology.

A further analysis of the linewidths determined is depicted in Fig. 3.7(c) and (d), the underlying data can be found in Tab. 3.3, as well as in Tab. 3.4. On closer examination, one can see an unusual behaviour regarding the damping data [see Fig. 3.7(c)]. For both the damping and the inhomogeneous linebroadening data, the

plot for the oop geometry (blue triangles down) shows a only slight change in value with l_c (when compared to the ip data). By averaging these values one obtains a Gilbert damping constant of $\langle \alpha^{\mathrm{oop}} \rangle \approx 0.005$.[281] The same can be done for the values of the inhomogeneous linebroadening yielding $\langle \Delta B_0^{\mathrm{oop}} \rangle \approx 60,2$ Oe. Both values are similar to values reported in the literature for flat thin Py films.[104,281,282] The measurements in the in-plane geometry (red triangle up) reveal a significant influence of l_c [see Fig. 3.7(d)] on the damping. At a first glance, one observes a distinct increase in the damping for $l_c > 40$ nm [see Fig. 3.7(c)]. Below this threshold the values are similar to those from the oop measurements [see Fig. 3.7(c)]. The averaging of the values associated with the smaller l_c ($l_c < 40$ nm) give a $\langle \alpha^{ip} \rangle \approx 0.010$. This value can be considered to be equal to typical values for a flat thin Py film.[283,284] The values for the case where l_c is greater than 40 nm are emphasised in Fig. 3.7(c) by a green transparent region, show that the size of the cones begin to play a dominant role. From the evaluation of the α, which is based on the resonance condition for the ferromagnetic resonance,[179,181,185,228] this behaviour can be regarded as an effective Gilbert damping (α_{eff}). The resonance condition used presupposes a uniformly magnetised infinite continuous film. At a certain cone size this premise can most likely not be fulfilled anymore. Therefore, a new formula needs to be derived, which is suitable for describing the resonance condition for a modified surface structure like the nanocones. Moreover, the inhomogeneous linebroadening observed for the ip-measurements yields much higher ΔB_0 values. The average of the values determined for the structured samples[2] lead to a $\langle \Delta B_0^{\mathrm{ip}} \rangle \approx 525.9$ Oe. This value differs significantly from the literature.[204,207] Furthermore, this considerable deviation plus the spread of ΔB_0^{ip} leads to the assumption, that the inhomogeneous linebroadening has to be treated as an effective $\Delta B_{0,\mathrm{eff}}^{\mathrm{ip}}$, as well.

In summary there are three main effects which should be discussed further: (i) First the observation that the oop and ip measurements are so different is unexpected. Due to the increasing isotropic behaviour with increasing l_c(as seen from Fig. 3.5), one would expect that for the structured samples with larger l_c the difference between both geometries is decreasing. (ii) Although one would expect a difference in the values of ΔB_0 the magnitude in the difference is surprising because typical values from the literature are in the region of 10 Oe.[281,285] Whereas the values measured for the ip geometry are in the oder of magnitude of about 500 Oe. A reason for this behaviour could be that the change of morphology leads to a significant non-uniformity of the sample surface which enhances the inhomogeneous linebroadening. (iii) In particular, the increase in the damping for $l_c > 40$ nm is interesting. Given that the measurement and analysis technique used (ΔB versus f) allows the Gilbert damping to be a separated from the inhomogeneous linebroadening, the increase of α cannot be accounted for by the inhomogeneity of the magnetic film. Because the nanocone pattern is not expected to be cause of a change in the crystalline structure, which is also supported by the observation that the g-factor is nearly constant. Thus, the effect of the increase of α with increasing l_c has to be tributed to the change in shape of the film.

A more detailed investigation would have to take a step back. The morphology-induced effects could be determined by analysing an individual structure (i.e. starting with one cone) and subsequently increasing the system complexity to that of a small cluster by making additional use of simulations. This step-by-step procedure could help to determine a new resoance condition, which extended to the behaviour of such 3D magnetic films.
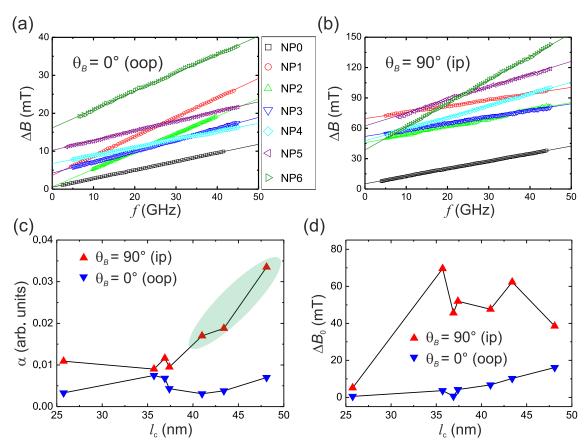
Fig. 3.7 Frequency-dependent VNA-FMR measurements (a) $\theta_B = 0°$ (out-of-plane): ΔB versus f. (b) $\theta_B = 90°$ (in-plane): ΔB versus f. (c) Gilbert damping parameter α versus l_c. The light green area emphasize the significantly increasing α. (d) inhomogeneous linebroadening with respect to l_c. The black lines just guides to the eyes.

3.1.3. MOKE Measurements

We investigated the possible existence of an in-plane anisotropy by carrying out an in-plane MOKE scan [see Fig. 3.8(a) and (b)]. The scanned azimuth angle region was $\varphi_H = 180° - 0°$. The data could only be analysed for the samples NP0 up to NP4, due to an increasing influence of the structured surface on the reflectivity which led to a decrease of the signal. The data was analysed using the *AnalyseHyst* LabVIEW™-software. This software was programmed by Michael Körner.

The results obtained for M_r/M_s and H_c are shown in Fig. 3.8(a) and (b), respectively. Only the resulting

---

[2]The ΔB_0 for the planar sample, is similar as shown in the oop-measurements.

Tab. 3.3.: Table of the slope of the linear fit, the evaluated Gilbert damping α, and the inhomogeneous linebroadening ΔB_0 measured at $\theta_B = 0°$ (oop).

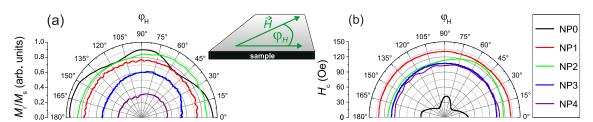| Sample number (N°)	slope of the linear fit (arbitrary units)	α (arbitrary units)	ΔB_0 (mT)
NP0	2.26(1)	0.003	0.53(1)
NP1	5.11(2)	0.008	3.64(2)
NP2	4.65(2)	0.007	0.61(2)
NP3	2.93(1)	0.004	4.23(2)
NP4	2.12(1)	0.003	6.74(3)
NP5	2.56(1)	0.004	10.23(2)
NP6	4.84(2)	0.007	16.14(6)

Fig. 3.8 Angular-dependent MOKE scans of the samples NP0 - NP4 in-plane ($\varphi_H = 180° - 0°$) (a) Results of the normalised remanence M_r/M_s. (b) Results of the coercivity H_c.

plot for the NP0 sample (black) reveals a slight fourfold anisotropic behaviour in both figures. The height of the fragments is about 5 nm, which is the same as the seed layer thickness of the Cr. Potentially, the imperfections on the surface and the crystallographic orientation of the planar GaSb(001) lead to an epitaxial growth of the deposited film stack, which results in the observable fourfold anisotropy. To verify this last proposal a planar GaSb(001) reference sample, which has been sputtered briefly to get rid of the fragments on top of the surface, should be prepared with the Cr (5 nm)/Py (20 nm)/Cr (3 nm) stack deposited on top of it. If the origin of the anisotropy is related to the presence of the fragments then a MOKE measurement should show an isotropic behaviour for the curve in both of the graphs shown in Fig. 3.8(a) and (b). Unfortunately, the TEM images showing the fragments on the planar surface were measured at a time where a new sample series could not be prepared anymore. But the statement regarding the influence of the fragments is supported by a comparison with the results of the pre-structured samples NP1-NP4. These samples, due to the structuring process consist of a small (< 5 nm) amorphous GaSb film on the surface. Furthermore, the imperfections were removed by the ion erosion. All of these pre-structured samples show an isotropic behaviour in both graphs. This leads to the conclusion that the amorphous film on the surface leads to the polycrystalline growth of the Cr and Py layers. Therefore, as expected for a polycrystalline Py film, these samples show an isotropic behaviour in the hysteresis curves analysed, in contrast to the result for the planar reference sample. The result for the planar sample shows the anisotropy axis as being rotated by about 5° from the 0°, 90°, and 180°directions, as shown in Fig. 3.8(a) and (b). This can be explained by a small misalignment of the sample on top of the sample holder inside the MOKE setup which is done by eye.

One can also further examine the behaviour of the normalised remanence and the coercivity. In Fig. 3.8(a) the normalised remanence is showing that in case of the NP0 to NP3 samples are rather similar in value, however, these measurements reveal a large spread within the values. Whereas, NP3 and NP4 show a significant decrease in M_r/M_s. This trend might be linked to the observed behaviour within the in-plane FMR measurements of the Gilbert damping (see Fig. 3.7). This will be discussed in more detail together with the simulation results in next section. In Fig. 3.8(b) the coercivity is shown, and it reveals a different pattern. At a first glance, one observes that NP0 behaves completely differently, having a significantly smaller value compared to the other samples. For the other sample there is a slight decrease in value from NP1 to NP4, but this trend is most significant for the NP1 sample as the others have a rather similar value. A possible explanation for the totally different behaviour of the planar sample might be that the structuring of the other samples introduces pinning sides. If the samples reverse by domain nucleation and propagation then the pinning sides tend to frustrate this propagation process, which leads to an increase in H_c.

3.1.4. Magnetostatic Simulations with OOMMF

Description of Model.　To verify the results for the Permalloy nanocone sample series, micromagnetic simulations were performed. Hysteresis loops for a single nanocone were computed for various cone sizes. We utilised the simulation software OOMMF, which is provided by the National Institute of Standard and Technology (NIST).[3] The code for the single cone simulation can be found in the appendix **B**. The documentation for OOMMF's installation, simulation code, and graphical user interface can be found on the OOMMF homepage. The simulation program requires only one input file, where all necessary parameters and the geometric definition of the desired shape are set.

　　Here, a single nanocone, with a thickness of 20 nm Py on the sidewalls, was generated by making use of an OOMMF environmental cube, within which the cone is completely included. This geometrical definition leads to a larger volume of Py on the cone tip compared to the sidewalls, as was shown in the TEM images above for the real samples. To simplify the problem the following assumptions were made: the lateral cone cross-section is an isosceles triangle and the total height is equal to the base diameter. The benefit of defining a surrounding cube is that by changing the surrounding cube size, the size of the cone also changes. The cone structure was described by a function, which defines the lateral boundary of the inner and outer cone surfaces. The simulation grid points included in between these boundaries represent the ferromagnetic material. All points outside this region were set nonmagnetic. The origin (0,0,0) of the coordinate system used by OOMMF is located in the front left bottom corner of the cube. We defined a new coordinate system, which shifts the origin by the transformation

$$\tilde{x} = 2x - 1 \quad \wedge \quad \tilde{y} = 2y - 1 \quad \wedge \quad \tilde{z} = z, \tag{3.1}$$

to the middle of the bottom x-y plane, as shown in Fig. **3.9**. We define the lateral radius

$$r_{\text{dist}} = \sqrt{\tilde{x}^2 + \tilde{y}^2}, \tag{3.2}$$

to exploit the cylindrical symmetry of the cone to be defined. The magnetic volume is then defined as a subset of the cube C and is expressed by

$$
\begin{aligned}
f_{\text{in}}(x,y) &= z_{\text{in}} = h_{\text{in}} - \sqrt{\tilde{x}^2 + \tilde{y}^2}, & (3.3) \\
f_{\text{out}}(x,y) &= z_{\text{out}} = 1 - \sqrt{\tilde{x}^2 + \tilde{y}^2}, & (3.4) \\
\text{where} & \quad \left\{ (\tilde{x}, \tilde{y}, \tilde{z}) \in C \mid h_{\text{in}} - r_{\text{dist}} < \tilde{z} < 1 - r_{\text{dist}} \right\}.
\end{aligned}
$$

---

[3]The National Institute of Standards and Technology (NIST) is an agency of the U.S. Department of Commerce, 100 Bureau Drive, Stop 1070, Gaithersburg, MD 20899-1070, `http://math.nist.gov/oommf/`
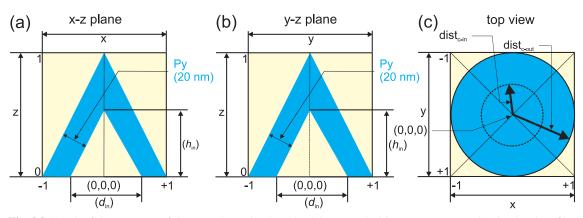
Tab. 3.4.: Table of the slope of the linear fit, the evaluated Gilbert damping α, and the inhomogeneous linebroadening ΔB_0 measured at $\theta_B = 90°$ (ip).

Sample number (N°)	slope of the linear fit (arbitrary units)	α (arbitrary units)	ΔB_0 (mT)
NP0	7.45(2)	0.011	5.15(3)
NP1	6.17(3)	0.009	69.56(8)
NP2	7.98(5)	0.012	45.62(2)
NP3	6.45(4)	0.010	51.94(9)
NP4	11.57(5)	0.017	47.60(2)
NP5	12.80(10)	0.019	62.30(3)
NP6	23.04(5)	0.016	38.50(2)

Fig. 3.9 Sketch of the geometry of the cone shape simulated by OOMMF. The blue areas represent the simulated Py film. The light brown area is the part, which was not evaluated inside the environmental cube. The projection show: (a) x-z plane, (b) y-z plane, and (c) top view.

As (3.1) and (3.3) demonstrate, the inner diameter d_{in} is equal to the inner height h_{in} [see Fig. 3.9(a)-(b)]. Therefore, these parameters will be referred to as the cone size in the following. The simulations presented were done for six different cone sizes: 10, 20, 30, 40, 50, and 60 nm.

Results for the OOP Case. The first simulations were done with the field orientated out-of-plane $\theta_B = 0°$. The results for all cone sizes are shown in Fig. 3.10(a). The field was swept between $H = \pm0.5$ kOe, with 100 steps per branch. After each field step, the magnetisation was relaxed until the stopping criterion was fulfilled [see appendix B]. These results exhibit the expected decrease of coercivity and normalised remanence with an increase of l_{c} .[286–288] The behaviour of $M_{\text{r}}^z/M_{\text{s}}$ (blue squares) and H_{c} (red triangles) is shown in Fig. 3.10(b). This agrees with the results obtained previously from VNA-FMR measurements, where it was inferred that the magnetisation follows the curvature of the nanocone structure. All of the loops simulated depict a switching field above 1 kOe.

Figure 3.10(c) and (d) depict the magnetisation distribution of the in- and out-of-plane magnetisation components at zero field during the reversal, revealing the reason for the broad bending of the curves. During the reversal process, a so-called vortex state appears inside the cones. In the lower part of the cone, the magnetisation gradually turns in-plane, i.e. perpendicular to the z-axis. The in-plane component curls around the cone centre. This state resembles the vortex states observed in ferromagnetic discs [see Fig. 3.10(c) and (d)].[289] In such discs, the exchange energy leads to the formation of an out-of-plane magnetised core in the disc centre. The hollow structure of the cone however allows the vortex state to exist without paying the full price of the increased exchange energy density at the centre. Also the demagnetisation energy associated with the surface charges induced by an out-of-plane core is reduced by the missing centre region inside the cone. This simulation reveals, that a vortex seems to be energetically preferable compared to a switching from one external field orientation to the opposite direction. In the vector plots [see Fig. 3.10(c) and (d)] it can be observed that the vortex state is more dominant in the 60 nm cone compared to the 10 nm cone. The colour coding (red/blue) in the vector plots [see Fig. 3.10(c) and (d)] depicts a tilting of the magnetisation in-plane, because the corresponding directions are the x (side view) and y (top view) coordinates. This also shows, that the magnetisation follows the cone structure.

Results for the IP Case - Overview. Subsequently, the orientation of the applied external field was changed to an in-plane orientation ($\theta_H = 90°$) along the x-axis. The results obtained are shown in Fig. 3.11(a). At a first glance, there are significant differences between the loops of cones with a size less than 40 nm and the
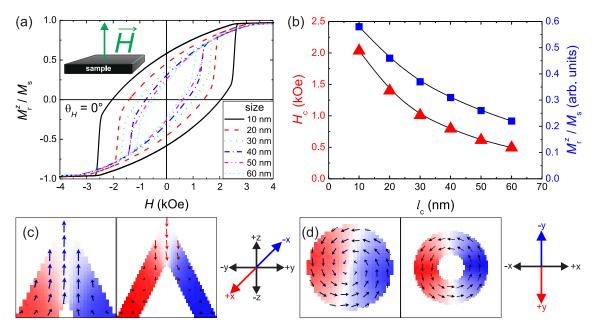
Fig. 3.10 (a) All OOMMF results for the simulations with $\theta_H = 0°$ cone sizes. (b) Analysis results for the coercivity (red triangles/left side) and the z-component of the normalised remanence (blue squares/right side) plotted against l_c. The lines just guides to the eyes. (c) Cross sectional images of the vector field plot in the x-z plane for a 10 nm cone (left) and 60 nm (right). The colour coding according to the x-direction is shown on the right side. (d) Cross sectional images of the vector field plot in the x-y plane at the half height. The left side shows the plot for a 10 nm cone and on the right side the plot for a 60 nm cone is shown. The colour coding according to the y-direction is shown on the right side. Both cross-sections show the magnetic configuration at $H = 0.00$ kOe.

larger ones. In addition there are obvious differences from the results for the out-of-plane field simulations. The simulated loops for cones between 10 and 30 nm in size reveal a reversal from one direction to the other one with no bending observable as compared to the results for $\theta_B = 90°$. However, the loops for the cones which are 40 to 60 nm in size show, at a certain field during the reversal process, a similar bending to that seen in Fig. 3.10(a). These results show a two parts reversal process. The first part is a sharp reduction of magnetisation to zero. Then the magnetisation gradually increases in the opposite direction. This is typical for a switching of a vortex state. The first part is where the vortex forms and the second part is the movement of the vortex core through the structure. Besides, the loops behave differently to the latter simulation geometry, which shows up due to the normalised remanence, as well as, the coercivity. Both parameters do not show a decrease with increasing cone size, as was expected.

The 20 and the 60 nm results depict an unusual behaviour. These simulations do not show the switching behaviour expected, namely that $\vec{M}$ follows the surface profile of the nanocones. This behaviour would be expected to result in a decrease of both the normalised remanence and the coercivity with increasing cone size. One possible reason for this discrepancy between the simulated and the measured behaviour could be related to the fact that the simulation is of an individual cone, whereas the real samples consist of a large number of cones which can interact, taking into account these interaction would probably improve the simulations. In order to achieve a better understanding of the single-cone hysteresis loops, a second simulation was started within a smaller field range ($H = -0.30$ up to $+0.70$ kOe / ascending branch) and an increased number of steps of 500 steps per branch. The resulting hysteresis branches are shown in Fig. 3.11(b). As shown before, the cones up to 30 nm in size show a single jump from one orientation to the opposite. The switching field of the cones up to 30 nm in size is rather small compared to the cones larger than 30 nm in size. Whereas, all larger cone sizes undergo a transition during the reversal from common reversal loop behaviour to a bent hysteresis loop. Due to the observation of the bending of the hysteresis loop
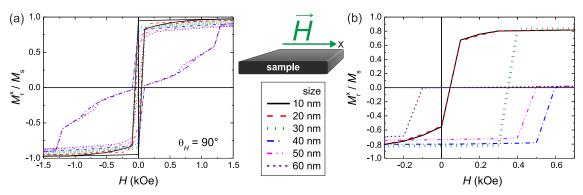
Fig. 3.11 (a) All hysteresis loops simulated for the in-plane geometry. (b) Simulation results for the in-plane configuration with a smaller field range, but with more steps.

it is expected that a vortex state is involved in the transition process as was shown for the oop configuration prepared simulations, which was already shown. First the shift of the coercivity will be discussed. As shown in Fig. 3.11(b), the 10 and 20 nm results depict a similar behaviour, where the 30 nm and 40 nm loops show an increase of H_c. The samples with even larger cones then behave in an unexpected manner, their H_c is observed to decrease instead of continuing to increase. In particular, the H_c of the 60 nm loop which has a negative value is unexpected and might be caused by an computation error in the simulation. In order to understand the behaviour observed one has to consider the particular contributions to the total energy of the system:

$$E_{tot} = E_{dem} + E_{exc} + E_{Zeeman}, \tag{3.5}$$

which are the dipole energy, the exchange energy, and the Zeeman energy, respectively. We developed an idea to explain the observed behaviour, which is based on qualitative energy considerations. A further detailed quantitative analysis should lead to a confirmation of the following idea:

- For cones with sizes ≤ 30 nm, the magnetisation at low external fields is characterised by a homogeneous in-plane component, while the out-of-plane component is largely positive in one half of the cone and negative in the other half [see Fig. 3.13(b)], forming a domain-wall-like structure in between. We will refer to this as the quasi-homogeneous (QH) configuration. As the sample approaches the saturated state, the in-plane component increases at the expense of the out-of-plane component.

- Fig. 3.11(b) shows that the reversal in the trend of H_c versus size is accompanied by a qualitative change of the hysteresis loop. For samples with sizes ≥ 40 nm the magnetisation reverses via the formation of a vortex-like state.

- Fig. 3.13(c) shows the vortex-like state. This configuration has a curling of the in-plane magnetisation, while the out-of-plane component is generally small. It increases near the cone tip until it points entirely up- or downwards. This can be seen as an analogy to the conventional vortex structures in nano-sized ferromagnetic discs. Here, the out-of-plane magnetisation at the disk centre, referred to as the vortex core, can have "up" or "down" polarity. [290]

  From the simulations, one observes that small sizes ≤ 30 nm favour the quasi-homogeneous (QH) configuration described above. We now compare the vortex like and QH states at a fixed intermediate field, near the switching field.

- The QH state generates a stray field. However, due to the presence of the domain-wall, there is also a contribution to the exchange energy. As the cone size increases, both energy contributions increase, as

well.

- The vortex-like state:

  From the simulated magnetisation distributions it is plausible, that while the cone end contains an amount of exchange energy, the contribution from the rest of the structure to E_{exc} might be rather low. Due to the curling magnetisation in the lower part of the cone, it is expected, that the energy density of the demagnetising field has its maximum in the cone end, as well.

- From the above, it is expected, that E_{tot} of the QH to increase faster with increasing cone size than E_{tot} of the vortex-like state.

- This leads to an interception of both energy curves as a function of the cone size parameter. Small cones will prefer the QH state, while for larger cones beyond the point of intersection, the vortex state is energetically preferable.

Now the influence of the external magnetic field has to be considered.

- Figure 3.12 shows the schematic drawing of $\Delta E = E_{\mathrm{QH}} - E_{\mathrm{vls}}$ versus size. The definition of a positive field is that the magnetisation points in the opposite direction with respect to the magnetisation before the sample switches into the vortex-like state. Since the magnetic moments of the vortex-like state partially compensate the dominant contribution to ΔE is expected to increase mainly due to the changes in E_{QH}. From the same argument, cones of the same size will have a lower ΔE for lower H_{ext}. The slope of ΔE with H_{ext} is expected to increase with increasing cone size. This leads to the different slopes of ΔE with size as can be seen in Fig. 3.12.

- Then, according to Fig. 3.12 for larger cones the switching from the QH state into the vortex-like state takes place at an earlier point during the hysteresis.

- This idea would explain the decreasing switching field with increasing cone size seen for cones larger than ≥ 40 nm. From our considerations, the decrease of the switching field with increasing cone size is expected to slow down, whereas the in the simulation it accelerates. Thus, a quantitative check of this explanation by micromagnetic simulations should be performed.

Results for the IP Case - Comparison of: $\leq$ 30 nm / $\geq$ 40 nm.   Figure 3.13 shows the detailed analysis of the differences between the simulation results for the 30 and 40 nm cone sizes. The information obtained from analysing these two results is then valid for either the smaller cone sizes by referring to the results for the 30 nm cone, or for the larger ones when referring to the results of the 40 nm cone. These two cone sizes were chosen as being exemplary of the overall system behaviour, because it is between these sizes that the system behaviour changes. In the top right corner the simulated loops are shown for both sizes. Here, the reversal behaviour typical of a smaller cone is reproduced, whereas the loop for the larger cone reveals a bending [see Fig 3.13(a)] behaviour in the hysteresis during the switching process for values higher then $M_{\mathrm{r}}^z/M_{\mathrm{s}} \cong 0$. To show that this bending corresponds to a vortex state, the vector field plots (VFP) of the magnetic configuration are shown. Below the overview graphic [see Fig 3.13(a)], the colour coding for the vector field plots is shown, as well as the magnetic field orientation with respect to the sample. The top panels of Fig 3.13(b) and (c) depict the switching region of the simulated hysteresis loop. Below the loops, two VFPs showing the configuration at two different fields are shown. The VFP before the switching is shown on the right and on the left the result after the switching is shown. All VFPs presented first depict the cross-section in a side view, whereas the top view is always shown below.

Figure 3.13(b) represents the results for the 30 nm cone size. The loop depicts a switching from one
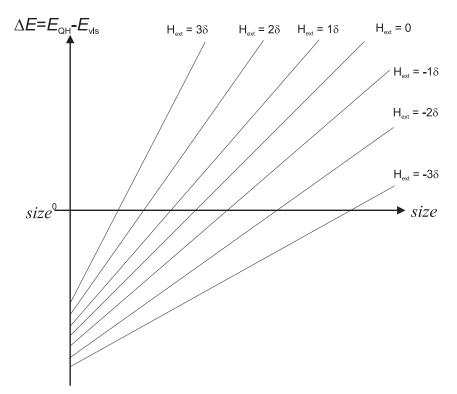
$$\Delta E = E_{\mathrm{QH}} - E_{\mathrm{vls}}$$

Fig. 3.12 Schematic drawing of the energy difference ΔE between the QH-state E_{QH} and vortex-like state E_{vls} as a function of the size for different values of the external field ($\delta > 0$), assuming rigid magnetisation distribution. The origin size^0 represents the finite size, where the vortex-like state is always preferable.

direction to the opposite. Below the graph of the hysteresis loop the magnetic configuration on either side of the transition is shown in cross-sections. The side- and the top views indicate that the reversal takes place between a field of 0.03 kOe and 0.04 kOe. The change of the direction of the magnetisation is clearly observable. Moreover, the side views show that the magnetisation partly follows the curvature of the cone. In order to avoid creating surface charges, the magnetisation points on one side up to the cone tip and on the other side down to the cone base. This magnetisation configuration was also observed in the simulations where the field was applied perpendicular to the sample surface. The results show the same quantitative behaviour for all cone sizes below 30 nm.

The cones with a size equal to or greater than 40 nm behave differently during the magnetisation reversal. This is shown in the panel of Fig. 3.13(c). The VFPs indicates, that before the switching process begins ($H = 0.05$ kOe) the conditions are similar to those in the 30 nm case. The difference here is that the region where the magnetisation points to the cone base is larger compared to the VFP results for the 30 nm cone size. Since only the in-plane component of the magnetisation contributes to the Zeeman energy, the position of the domain wall (i.e. "on the left" or "on the right" side) should be arbitrary. Both positions are equivalent in terms of energy. At a certain critical field the $M_{\mathrm{r}}^z / M_{\mathrm{s}}$ jumps to zero. Subsequently, the bending in the hysteresis loop is observable. At $H = 0.06$ kOe the vortex state is observable in both VFPs. Moreover, the upper VFP shows that at the cone tip the magnetisation predominantly points towards the cone base. The behaviour on the sidewalls is different. There, the magnetisation is obviously tilted more and more into the x-y plane as the vertical distance from the cone tip increases. The vortex state remains stable up to a certain field value, at which point it is expelled from the structure and the magnetisation becomes homogeneous again. Still the open question has to be answered: "Why do the coercivity and remanence not decrease with increasing cone size?". This is particularly puzzling due to the fact, that in the VFP a
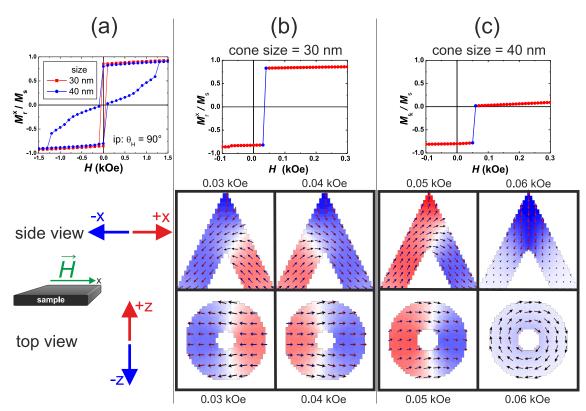
Fig. 3.13 (a) Simulation results plotted for the 30 and the 40 nm cone size. Below this graph the colour coding for the vector field plots on the right and the field orientation is shown. Below (b) and (c) the corresponding results are shown with the following the order, beginning from top, is: loop, side view cross-section, and top view cross-section. (b) Simulation results for the 30 nm cone size. (c) Simulation results for the 40 nm cone size.

tendency of the magnetisation in the nanocone to follow the nanocone curvature is apparent [see Fig. 3.13(b) and (c)]. Furthermore, the results in Fig. 3.10(b) exactly reveal this expected behaviour. Whereas, the loops in Fig. 3.13(b) and (c) do not show the expected tendencies for the coercivity and the remanence. A possible explanation might be given by the stray fields in between the cones. Nevertheless, a clear explanation has to be found. For that purpose, further simulations of a system of multiple cones need to be performed.

3.1.5. Summary

In this section we characteristics a thin film of Cr (5 nm)/Py (20 nm)/Cr (3 nm) on top of a GaSb(001) substrate pre-structured with nanocones. For this work nanocones with six different l_c's were prepared, a linear relationship between the l_c and the irradiation energy was determined by PCF analysis. The samples prepared had a reasonably high degree of order. Nevertheless, a still higher ordering has to be achieved if these samples are to be used in a technological application, such as bit patterned media for example. Moreover, it was shown that the GaSb wafer is covered by small GaSb fragments, which also had a periodic distribution on the surface. This contamination needs to be prevented, because it modifies the results for the planar sample making the comparison with a nanostructured sample more difficult.

Furthermore, the results of coating the patterned substrate with a Cr (5 nm)/Py (20 nm)/Cr (3 nm) film were presented. In the TEM image one observes that a polycrystalline film has formed on top of the nanocones, the crystallographic structure originates from the amorphous GaSb cap film. This cap film forms due to the action of the ion beam erosion process.

Subsequently, the results for the VNA-FMR measurements were shown. The polar measurements reveal,

as expected, an in-plane magnetisation for the planar sample. Moreover, a decreasing resonance field at $\theta_B = 0°$ and an increasing B_{res} at $\theta_B = 90°$ with an increasing l_c were found. This indicates that the magnetisation follows the curvature of the nanocones. The fitted $4\pi M_{\mathrm{eff}}$ parameter provides further evidence in support of this idea as a decreasing effective magnetisation with an increasing l_c was observed. The analysis of the linewidth information gives information about the damping and the inhomogeneous linebroadening. The linear slope of the frequency-dependent VNA-FMR measurements indicates that only a Gilbert damping is present in this system. Furthermore, the Gilbert damping parameters α measured for the different l_c, reveal that in the case of the in-plane geometry the α is increasing for cones with $l_c \geq 40$ nm. However the damping measured using the out-of-plane geometry stays nearly constant. By analysing the inhomogeneous linebroadening one observes a significant difference between the measurements at $\theta_B = 0°$ and $\theta_B = 90°$. The results for $\theta_B = 0°$ show a slight increase with increasing l_c and the values are of the order of several tens of Oe. Whereas the values obtained for $\theta_B = 90°$ reveal significantly higher values which are of the order of several hundred of Oe, and have a significant spread of about 200 Oe. Both results obtained for α and ΔB_0 indicate, that the simplified resonance condition formula typically used (homogeneous infinite film) cannot be valid anymore. This is indicated by Fig. 3.7 which shows an increase of α for the cones > 30 nm and the large difference between $\Delta B0$ in the oop and ip geometry. In the case where the transition from an infinite uniformly flat film to the 3D magnetic structure has to be taken into account, one is dealing with effective values α_{eff} and $\Delta B_{0,\mathrm{eff}}$. These results suggest, that a new equation has to be derived, which accounts for these morphology aspects. The in-plane MOKE scans are able to detect whether one has to consider an in-plane anisotropy contribution. As was shown, only in the case of the planar sample was a slight fourfold anisotropy observable, which may possibly originate from the GaSb(001) substrate. In contrast, all of the pre-structured samples show an isotropic behaviour. Due to the presence of the amorphous cap film on the GaSb nanocones the Cr (5 nm)/Py (20 nm)/Cr (3 nm) stack grows in a polycrystalline manner, which might be the reason for that isotropic behaviour. The results for H_c show a decrease in value for all of the pre-structured samples, which corroborates the picture that the magnetisation follows the curvature of the cones. A slightly different result was obtained by the analysis of the M_r. Here the NP1 and the NP2 behave in an opposite manner to that implied by the measurement of H_c. Excepting these two samples, the others show a decreasing normalised remanence with increasing l_c. This is also consistent with the explanation proposed. It is possible that one of these samples had been damaged, which would be an explanation for this result. Afterwards, an OOMMF simulation was performed to help better understand the information obtained from the measurements. A series of simulations with cone sizes between 10 and 60 nm in steps of 10 nm were performed with an in-plane and an out-of-plane applied external field. The oop simulations show the expected decrease of H_c and M_r/M_s with increasing cone size. However, the results of the ip simulations do not exhibit the behaviour expected. Nevertheless, a partial explanation for this behaviour was given. Further micromagnetic simulations might improve the understanding of this system.

3.2. CoCrPt and CoCrPt:SiO$_2$

Granular CoCrPt:SiO$_2$ is a well-known recording media. For the last two decades it has been the focus of many investigations.[291] First CoCrPt:SiO$_2$ was used in longitudinal hard disk drives. Afterwards the CoCrPt:SiO$_2$ film and a soft magnetic underlayer together with a dual-Ru seed layer have been developed to allow its use as a high perpendicular anisotropic media which find uses as in PMR.[292] This development allows hard disk drive producers to increase the storage density significantly.[293] It was possible to reduce the grain size as well as to reduce the inter-granular exchange coupling by using an oxide addition to the growth process.[294] These approaches have led to the currently common numbers of 20 to 30 grains per bit, with an average diameter per grain of 6 to 8 nm.[295] Currently, the development of hard disks has reached a storage density of about 1 Tbit/inch^2.[40,293] Further steps to improve this could be heat assisted-, microwave-, domain-wall assisted magnetic recording and/or bit patterned media.[41,44,138,296–298]

In this chapter the investigations of the recording media CoCrPt:SiO$_2$ will be presented. CoCrPt:SiO$_2$ has the advantages of a high perpendicular anisotropy and coercivity. The anisotropy axes are highly oriented out-of-plane due to the tailoring of the entire stack. Details of the tailoring process are described elsewhere.[7,8,10,16,299–306] These points are important for its application as a perpendicular recording media (PMR). The investigations presented here focus on the influence of ion implantation and morphology-induced effects on the magnetic properties of the samples. Moreover, the influence of an additional oxide in the CoCrPt grains will be discussed. First the investigations of the nanostructured samples will be presented, wherein two test systems were studied. The first subsection deals with two planar CoCrPt test samples, where besides the static magnetic properties, also dynamic measurements will be discussed. Apart from studying the saturation magnetisation, the remanence, coercivity, anisotropy, damping, and inhomogeneous linebroadening of this experimental CoCrPt system, a comparison between VNA-FMR and TRMOKE results will also be presented. The second subsection describes the study of a planar CoCrPt:SiO$_2$ sample series, which was implanted with Co$^+$ ions, where the fluence of the ions was varied over a large range. The idea behind this variation was to study the intermixing and concentration effects of the implanted Co on the magnetic properties of the CoCrPt:SiO$_2$ stack. Within the second subsection, practical aspects concerning VNA-FMR measurements of the CoCrPt:SiO$_2$, as well as the [Co/Pd] samples will be discussed. In addition, the differences between those samples which consist of only CoCrPt and those with additional SiO$_2$ content will be described. In the last subsection, the results of the investigations of CoCrPt:SiO$_2$ on GaSb(001) nanocones will be presented. Here, the focus is on the effects of the tailored exchange interactions between the grains and also between the nanocones. The interaction between the grains is from now on called the intergranular exchange interaction and the interaction between the nanocones will be called the interdot exchange interaction. With regards to the intergranular- and interdot interactions, the influences of SiO$_2$ content and the growth of the grains with respect to the size and shape of the nanocones will be discussed.

3.2.1. Hard- and Soft Magnetic Planar Granular CoCrPt Films

We will start in this section with a discussion of the results obtained from measurements on a planar CoCrPt sample series and subsequently a planar CoCrPt:SiO$_2$ specimen. The results for both sample series will be used as a reference system in the summary [see chapter 4], for comparison with the results from the granular CoCrPt:SiO$_2$ on nanocones. Furthermore, the purpose of these measurements was to get to know the capabilities of this recording material, mainly in terms of the dynamical magnetic properties as measured by
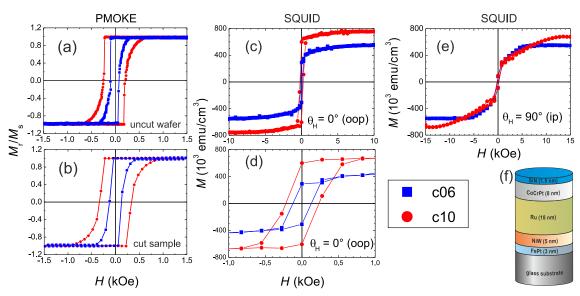
Fig. 3.14 (a) – (e) Magnetometry measurements of the hard magnetic sample c10 (red points) and the soft magnetic sample c06 (blue squares). (a) PMOKE measurements, carried out before cutting into small pieces, and (b) after the cutting. (c) SQUID at $\theta_H = 0°$. (d) Magnification of measurement (c). (e) SQUID at $\theta_H = 90°$. The lines are just guides to the eyes. (f) Sketch of the CoCrPt stack.

the VNA-FMR- and the TRMOKE setup. These results are presented within this subsection. Secondly, the CoCrPt:SiO$_2$ samples were used to investigate the influence of ion implantation on its magnetic properties, the results of which are presented in the second subsection. The experimental systems presented first are two oxide-free CoCrPt samples. One of them is a hard magnetic sample (c10) and the other one is a soft magnetic sample (c06). The reason for this classification originates from the two different anisotropies of these samples. The anisotropies were induced by the alloying of Cr and Pt during the growth. The soft magnetic sample (c06) has a higher content of Cr and less Pt compared to the hard magnetic sample (c10). Due to the granular hcp structure of CoCrPt , the resonance condition for the analysis of the VNA-FMR and TRMOKE measurements has to be derived from the Gibbs free energy with respect to the hcp structure.[10,13,307–315] This derivation is shown in the appendix A. The first sample series was prepared without a SiO$_2$ add-on and therefore these samples are strongly exchanged coupled. This strong exchange coupling is beneficial, because this should increase the signal of the VNA-FMR measurements as it enforces the coherent precession of all grains in phase.

The two samples c06 and c10 were prepared by the group of Dr. Olav Hellwig at the research centre of Hitachi Global Storage Technologies, a Western Digital company. Due to the fact that these samples were prepared in an industrial research and development department, it has to be mentioned, that not all of the preparation processes or the exact alloy compositions could be described in detail. Fig. 3.14(a) shows the entire stack that was created. This stack was deposited using magnetron sputtering onto both sides of a glass wafer. The first layer is 3 nm of FePt-alloy, which has two main functions. On the one hand

Tab. 3.5.: Table of the PMOKE and SQUID analysis for the soft (c06) and hard magnetic (c10) samples.

Sample number N°	H_c (uncut) kOe	H_c (cut) kOe	M_s 10^3 emu/cm^3
c10	0.230(8)	0.336(2)	720(40)
c06	0.097(5)	0.131(9)	550(10)

it allows the proper adhesion of the metallic layers to the glass wafer, and on the other hand it is also a SUL. Usually the SUL in a recording media is about 40 nm thick, but in this case for the purposes of the experimental investigation done in this work, this layer was chosen to be as thin as possible in order to lower the magnetic anisotropy. This decreased the excitation power required and therefore made the sample suitable for measurements with the VNA-FMR and TRMOKE. The next layers are a NiW layer of 5 nm and a Ru layer of 18 nm thickness. Both layers are crucial for the proper epitaxial growth of the CoCrPt:SiO$_2$ on top, which causes a perpendicular anisotropy with a high degree of orientation along the film normal (see chapter 1). Afterwards the magnetic CoCrPt layer with a thickness of 8 nm was deposited and then finally a SiN cap layer with a thickness of 1.5 nm was added to prevent oxidation. The entire stack then reads from the bottom to the top on each side as: glass wafer/FePt-alloy(3 nm)/NiW(5 nm)/Ru(18 nm)/CoCrPt(8 nm)/SiN(1.5 nm).

PMOKE and SQUID The samples were sent as two large pieces, which made it necessary to cut both into smaller pieces of 4×4 mm^2 for the further experiments. For the original large samples, polar MOKE measurements were carried out by Dr. Olav Hellwig [see Fig. 3.14(b)]. Afterwards the samples were cut into pieces by a diamond saw and a second set of polar MOKE measurements were done, these should ensure that the division of the sample into smaller pieces has not changed the magnetic properties. This measurement is shown in Fig. 3.14(c). The data for the sample c10 is shown by red squares and for the sample c06 by blue circles. The comparison of both PMOKE measurements show that each sample exhibits a clear out-of-plane magnetisation, as was expected. All the H_c values determined from the PMOKE measurements are similar to literature values [see Tab. 3.5].[34,232] There is, however, a slight difference in the measurements of the samples before and after cutting: the samples show a lower coercivity before cutting. One reason for this behaviour could be the existence of so-called magnetic soft spots, which are imperfections inside the film which can pin the domains during the switching process.[316,317] These imperfections are present in the cut and uncut sample, however within the cut sample measured there might be an increased density of such soft spots. Another possibility is that the sample might be heated during the cutting process, and this might lead to an annealing process.

Due to the fact that the LMOKE setup is limited to a maximum external field of 790 Oe, which is insufficient to saturate the CoCrPt samples, two SQUID measurements were carried out. One is measured along the out-of-plane easy-axis and the other one along the in-plane hard-axis of magnetisation, to obtain information about the saturation magnetisation. These measurements are shown in Fig. 3.14(c), (d), and (e) and furthermore, the values determined are listed in Tab. 3.5. The colour coding is the same as that used in the PMOKE graphs. Figure 3.14(d) shows the measurement along the easy axis $\theta_B = 0°$ and the Fig. 3.14(e) the measurement along the hard axis ($\theta_B = 0°$). The comparison of the PMOKE and the SQUID data in Fig. 3.14(b) and (c) show significantly different shapes for the easy axis loops, in principle both methods should yield the same measurement result. In particular, the values for the normalised remanence deviate between these two methods. This can be explained by a misalignment of the samples in the SQUID

Tab. 3.6.: Table showing the results of fitting for the anisotropy fields $2K_i/M_s$ and g-factor (resonance condition fit) for the soft- (c06) and hard magnetic (c10) samples. The last row shows the values determined for the soft magnetic underlayer (SUL).

Sample number N°	$4\pi M_{\mathrm{eff}}$ kG	$2K_{4\perp}/M_s$ Oe	$2K_{6\perp}/M_s$ Oe	g-factor arb. units	φ_u °
c06 (CoCrPt)	5.2	130	20	2.15(3)	14
c10 (CoCrPt)	11.3	106	72	2,11(5)	0
c10 (SUL: FePt)	6.7	-20	82	2.11(5)	0

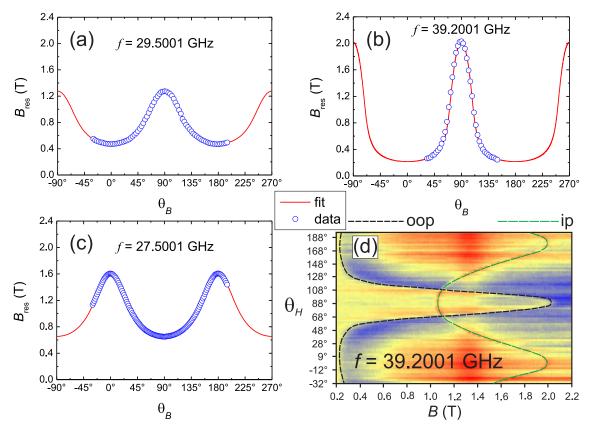**Fig. 3.15** Polar angle-dependent VNA-FMR measurements in the range $\theta_B = -30°$ to $+195°$. (a) Fit of the soft magnetic planar granular CoCrPt (c06). (b) Fit of the hard magnetic planar granular CoCrPt (c10). (c) Fitted FMR signal of the SUL (FePt-alloy) of the hard magnetic sample. (d) Pseudo colour plot of the hard magnetic sample. The dashed lines emphasise both observable resonances in the hard magnetic specimen.

measurement. A practical difficulty associated with using the SQUID is that it is not possible to align the sample perfectly within the sample holder tube along the easy or hard axis of magnetisation. Usually, this deviation is around $\pm 5 - 10°$. The measurements in Fig. 3.14(d) suggest that the angular deviation lies in this said range. Nevertheless, by comparing the shapes of both of the SQUID loops shown in Fig. 3.14(c) and (e) an out-of-plane magnetisation for both samples is observable, as expected The M_s values obtained from these measurements are summarised in Tab. 3.5. To normalise the magnetisation with respect to the magnetic volume, it was assumed that the FePt-alloy and the CoCrPt on both sides contribute to the magnetic moment. Therefore, the entire volume of magnetic material was determined to be $V_{FM} = 3.52 \times 10^{-7}$ cm^3. As will be shown within next section, which presents the analysed FMR results, the FM FePt-alloy layer is also visible in the FMR measurement of the c10 sample. The data obtained reveal similar values for M_s to those found in the literature for CoCrPt .[306,318] Typically, the values for M_s are less than 1000 emu/cm^3 for CoCrPt .[319,320] Due to the fact that the exact composition of the FePt-alloy used here is not known, an assignment of the signal to one or the other FM layer is not possible. Moreover, even for the CoCrPt , the dependence of M_s on the FePt-alloy SUL composition used and the variation of M_s with the content of Cr and Pt, does not allow a more detailed clarification of the contribution from each of the FM layers to the measured signal.

VNA-FMR Measurements   The first set of measurements carried out with the VNA-FMR on these samples used a polar geometry, where the angle of the applied external field was varied. These measurements (blue
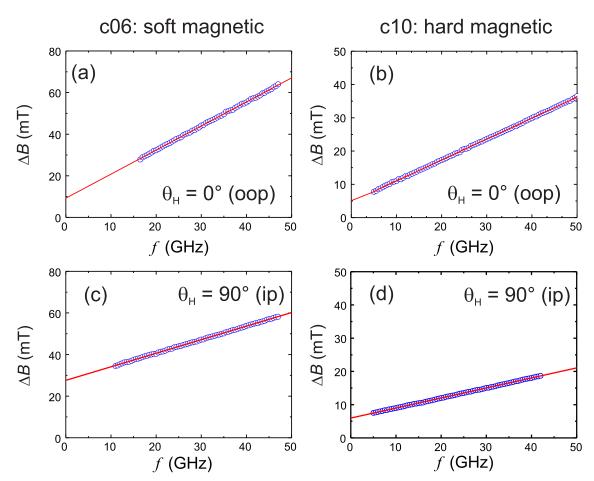
Fig. 3.16 Frequency dependent VNA-FMR measurements (blue circles) with linear fit (red lines) (a,c) c06: soft magnetic CoCrPt . (b,d) c10: hard magnetic CoCrPt .

circles) along with the fit curves (red lines) are shown in Figs. 3.15(a) – (c). The Figs. 3.15(a) and (b) reveal the expected out-of-plane magnetisation, as indicated by the maximum resonance field being at $\theta_B = 90°$. The frequency of the measurement for the c06 sample was $f = 29.5001$ GHz and for the c10 sample $f = 39.2001$ GHz. The higher frequency was chosen, because the first measurement at $f = 27.5001$ GHz of the c10 sample achieved the result shown in Fig. 3.15(c). There, the angle dependence for the c10 sample obviously behaves differently to the measurements shown in Figs. 3.15(a) and (b). The result of measuring c10 at the lower frequency reveals the presence of an in-plane magnetisation, because both of the observable maxima are located at $\theta_B = 0°$ and the minima at $\theta_B = 90°$. This in-plane magnetisation could be assigned to the FePt-alloy SUL layer. Still, the absence of any contribution from the SUL (additional resonance peaks at $\theta_B = 0°$ and $\theta_B = 180°$) to the measurement of the c06 sample is puzzling and the reason could not be determined up to now. Interestingly, both types (in- and out-of-plane easy axis) were visible in the measurement of the c10 sample at $f = 39.2001$ GHz, which is shown in the pseudo-colour plot in Fig. 3.15(d). There, both curves are emphasised by dashed lines (ip: green dashed line/oop: black dashed line). The fit parameters for the anisotropies are summarised in Tab. 3.6. The value of $4\pi M_{eff}$ for the c10 sample is slightly smaller as compared to the value published by Clinton *et al.* of $4\pi M_{eff} = 14.124$ kG. [321]

To obtain information about the *g*-factor and the damping, two further frequency dependent measurements were carried out. One was done at $\theta_B = 90°$ and the other one at $\theta_B = 0°$. The results of the measurements (blue circles) and the linear fits (red lines) are shown in Fig. 3.16(a) – (d). Figures 3.16(a) and (b) represent the results for $\theta_B = 0°$ and Figs. 3.16(c) and (d) the ones for $\theta_B = 90°$. From the out-of-plane measurements

the g-factor was determined. For the c10 sample it is $g = 2.11$ and for the c06 sample $g = 2.15$, which is, in the order of magnitude consistent with the literature.[106] The difference between both Landé factors for c06 and c10 might be due to the differences in the in the alloy content (g-factor is sensitive to the local electronic environment of the atoms). The $g$factor values determined were used to fit the polar VNA-FMR results in Figs. 3.15(a) – (c). The analysis of the slopes for the data in Fig. 3.16(a) – (d) reveal that in each system shown only Gilbert damping is observable. This is indicated by the linear relationship between linewidth and frequency. The results of the linear fits are listed in Tab. 3.7. As shown in Tab. 3.7, the Gilbert damping parameter for the c06 sample is nearly twice as much compared to the c10 sample. Comparing α for the two different geometries shows, that for the in the plane geometry the α is nearly twice as large as in the out-of-plane geometry. All the damping constants determined are similar to the literature, where α ranges between 0.001 and 0.03.[322–324] The analysis of the inhomogeneous linebroadening ΔB_0 reveals a different behaviour. While the ΔB_0 ratio between the results of the oop geometry for c06 and the c10 sample is approximately two, the ratio between both samples in the ip geometry is around five. By comparing the evaluated ΔB_0 for both the geometries and for each sample, one can observe the following: for the c06 sample between oop and ip the ΔB_0 ratio is 2.5, whereas for the c10 sample it is approximately one. The origin for this might be found in misplacements of the granular structure.

TRMOKE Measurements were carried out on the one hand to obtain further measurements of the magnetic properties of the CoCrPt system and on the other hand to compare these data with the results achieved by the VNA-FMR setup. The measurements were done at a polar angle of $\theta_B = 60°$. This angle is chosen to apply the external field between the ip and the oop geometry, which is necessary so that the system is able to generate an internal field transient when the laser pump pulse creates a short thermal transient. Furthermore, the choice of this angle was limited due to the requirement to reflect the laser beam off the sample which was placed in between the poles of an electromagnet. The external field was swept to record the change of frequency versus field. This was achieved by fitting the individual signal curves for every individual field step, and determining the corresponding resonance frequency as a function of the field.

The data for both samples, given as the inverse of the decay time and the frequency, is shown in Figs. 3.17(a) – (d). Figures 3.17(a) and (b) present the data (red circles) and the fit curves (black lines), fitting is done by using the hcp resonance condition. The fit parameters obtained are summarised in Tab. 3.8. The comparison between the TRMOKE and VNA-FMR fit parameters shows that the results for the c06 samples have the same $4\pi M_{\text{eff}}$ and also the other anisotropy fields are similar. So the results for the c06 sample from the VNA-FMR and the TRMOKE can be considered as being consistent. In contrast to the c06 fit, the TRMOKE result for the c10 sample does not match to CoCrPt , but to the FePt-alloy in the adhesion layer. One can be sure that the probe beam cannot sense the bottom layer, because the penetration depth of 400 nm light into typical metals is about ten nanometres. The reason for this discrepancy remains unclear. There are two possible reasons for this which are related to the elevated temperature of the sample during measurement. The first issue is due to the fact that K_u and M_s are a function of the material temperature and therefore both

Tab. 3.7.: Table of the results for Gilbert damping α and inhomogeneous linebroadening ΔB_0 for the soft- (c06) and hard magnetic (c10) samples.

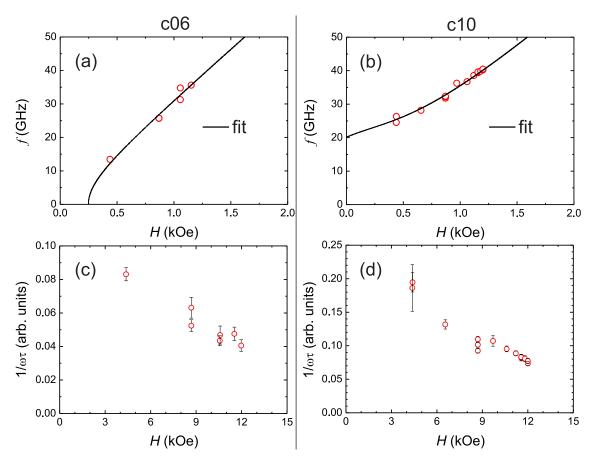| Sample number N°	α ($\theta_B = 0°$) arb. units	ΔB_0 ($\theta_B = 0°$) mT	α ($\theta_B = 90°$) arb. units	ΔB_0 ($\theta_B = 90°$) mT
c06	0.017(2)	9.22(5)	0.010(2)	27.59(4)
c10	0.009(2)	4.74(3)	0.005(2)	5.97(2)

Fig. 3.17 Results for the TRMOKE measurements of soft- (left panel) and hard magnetic (right panel) CoCrPt. (a) – (b) Evaluated resonances measured at $\theta_H = 60°$ with fit curves (black lines). (c) – (d) determined damping constants.

change due to the laser heating. The second issue is that the thermal treatment can cause an annealing effect on the material, which changes the properties as well. However one might expect to see this effect in both cases (for c10 and for c06) because the samples are similar regarding the thermal properties.

The data for τ and ω are plotted as $(\omega\tau)^{-1}$ versus external field as shown in Figs. 3.17(c) and (d). The value $(\omega\tau)^{-1}$ represents the damping α, under certain conditions mentioned in the TRMOKE section, and in these measurements a decrease in the damping parameter with an increasing field is observed. This decrease indicates that the damping measured is not the underlying intrinsic damping of the material. Generally speaking, the material's intrinsic damping is not expected to change with field. As will be shown in the next subsection, in case of a certain field and frequency the damping saturates and stays constant with increasing field values. Once the applied field has been raised to a level where the measured value of the damping stops changing, then the data above this level can be averaged to obtain the damping parameter. In the case where $(\omega\tau)^{-1}$ is seen to continuously change over the measured range then no damping constant can be determined. However, the lowest value obtained can be used as an upper limit for the real damping. This is because, although one can always measure something larger than the real damping due to problems such as linebroadening effects etc., a lower damping than the intrinsic one should never be obtained. Therefore, in the case of c06 α must be less than 0.04 and in the case of c10 less than 0.1.

Summary It was shown in this subsection how the magnetic properties of a CoCrPt sample are sensitive to the alloying elements used in its preparation. The SQUID and PMOKE measurements reveal that the CoCrPt samples have a high perpendicular anisotropy as expected. The M_s data obtained from the SQUID

and the H_c data from PMOKE are similar with those in the literature. Furthermore, the polar VNA-FMR measurement also shows the perpendicular anisotropy. The hard magnetic c10 sample showed the resonance curve for the FePt-alloy layer at a lower frequency, as well as showing the resonances of both layers at a higher frequency. The soft magnetic sample only shows a resonance curve with oop anisotropy corresponding to the harder magnetic layer only. The anisotropy fields evaluated from the VNA-FMR data are similar as those given in the literature. Furthermore, the $4\pi M_{\text{eff}}$ of the c10 sample is closely equivalent to the value given in the literature. Also the analysis of the linewidth measured by the frequency dependent VNA-FMR experiments yields values from the fit parameters for the damping and the linewidth which are consistent with values in the literature. The last measurements on these samples were carried out using the TRMOKE setup. The parameters of the c06 sample are approximately equal for TRMOKE and VNA-FMR. Although the values obtained for c10 seem to match those for the SUL rather than the top magnetic layer which was measured by the probe beam, this may be coincidence. Further measurements are necessary to resolve this issue. For example, one can vary the pump power to see if the values measured change, this would indicate that the temperature of the sample during the measurement changes the material properties. The last part of the analysis deals with the damping. Here it was shown that $(\omega\tau)^{-1}$ is decreasing with increasing applied field. This means that an evaluation of the damping behaviour is not possible over the limited field range used, due to the fact that such a decrease of the damping shows that the measurement is still in an unsaturated resonance condition.

Tab. 3.8.: Table of the fit results of the TRMOKE measurements damping of the soft- (c06) and hard magnetic (c10) samples.

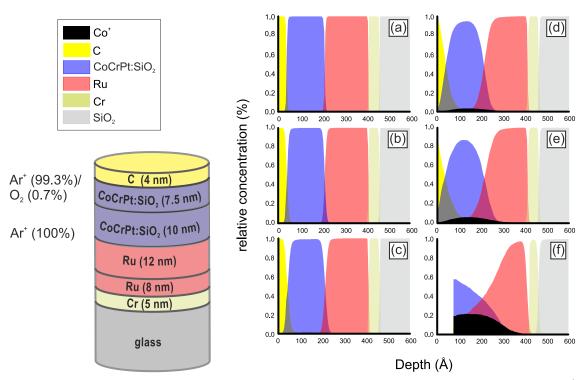| Sample number N°	$4\pi M_{\text{eff}}$ kG	$2K_{2\parallel}/M_{\text{s}}$ Oe	$2K_{4\perp}/M_{\text{s}}$ Oe	$2K_{6\parallel}/M_{\text{s}}$ Oe	$2K_{6\perp}/M_{\text{s}}$ Oe	g-factor arb. units
c06	5.2	0	-1.2	0	164	2.15
c10	6.7	144	40	0.2	6	2.11

Fig. 3.18 Left: Sketch of the CoCrPt:SiO$_2$ stack. Right: TRIDYN simulation of the sample series TM5, which were Co$^+$ ion implanted with a kinetic ion energy of 40 keV. The following fluences are shown: (a) 1.0×10^{14} cm^{-2} (b) 5.0×10^{14} cm^{-2} (c) 1.0×10^{15} cm^{-2} (d) 5.0×10^{15}cm^{-2} (e) 1.0×10^{16} cm^{-2} (f) 5.0×10^{16} cm^{-2}.

3.2.2. Ion Irradiated Planar Granular CoCrPt:SiO$_2$ Films

Apart from studying the influence of modifications to the substrate surfaces on the magnetic properties, the tailoring of FM thin films by ion implantation is also the focus of many investigations.[2,325–328] Particularly in the case of a stacked film system where the effects arising from the intermixing of the layers by the ions will be of particular interest. In a CoCrPt:SiO$_2$ system the effects that arise from concentrating one of the alloying elements is also of interest. For this work SiO$_2$was added to the CoCrPt system investigated, to obtain exchange decoupled grains.[35,329] Subsequent ion implantation can then affect the exchange decoupling, which will also be investigated here.

In this subsection, the results from measurements of the TM5 sample series are presented. For the TM5 series the stack design was chosen to match that used in a previous study.[32,128] The unirradiated TM5 wafer was provided by our cooperation partners of the group of Prof. Dr. Manfred Albrecht. It was implanted with Co$^+$ ions, where the fluence was varied in the range between 1.0×10^{14} cm^{-2} and 9.0×10^{15} cm^{-2}. This range was divided into 17 equally spaced fluences. These results will be compared to those from a non-irradiated sample. The idea is to obtain information about the tailoring effect of the implantation onto the magnetic properties. The main goal was to find out the influence of the intermixing due to the ion implantation and the concentration of Co$^+$ ions inside the FM CoCrPt:SiO$_2$ layers. This series was prepared with a larger range of fluences compared to the previous investigations. This system proved to be more difficult to measure using standard FMR techniques such as those employed in the previous section. There a two significant contributions to this problem. Firstly, the CoCrPt:SiO$_2$ has a very high anisotropy compared to the CoCrPt system measured previously, this means that the field and frequencies required to excite the precession are very high. Secondly, the CoCrPt:SiO$_2$ system has SiO$_2$ content added to exchange decouple the grains, this allows the individual grains to precess with their own phase and so the resonance
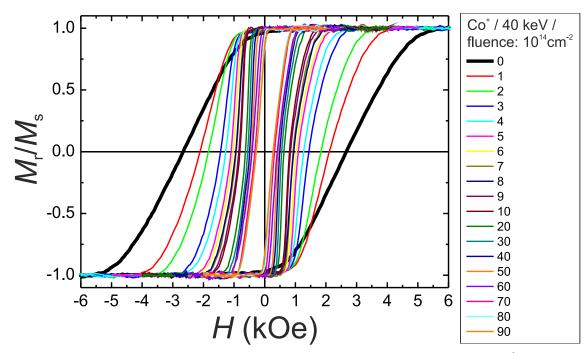
Fig. 3.19 Polar MOKE measurements of the TM5 samples. The samples were ion implanted with Co^+ ions with an energy of 40 keV. The fluences are increasing from 1.0×10^{14} cm^{-2} to 9.0×10^{15} cm^{-2}.

signal is greatly broadened and its amplitude is correspondingly decreased. Because, the FMR signal is rather noisy compared to the measurements of the Py samples in the first section, it is thought that the absorption signals is present but is hidden by the system noise floor. Consequently, one has to say that the FMR measurements could not be analysed, however TRMOKE measurements could be carried out. This suggests that the TRMOKE pump beam may be able to apply a much higher energy excitation than the VNA-FMR microwaves which were used. An additional factor is that the TRMOKE might be more sensitive (when the film thickness is of the order of penetration depth, for thicker film FMR can give a larger signal as it measures the volume).

Preparation   This sample series was prepared onto one side of a glass wafer, typical of the type used for recording media, at the Hitachi Research centre. The stack is built up as follows: first a Cr (5 nm) seed layer was deposited, this is for adhesion and to transition from the glass to metallic layers. Then, in a two-step process with different partial pressures, the Ru was magnetron sputtered onto the Cr. The first Ru layer is 8 nm and the second is 12 nm thick. These layers are crucial for the epitaxial growth of the $CoCrPt:SiO_2$ layers in a hcp structure and therefore they are responsible for the local perpendicular anisotropy of the grains being aligned along the film normal. A subsequent deposition of two $CoCrPt:SiO_2$ layers was done. The difference between the layers is the Ar^+ and O_2 content during the deposition. The first $CoCrPt:SiO_2$ layer was magnetron sputtered in a 100 % Ar^+ atmosphere and is 10 nm thick. The second $CoCrPt:SiO_2$ layer was deposited under an atmosphere of 99.3 % Ar^+ and 0.7 % O_2. It has a thickness of 7.5 nm. In the last step a carbon cap layer, to prevent oxidation, with a thickness of 4 nm was deposited. The entire stack is shown in Fig. 3.18 on the left side and finally reads as: glass/Cr(5 nm)/Ru(8 nm)/Ru(12 nm)/$CoCrPt:SiO_2$ (10 nm)/$CoCrPt:SiO_2$ (7.5 nm)/C(4 nm).

Afterwards, the wafer was cut into pieces of 5×5 mm^2 with a diamond saw. These samples were then ion implanted with Co^+ ions. SRIM (not shown) and TRIDYN simulations were performed to simulate the effect of the ions at different fluences. These give a theoretical picture of the intermixing effects and the
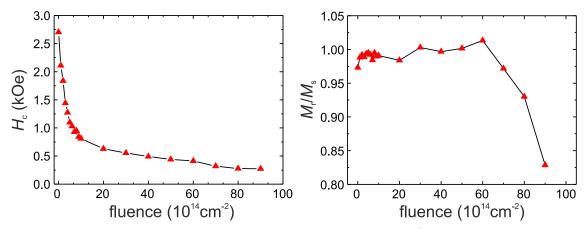
Fig. 3.20 (a) PMOKE results, which depict the decreasing H_c with increasing Co$^+$ - fluence. (b) PMOKE results showing the normalised remanence versus the implanted ions fluence. The lines are just guides for the eyes.

erosion on the surface that comes from the ions. First it was necessary to perform a SRIM investigation to get information about the implantation depth for Co$^+$ ions as a function of energy. This information was then used to decide which energies to use for the TRIDYN simulation (TRIDYN simulations account for more effects, like diffusion etc., and therefore they need more calculation time). To simplify the TRIDYN model each of the sub-layers of the CoCrPt:SiO$_2$ and the Ru layers were modelled as a single layer which is possible because TRIDYN does not account for the crystallographic properties. A summary of the results is shown in Fig. 3.18(a) – (f). The simulations were performed with $E_{kin} = 40$ keV and a fluence ranging between 1×10^{14} ions/cm^2 and 9×10^{16} ions/cm^2. The results presented in Fig. 3.18 are assigned to the fluences as follows: (a) 1×10^{14} ions/cm^2, (b) 5×10^{14} ions/cm^2, (c) 1×10^{15} ions/cm^2, (d) 5×10^{15} ions/cm^2, (e) 1×10^{16} ions/cm^2, and (e) 1×10^{16} ions/cm^2. The simulation plots show the relative concentration of the stack components in percent versus the depth in Angström. Figure 3.18(a), (b), and (c) reveal that the intermixing effect is dominant compared to the erosion and implanted Co content. The implanted Co content is rather small (< 1 %) and no erosion of material from the surface is observable. In the graphs that follow this behaviour changes significantly. Apart from the increasing intermixing effects of the stack components, where particularly the cap layer, both of the CoCrPt:SiO$_2$ layers, and both of the Ru layers are influenced, the erosion also increases in influence. Moreover, the concentration of Co increases from 5 % in (d) over 10 % in (e) up to more than 20 % in (f), the Co is mainly distributed inside both of the CoCrPt:SiO$_2$ layers. Figure 3.18(f) reveals a complete erosion of the Carbon cap layer. On the basis of these results a Co$^+$ ion implantation energy of 40 keV was chosen and the range of fluences used was decided. In particular it was considered important that the erosion of the surface should be avoided and therefore, when considering that the error associated with the TRIDYN model could be quite large, the prepared samples were implanted at maximum fluence of 9×10^{15} ions/cm^2.

PMOKE and SQUID Results The first experiments were carried out using polar MOKE measurements. The results for the entire sample series are shown in Fig. 3.19. All loops depict a clear out-of-plane magnetisation, as well as an increasingly sharp switching transition. This is associated with a reduced switching field distribution, as will be shown later. This effect could be described by an increasing exchange coupling between the grains, or also by an alloying effect. Moreover, the increasing Co$^+$ fluences are accompanied by a decreasing coercivity, as the analysis of the PMOKE data shows in Fig. 3.20(a). As this result demonstrates, the main decrease occurs for fluences up to 1×10^{15} ions/cm^2. Therefore, the H_c cannot be tailored beyond this fluence value. The next analysis deals with the normalised remanence with respect
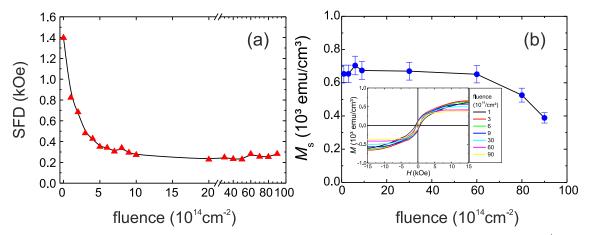
Fig. 3.21 (a) Analysis of the decreasing SFD for the TM5 sample series with respect to the implanted fluence of Co$^+$ ions. (b) M_s results evaluated from the SQUID measurements of the TM5 samples with respect to the fluence of Co$^+$ ions. The inset shows the entire data. For both graphs, the lines are just guides for the eyes.

to the fluence and shows that up to a fluence of 6×10^{15} ions/cm^2 the value does not change significantly. Beyond this fluence M_r/M_s significantly decreases as shown in Fig. 3.20(b). Due to the fact that these PMOKE measurements have been normalised as M_r/M_s because the implantation process changes the optical properties (reflectivity) and therefore one cannot be sure that the proportionality between $\vec{M}$ and the Kerr rotation is the same. To obtain information whether it is the M_r or the M_s is changing it was necessary to carry out SQUID measurements.

The SQUID measurements were done in the in-plane geometry ($\theta_B = 0°$), to see if the loops show any in-plane anisotropy contribution. The results are shown in Fig. 3.21(b) with the inset showing the complete set of measurements. This graph reveals, by a small coercivity, a small deviation from the in-plane hard axis orientation. As was mentioned in the last subsection, the samples are fixed inside a tube, which is utilised as a sample holder. The angular orientation of this tube is set by eye and thus, the angular error associated with this adjustment can explain the deviation of hysteresis loops from an ideal hard axis loop. The data were analysed to obtain the saturation magnetisation M_s and this is shown in the main graph. As for the M_r/M_s results, M_s stays nearly constant up to a fluence of about 6×10^{15} ions/cm^2. This constant value was determined to be 670(20) emu/cm^3. From a fluence of about 6×10^{15} ions/cm^2 M_s starts to decrease reaching a value of 390(20) emu/cm ^{3} at a fluence of 9×10^{15} ions/cm^2. From this behaviour, one can conclude that M_r behaves in a similar manner and also decreases after 6×10^{15} ions/cm^2. Furthermore, the question has to be answered, if this decrease of M_s is scalable over a broad fluence range or if it also reaches a constant value. As shown in the preparation paragraph earlier and in the simulation plots [see Fig. 3.18(e)] at higher fluences a problem arises from the erosion of the surface. Therefore, the range over which on can tailor the M_r and M_s without eroding the surface is rather small.

To achieve more detailed information about the reversal process, the hysteresis data obtained by the PMOKE were analysed by making use of the SFD fit procedure (as explained in chapter 2). The result of this process is plotted against the fluence and is shown in Fig. 3.21(a). Similar to the behaviour of H_c, the SFD significantly decreases already at low fluences and from a fluence of about 5×10^{14} ions/cm^2 the values reach a constant level. This means that no further change to the SFD can be achieved by ion implantation beyond the latter fluence.

The behaviour described here, for the variation of H_c, M_r/M_s, and the SFD with fluence is similar to that which was already reported in the literature.[32,128] After the investigation of the changes to the static magnetic properties induced by the ion implantation, the influences of the implantation on the dynamic
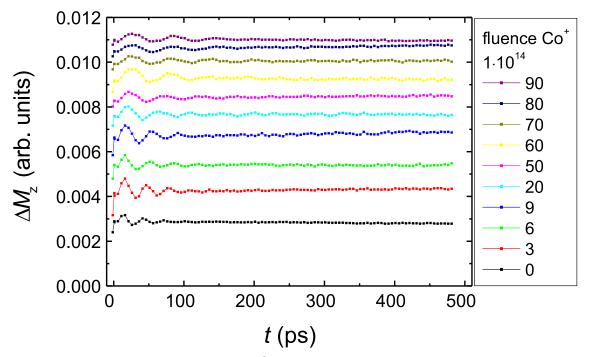
Fig. 3.22 Results of TRMOKE measurements of Co$^+$ ion irradiated CoCrPt:SiO$_2$ with different fluences. ΔM_z versus time is plotted.

properties were studied.

TRMOKE measurements were carried out to show, how the ion implantation acts on the dynamic magnetic properties. In contrast to the PMOKE measurements, for this experiment, only a subset of the samples was used. The results of the TRMOKE measurements are shown in Fig. 3.22. This graph shows the change in the z-component of the magnetisation (ΔM_z) plotted against time. Apart from the unirradiated sample, the samples exposed to a lower fluence of implanted ions show a more pronounced oscillation with a faster decay compared to the samples with a higher implantation fluence. The precessional decay data shown in Fig. 3.22 were fitted by a damped sinousoidal fitting function, the frequency and the decay time results that were obtained were plotted with respect to the Co$^+$ ions fluence. This evaluation is shown in Fig. 3.23(a). The frequency is shown by the black top triangles and black line. As one observes, over the entire fluence range up to 9×10^{15} ions/cm^2 the precessional frequency decreases from 31.4 GHz down to 16.8 GHz. The decay time is depicted by the red down triangles and red line, these data reveal an increase of the decay time from 33.4 ps to 99.8 ps with an increasing fluence. To yield information about the damping behaviour, the data obtained were analysed by plotting $(\omega\tau)^{-1}$ versus the fluence of Co$^+$ ions. This graph is shown in Fig. 3.23(b). Besides the spread in the damping values of $(\omega\tau)^{-1}$, the plotted data depicts a distribution around a constant value. The red line shows the mean value of all the data points. Thus, the value for the damping constant could be determined to be $(\omega\tau)^{-1} = 0.114(6)$. This value is consistent with the value for Gilbert damping determined using a TRMOKE by Mizukami.[235]

Summary In this subsection, the effects of Co$^+$ ion implantation on the magnetic properties of a CoCrPt:SiO$_2$ recording media samples were studied. Here, the static and the dynamic magnetic properties were investigated in detail. Based on the findings of previous investigations,[32,128] first SRIM and TRIDYN simulations were performed to uncover the right range of parameters for the implantation of
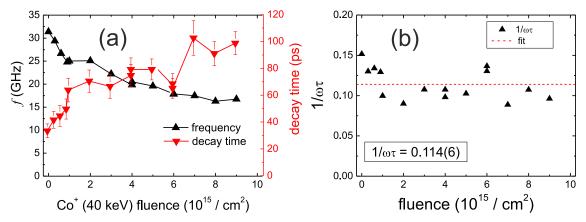
Fig. 3.23 (a) shows the frequency-dependence (black triangles) versus fluence (right y-axis). The decay time dependence is shown by the red triangles (left y-axis). (b) shows the plot of $(\omega\tau)^{-1}$ versus the increasing fluence. $(\omega\tau)^{-1}$ is equivalent to the Gilbert damping constant of the Landau-Lifshitz-Gilbert equation and the determined value is $(\omega\tau)^{-1}$ = 0.114(6).

Co$^+$ ions into the CoCrPt:SiO$_2$ layers. After the implantation all samples were measured using a PMOKE. The results obtained for H_c, M_r/M_s, and the SFD were consistent with the investigations from the literature mentioned previously. As was shown, the SFD and H_c decrease with increasing fluences and in both cases the decrease takes mainly part in the region of lower fluences. The results for H_c show that the SFD decreases more slowly at lower fluences, whereas for higher fluences the rate decrease has reached a nearly constant value. The M_r/M_s results show, that the value stays constant up to a fluence of 6×10^{15} ions/cm^3 and then starts to decrease. In addition, the SQUID measurements reveal a decreasing M_s for Co$^+$ fluences above 6×10^{15} ions/cm^2, which is consistent with the results for M_r/M_s from PMOKE. Therefore, one can conclude a simultaneous decrease of M_r, as well. The next studies were made using the TRMOKE setup. The results show a decreasing frequency with increasing fluence and furthermore, an increasing decay time with increasing fluence. Moreover, the damping could be determined as being $\alpha \approx (\omega\tau)^{-1} = 0.114(6)$, which is equivalent to the values found in the literature.[235]

3.2.3. Granular CoCrPt:SiO$_2$ Film on Nanocones

The pre-structuring of surfaces on the nanoscale is a promising technique to modify and finally to control the magnetic properties of materials used for applications, e.g. in spintronic devices or recording media.[293,330–332] This pre-structuring can be achieved by ion irradiation induced self-organization[56], ion irradiation in combination with lithographically defined masks[333], or nano-imprinting.[334] In order to use the resulting systems the morphology induced magnetic effects must be analysed. Currently, more and more studies deal with these effects due to the increasing demand for tailored magnetic materials.[38,42,48]

Electron beam lithography on the one hand gives a high accuracy but on the other hand, it suffers from its slow speed when large but detailed areas are to be structured. Self-organised structures made by broad ion beam erosion can meet this challenge. Here, GaSb nanocone templates were used, which were created from GaSb wafers by ion beam erosion, as was discussed in chapter 2.[58]

For the magnetic coating of the nanostructures granular CoCrPt:SiO$_2$ is used. It is a well-known hard magnetic material, which has been used as a magnetic recording material for several years.[23] The SiO$_2$ is added to magnetically decouple the grains from each other.[32]

The subsection is organised as follows: First it will be explained, how the GaSb nanocone templates were prepared and moreover, their structural characterization will be shown. Then we present the growth behaviour of the granular CoCrPt:SiO$_2$ on top of the cones. Finally, in the last paragraph, the influence of the nanocone size and the SiO$_2$ content on the exchange coupling of the grains as well as on the remanence and coercivity will be discussed.

Preparation   These self-assembled periodic nanostructures were prepared from a conventional GaSb(001) wafer using an ion beam erosion technique. The wafer was cut into 1×1 cm^2 pieces, which were then mounted onto a water-cooled fixture with a Cu mask. The Ar pressure during sputtering was 2.4×10^{-4} mbar. The broad Ar$^+$ ion beam had a normal incidence on the GaSb surface with ion kinetic energies of 200, 800, and 1200 eV, used to produce nanocones of selectable size. The ion kinetic energy range of 200 – 1200 eV obtains the best results with respect to homogeneity and ordering. As an aside, due to a discussion with Dr. Stefan Facsko concerning the question: "What happens below a sputter energy of 100 eV and above 1200 eV?", an answer could be determined. The answer to the first question is that there exists a threshold, below which no sputter process can occur, but its value is not exactly known. Furthermore, above 1200 eV the cones become more and more disordered and the cone ends will become more and more planar. Figure 3.24 shows a cross-section HR-TEM micrograph of the nanocones prepared with $E = 200$ eV. Besides the clearly visible crystalline volume, the surface of the GaSb cones is amorphous. This amorphous film is roughly less than 5 nm thick and reflects the dependence on the average penetration depth of the ions. The average cone height at this energy is 32(3) nm.

The GaSb nanocone pattern is quite uniform with a homogeneous distribution of cones across the substrate surface. The cone size depends on the ion energy, i.e. the higher the energy the larger the cones[155]. The height h, the diameter d as well as the aspect ratio of the nanocones, as determined using AFM for the prepared samples are summarised in table 3.9. Nanocones with heights of 32 to 330 nm and diameters of 28 to 120 nm can be fabricated using ion kinetic energies of 200 – 1200 eV, respectively. Note that when interpreting the AFM images one has to take the AFM tip-shape into account, i.e. the measured height profile is a convolution of the real cone profile and that of the tip's apex, leading to an underestimation of the height.

The AFM images also indicate some imperfections in the structural order. A possible cause of this might be defects that were present in the initial substrate or a blocked cone formation that is due to limited neighbour spacing. These effects lower the hexagonal short-range order.
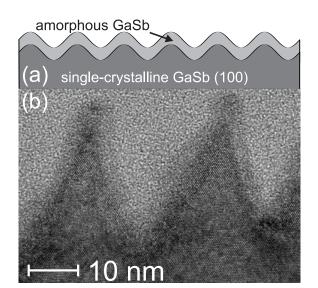
Fig. 3.24 (a) Schematic sketch of the microstructure. (b) Cross-sectional transmission electron micrograph of the uncoated GaSb(001) nanocones obtained with $E = 200$ eV.
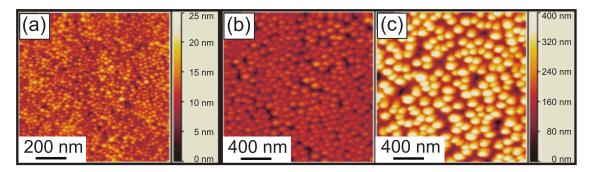

Fig. 3.25 AFM images of uncoated GaSb nanocones for ion energies E of (a) 200 eV, (b) 800 eV, and (c) 1200 eV.

For the ferromagnetic (FM) coating of the nanocones, first a 5 nm thin Ta adhesion layer was DC-magnetron sputtered followed by a two-step (12 nm and 8 nm) Ru buffer layer to support the high perpendicular anisotropy as well as the c-axis orientation of the granular FM layer.[6,294,335–337] The first Ru layer is sputtered at a lower Ar^+ pressure than for the second Ru layer which was processed at 7×10^{-2} mbar and this second layer is the one which is crucial for the perpendicular magnetisation. Further details of two-step Ru buffers are discussed elsewhere[9,293,336]. Subsequently, the 15 nm thick FM layer with the composition $[(Co_{90}Cr_{10})_{80}Pt_{20}]_x:(SiO_2)_{1-x}$ was deposited. This stack is known to grow in a hexagonal close-packed (hcp) columnar structure onto the substrate[332]. To optimize the SiO_2 content, samples with 8 at.% and 12 at.% of SiO_2 were prepared. The SiO_2 modifies the intergranular exchange coupling[57]. The optimal value for minimizing the intergranular exchange on planar substrates is reported by Dutson *et al.*[338] to be about 10 at.% SiO_2. Finally, a 4 nm diamond-like carbon (DLC) layer protects the stack from oxidization.

Tab. 3.9.: Ion erosion parameters.

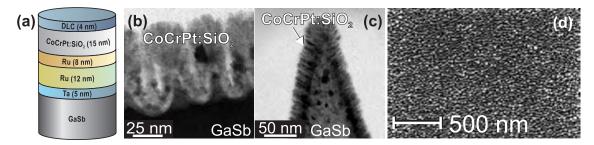| E (eV)	fluence (Ar^+/cm^2)	flux ($Ar^+/(cm^2 \times s)$)	l_c (nm)	h (nm)	aspect ratio
200	1.0×10^{18}	5.0×10^{14}	28(6)	32(3)	1 : 1.14
800	5.0×10^{17}	2.5×10^{14}	86(24)	170(30)	1 : 1.98
1200	1.5×10^{17}	2.0×10^{14}	120(42)	330(50)	1 : 2.75

Fig. 3.26 (a) Sketch of the full sample stack. TEM cross-sections of samples prepared with (b) 8 at.% SiO$_2$ on cones made with $E = 200$ eV, and (c) with 12 at.% SiO$_2$ on cones made with $E = 1200$ eV. (d) SEM image of cones prepared at $E = 200$ eV (height: 32 nm and diameter: 28 nm). They are coated with CoCrPt:SiO$_2$.
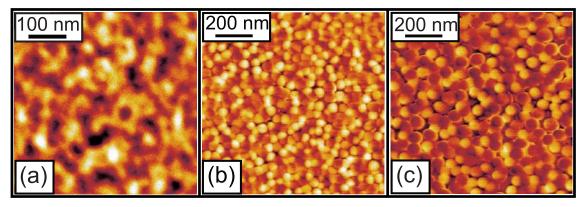

Fig. 3.27 MFM images showing the demagnetised state of the CoCrPtSiO$_2$ coated nanocones (8 at.% SiO$_2$) prepared with ion energies of (a) 200 eV, (b) 800 eV, and (c) 1200 eV.

Thus, the total height of the complete stack depicted in Fig. 3.26(a) is 44 nm.

Fig. 3.26(d) shows an SEM image of the magnetically coated, still separated cones. On this spot the short-range hexagonal ordering is slightly more visible as compared to the area shown in the AFM images in Figures 3.25(a) – (c).

To gain a detailed picture of the film growth on the different cone sizes cross-sectional TEM images were taken. Figures 3.26(b) and 3.26(c) show the corresponding samples. The nanocones were prepared with 200 eV (1200 eV) ion energy and with 8 (12) at.% SiO$_2$ content in the FM-layer, respectively.

One can see the effect of the cone size on the shape of the magnetic stack. The substrate which was produced at a lower sputtering energy exhibits broader cone ends in comparison to samples prepared at a higher energy.

Measurements   The measurements in this subsection were carried out by our cooperation partners at the group of Prof. Dr. Manfred Albrecht and by Dr. Gaspare Varvaro.

Here, the local magnetic properties are presented, which are determined from magnetic force microscopy (MFM). Later, the findings of the integral magnetic properties which were investigated using a polar magneto-optical Kerr effect (MOKE) and a vector vibrating sample magnetometer (vVSM) are shown.

The MFM images shown in Figures 3.27(a) – (c) were made of the sample in its demagnetised condition. Samples of both series (8 and 12 at.% SiO$_2$) present a similar magnetic domain structure in the virgin state which changes with increasing sputtering energy as shown in Fig. 3.27 for samples with a 8 at.% SiO$_2$ content. At the lowest ion energy (200 eV), the MFM shows the presence of larger magnetic domains of about 40 – 100 nm in width that extend over several nanocones. At higher ion energies (800 and 1200 eV) the samples predominantly show a single-domain behaviour even if a few of larger domains are still visible.
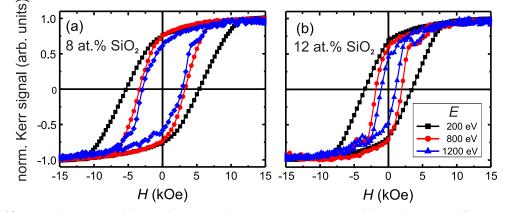
Fig. 3.28 Polar MOKE hysteresis loops of samples with (a) 8 at.% and (b) 12 at.% SiO$_2$ each on three different nanocone sizes measured at ambient temperature.

When this information is combined with that seen in the TEM cross-section images the reason for the domain behaviour observed becomes clear. The growth of the FM stack on the smaller cones causes a close packing of the magnetic grains and thus a coupling between the grains on the cones. For larger cone sizes the FM film grows on the side-walls, the film is thicker near the apex of the cone an thinner near base. Thus, the exchange coupling between the magnetic cones is strongly reduced leading to well-separated single-domain magnetic cones.

The sample series with 12 at.% SiO$_2$ (not shown) shows less contrast than with 8 at.% (measured with the same MFM-tip). The reason is an increase of the decoupling of the grains at a higher SiO$_2$ content. Apart from this, the results were similar for both series. One should also consider that the oxide diffuses to the boundaries of the grains, and therefore its content is responsible for the decoupling of the magnetic exchange interaction between the individual grains. This effect is described in more detail by Yingfan[309]. It is also established that the Cr in the alloy partially diffuses to the boundaries as well[309], dis also decouples the grains.

Fig. 3.28 shows the perpendicular magnetisation reversal of both sample series measured at room temperature by using a polar MOKE setup. The loops indicate that both the normalised remanence (M_r/M_s) and the coercivity H_c, decrease with increasing ion energy, i.e. cone size. These results can be explained by considering the combined effect of both the angular spread of the local c-axis of the grains and the strength of the intergranular exchange coupling. Both depend on the magnetic microstructure of the film on the nanocones. As explained above, on small cones (200 eV ion energy) one mainly has a bunch of FM grains on top of each cone tip [see Fig. 3.26(b)]. Whereas on the larger cones, the stack can cover the full cone surface as a flat film [Fig 3.26(c)]. Hence, the angular spread of the anisotropy axes on the cones results in a lower remanence (due to symmetry reasons, the moment from material on one side-wall partially cancels out that from the other) and coercivity (due to a tilt of the material on the side-walls relative to the applied field).

Interestingly, at 8 at.% SiO$_2$ content the remanence for both the 200 eV and 800 eV cones is the same, i.e. $M_r/M_s = 0.77$. For the largest cones prepared with 1200 eV $M_r/M_s = 0.60$ is smaller. From the TEM cross-sections and the domains determined from the MFM images one would expect the opposite, i.e. a difference in remanence for only the smallest cone size.

Compared to that, for the other series with 12 at.% SiO$_2$ M_r/M_s decreases with increasing ion energy (cone size) from 0.69 to 0.46. The coercivity H_c decreases in both series similarly, with the absolute values being larger overall for that with 8 at.% SiO$_2$ content, as expected.

These effects can easily be studied by simulating the hysteresis loops using the Stoner-Wohlfarth model.
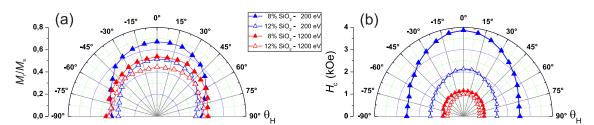
Fig. 3.29 (a) Angular dependence of the normalised remanence M_r/M_s and (c) of the coercivity H_c.

This model is a simplification that approximates the system as a cone-shaped substrate with columnar shaped grains distributed on top and having their easy axis perpendicular to the cone's surface.

The intergranular exchange–coupling among grains on the same cone is smaller in the case of 12 at.% SiO$_2$. This is suggested by the observation that for 8 at.% SiO$_2$ higher values of the normalised remanence and coercivity are measured. One also observes a decreasing switching field distribution (SFD) with increasing cone size. The comparison of Fig. 3.28(a) and Fig. 3.28(b) shows a significantly smaller SFD for 12 at.% SiO$_2$ content.

The effect of the substrate shape and the oxide content on the magnetic behaviour was further investigated by analysing the polar angular dependence of both remanence and coercivity. For this, a set of hysteresis loops were measured by an ADE-Technologies model 10 vVSM equipped with a rotating electromagnet. The field was applied along different directions in the yz-plane denoted by the angle θ_H as depicted in Fig. 3.30.

Figure 3.29(a) shows the angle-dependent normalised remanence and Fig. 3.29(b) the corresponding coercivity, each figure is for the two types of cones (blue and red colour) and both SiO$_2$ contents (solid/open symbols), respectively. The angular-dependence of the remanence is influenced by the easy axis distribution, the intergranular exchange coupling, and the magnetostatic effects. For a perpendicular recording media one expects the easy axis at $\theta_H = 0°$. In Fig 3.29(a) one can see, that for 12 at.% SiO$_2$ and 1200 eV cones (open red triangles) the sample even appears to be nearly isotropic. The samples on the small 200 eV nanocones (blue symbols) show the strongest anisotropic behaviour. By reducing the intergranular exchange coupling, the angular dependence of the normalised remanence (typical for a system with a spread of the easy axis) becomes more and more uniaxial.

The angular dependence of the coercivity exhibits a slightly different behaviour. There, the sample with 12 at.% SiO$_2$ on 1200 eV cones shows an anisotropic behaviour whereas that with 8 at.% SiO$_2$ on 1200 eV cones H_c is isotropic.

Simulation This simulation was performed and analysed by Stephan Günther.[339] A single cone can be modelled as being covered by a collection of exchange-decoupled grains, this kind of system is an ideal candidate for a Stoner-Wohlfarth model[340]. In this case one can neglect the exchange and dipolar interactions between the grains, this includes both interactions on the same cone and between different cones. Therefore, the relative spacing and position of grains does not need to be taken into account. All that matters is the angle of the field relative to the easy axis of the grains. As the grains are uniformly distributed over the surface of the cone, and the easy axis is assumed to lie along the local surface normal, then we have an array of grains with the easy axis angle distributed evenly between 0 and 2π rad. Each grain will contribute its own independent hysteresis loop to the signal measured in the experiment (which is an average over many grains). Therefore we can approximate the experimental result by averaging the hysteresis loops of a set a grains where the easy axis direction is varied with respect to the applied field direction. The problem geometry is depicted in Fig. 3.30 for particular case. For the simulation presented in Fig. 3.31 72 CoCrPt:SiO$_2$ particles with gives a angular spacing of 5°. The influence of the morphology was investigated by modifying the
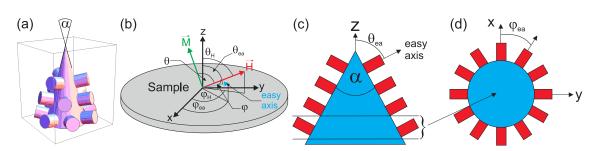
Fig. 3.30 (a) and (b) Sketch of the simulation geometry for one cone covered with CoCrPt:SiO$_2$ particles. For clarity only 13 particles are displayed. (c) cross-sectional side view of the model geometry with the extracted part shown by the region in between the black vertical lines at the bottom. (d) cross-sectional top view of one simulated conic-section with the grains uniformly distributed around.

cone angle α. In Fig. 3.31 the results of this simulation are shown. Two calculations are presented for cone angles of $\alpha = 150°$ (red triangles) and $\alpha = 90°$ (blue triangles). $\alpha = 150°$ corresponds to the small cones (200 eV/$h \approx 30$ nm), whereas the tall cones (1200 eV/$h \approx 330$ nm) were simulated with $\alpha = 90°$. The results for M_r/M_s are shown in Fig. 3.31(a) and H_c/H_a in Fig. 3.31(b). Comparing the experiment in Fig. 3.29(a), to the simulation in Fig. 3.31(a), one finds a similar behaviour. The normalised remanence decreases with an increasing cone size. The values measured by vVSM are, however significantly smaller than the values for the model, which could be due to a small residual exchange-coupling between the grains. Moreover, the normalised remanence for the planar samples is smaller than 1[32]. Furthermore, the comparison of Fig. 3.29(b) and Fig. 3.31(b) depicts a decreasing coercivity with increasing cone size. The discrepancies between the simulation and the measurements are due to two main influences. Firstly, there exists an exchange coupling between the grains which has been neglected in the simulation. Secondly, the Stoner-Wohlfarth model assumes a reversal of magnetization by coherent rotation. In reality the reversal may be realised by domain wall nucleation with subsequent propagation (a process which requires a degree of exchange coupling between the grains) which typically leads to smaller coercive fields.

Summary We have shown how to prepare a self-assembled network of magnetically coated GaSb nanocones with a high homogeneity using an ion erosion technique. We have investigated the morphology induced effects of such a pre-structured template on the magnetic properties of a hard magnetic coating of CoCrPt:SiO$_2$. We have varied the SiO$_2$ content and the size of the nanocones. MFM investigations revealed that the small nanocones have widespread connected domains, whereas the larger nanocones created by higher sputtering energies yield predominantly single-domain magnetisation. The analysis of the hysteresis loops shows that the remanence and coercivity decrease with increasing cone size or SiO$_2$ content. This is due to the angular distribution of the magnetic grain's c-axis and the intergranular exchange coupling strength. These results could be qualitatively reproduced by simulations.
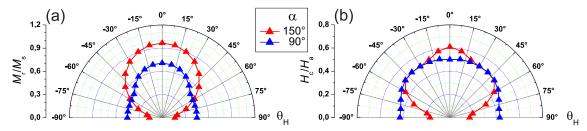

Fig. 3.31 Mathematica™ simulation of the coated nanocones with respect to the cone angle (α) and the applied field angle (θ_H). (a) Angular dependence of the normalised remanence (M_r/M_s) and (b) of the normalised coercivity (H_c/H_a). The lines are guides for the eye only.
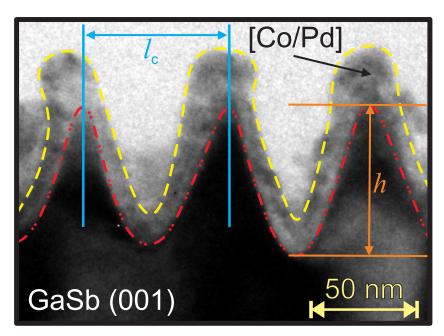
Fig. 3.32 Cross-sectional transmission electron microscopy image of a $[Co/Pd]_8$ multilayer deposited on top of nanocones ($l_c = 75$ nm). Dashed lines depict the structural and coating characteristics.

3.3. [Co/(Pt,Pd)] Multilayers on Nanocones

Here, the morphology-induced changes to the magnetic properties of exchange coupled thin ferromagnetic [Co/Pd] multilayers with perpendicular magnetic anisotropy on GaSb nanocones were investigated. [1,48,341–344] In contrast to the granular $CoCrPt:SiO_2$ films discussed in the previous section, this material is a magnetically continuous film. [27–31] Previous investigations presented in the literature were studying the effects of ion induced changes on the magnetic properties of [Co/Pd] and [Co/Pt] multilayer systems, [345,346] as well as on the curvature-induced effects on the magnetic properties of spherical or self-assembled particle arrays coated with [Co/Pd] or [Co/Pt] multilayers. [55,347–351] This material is, in addition to granular $CoCrPt:SiO_2$ media, a candidate for upcoming PMR applications, particularly in the field of BPM. [352,353] In contrast to the granular $CoCrPt:SiO_2$ system, these multilayer films grow as a magnetically continuous thin film on the substrate, as will be shown in the following. The focus here was on the effect of the underlying nanocone structure onto the exchange coupling.

Before the [Co/Pd] system was studied, we optimised the multilayer stack regarding the number of multilayer repetitions, Pt thickness within the multilayer, and the thickness of the Co within the multilayer by using a test [Co/Pt] system. Both of the multilayer systems, [Co/Pd] and [Co/Pt] , have nearly the same magnetic properties and so the change from the [Co/Pt] to the [Co/Pd] system does not affect the investigated results. [354,355] The advantage of working with [Co/Pd] was the lower pressure needed for the deposition process, due to technical issues this decreases the pumping load. For this reason the sample preparation was changed.

Preparation of the Substrate The self-assembled nanocones were created on GaSb(001) using the ion erosion technique described previously. [56] The densely packed cone-like nanostructures are produced by normal incidence ion erosion of crystalline GaSb(001) surfaces using Ar ions. [56] A Kaufman type ion gun with a single graphite extraction grid (5 cm diameter) was used. The irradiation was done at room temperature. The average distance between the cones, which we call the characteristic length [l_c,
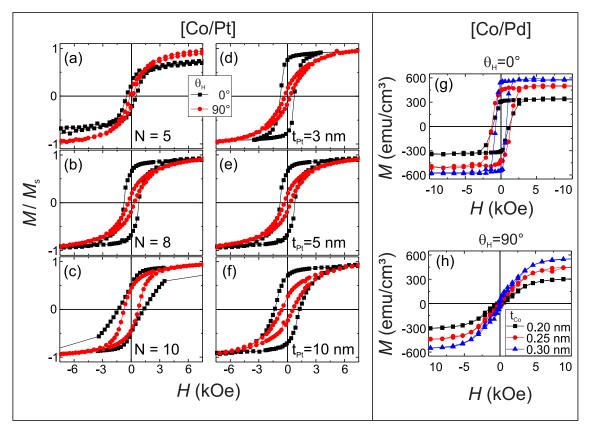
Fig. 3.33 Inside the left panel the SQUID loops of the [Co/Pt] samples measured in- and out-of-plane are shown. The panels show the normalised magnetisation with respect to (a) – (c) the number of bilayer repetitions N and (d) – (e) t_{Pt}. In the right panel the SQUID hysteresis loops of the [Co/Pd] samples measured at $\theta_H = 0°$ (top) and $\theta_H = 90°$ (bottom) are shown. (g) – (h) show the absolute Co-thickness dependence of M.

see Fig. 3.32], is controlled by the kinetic energy of the incident Ar^+ ions. [155] The characteristic length increases with increasing ion energy. Two different ion energies of 400 eV and 1200 eV were used to produce nanocone structures with $l_c = 29(4)$ nm and $l_c = 75(7)$ nm, respectively. The cone height [h, see Fig. 3.32] and the hexagonal short-range ordering of the nanocones increase with increasing fluences. [158] The smaller cones (with an average height of 30(3) nm) were prepared with a fluence of 1.0×10^{18} Ar^+/cm^2. The larger cones with $h = 67(8)$ nm were prepared with a fluence of 1.5×10^{17} Ar^+/cm^2. The h/l_c aspect ratio for smaller cones is 1.0 and 0.9 for larger cones, respectively.

Optimisation of the Film   As a first test series, [Co/Pt] multilayers on *planar* GaSb were prepared by magnetron sputter deposition. The overall stack needs to be thin enough to avoid a filling of the troughs between the cones but at the same time still able to yield the highest perpendicular anisotropy.

During preparation the Ar partial pressure was 8.2×10^{-3} mbar and the deposition rate was 0.04 nm/s. For this sample series (A) the number of bilayer repetitions N was modified, i.e. GaSb/5 nm Pt/[0.28 nm Co/0.8 nm Pt]$_N$/2 nm Pt with $N \in \{5, 8, 10\}$. For the next series (B) three seed layer thickness $t_{Pt} = 3, 5,$ and 10 nm with $N = 8$ were prepared, i.e. a stack of GaSb/t_{Pt} Pt/[0.28 nm Co/0.8 nm Pt]$_8$/2 nm Pt. To avoid oxidation all samples are capped by a 2 nm Pt layer.

The magnetic properties were determined by superconducting quantum interference device (SQUID) magnetometry and a vector vibrating sample magnetometer (vVSM). The SQUID and AFM measurements were carried out by Stephan Günther in the group of Prof. Dr. Manfred Albrecht. Whereas, the vector-VSM
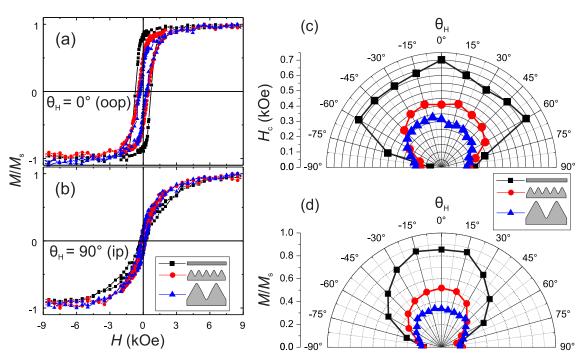
Fig. 3.34 Angle and cone size dependent hysteresis loops measured at room temperature. (a) $\theta_H = 0°$ (out-of-plane) and (b). $\theta_H = 90°$ (in-plane). Room temperature angular dependence of (c) coercivity (H_c) and (d) normalised remanence (M_r/M_s) of [Co/Pd]$_8$ samples with three different morphologies Lines are guides to the eyes only.

measurements were carried out by Dr. Gaspare Varvaro. The samples were measured with the external magnetic field applied either out-of-plane ($\theta_H = 0°$/oop) or in-plane ($\theta_H = 90°$/ip).

Figure 3.33(a) – (f) shows the SQUID hysteresis loops for ip (red circles) and oop (black squares) field directions of the [Co/Pt] samples. The left panels show the loops of the A series, i.e. for different bilayer repetitions, and the right panels show series B, which has different seed layer thicknesses. The normalised magnetisation M/M_s for $N = 5$ in Fig. 3.33(a) reveals an almost identical behaviour for both field directions, which suggests a weak net anisotropy for the system. In contrast, for $N = 8$ the square-like shape of the loop with high remanence M_r in the oop direction indicates an oop easy axis of magnetisation. Finally, for $N = 10$ [cf. Fig. 3.33(c)] one observes an increased coercivity but a decreased M_r at $\theta_H = 0°$. Therefore, we selected $N = 8$ as the optimised parameter (thinnest film given a sufficient oop anisotropy) and then moved on to optimise the seed layer thickness. This is shown in Figs. 3.33(d) – (f). All loops show an oop easy axis with equally high remanence. The optimal value which gives a low coercivity and a thin stack is found for $t_{Pt} = 3$ nm.

For the magnetic coating of the *nanocones* at room temperature, a [Co/Pd] stack (sample series C) was used instead of [Co/Pt]. However, since the properties of [Co/Pt] and [Co/Pd] are nearly the same,[354,355] the optimised values previously determined for the [Co/Pt] stack, were used. For this series (C) the Co thickness t_{Co} was modified, yielding three samples of 3 nm Pd/[t_{Co} nm Co/0.9 nm Pd]$_8$/2 nm Pd with $t_{Co} = 0.20, 0.25$, and 0.30 nm. The deposition rate was 0,04 nm/s for Co and 0.02 nm/s for Pd under a partial Ar pressure of 3.5×10^{-3} mbar. Figure 3.33(g) – (h) shows the SQUID loops of the [Co/Pd] sample series (C) measured in both oop (top) and ip (bottom) directions. In Fig. 3.33(g) and 3.33(h) the total magnetisation is given for three thicknesses. As expected, the loops show an increasing remanence and saturation magnetisation with increasing t_{Co}. The highest value is reached for $t_{Co} = 0.3$ nm, i.e. $M_s = 579$ G, whereas for $t_{Co} = 0.2$ nm $M_s = 340$ G. Moreover, for $t_{Co} = 0.25$ the highest coercivity of 1.3 kOe is found. It should be noted that $t_{Co} = 0.20$ nm is in the range of one atomic layer. Hence, it might be possible that the film is not
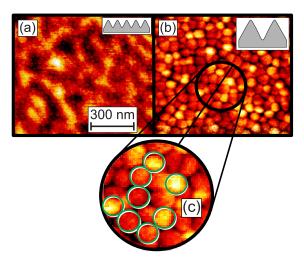
Fig. 3.35 MFM images of the [Co/Pd]$_8$ multilayers on (a) l_c = 29 nm and (b) l_c = 75 nm nanocones, respectively. (c) magnification with highlighted domains.

continuous. This in turn leads to a decreasing contribution of the interface anisotropy K_{if}. A comparable effect was observed for [Co/Pt] multilayers on Al$_2$O$_3$.[349] The smaller coercivity for t_{Co} = 0.30 nm could be ascribed to a decreasing K_{if} with increasing layer thickness.

Finally, the optimised magnetic stack on top of the GaSb pattern is Pd (3 nm) / [Co (0.3 nm)/Pd (0.9 nm)]$_8$ / Pd (2 nm) and has the desired out-of-plane magnetisation. The cross-section of the continuous film on the cones is shown in Fig. 3.32. The dashed lines depict interfaces for clarity. The film thickness on a large cone's apex is twice as large as on the side-walls, whereas no change in film thickness is observed for the sample with small cones.

Measurements   A vector vibrating sample magnetometer (vVSM) was used to investigate the angular dependence of the normalised remanence (M_r/M_s, where M_r is the remanence and M_s the saturation) and the coercivity (H_c) at room temperature. For these measurements a series of hysteresis loops were collected [see Fig. 3.34] with the external magnetic field applied along different polar angles θ_H ranging from $-90°$ to $+90°$, where $\theta_H = 0°$ is the sample's normal. In-plane angle-dependent measurements were also performed but are not shown, as they exhibit isotropic behaviour in agreement with the structural in-plane isotropy of the cone template. Note, the hexagonal order of the template mentioned before is only short-range and hence does not induce a long-range magnetic in-plane anisotropy.

The polar angle-dependent measurements of H_c, and M_r/M_s are shown in Figs. 3.34(a) and 3.34(b), respectively. The polar curves [see Fig. 3.34(c) and (d)] show a maximum of H_c and M_r/M_s at $\theta_H = 0°$ for all three samples, indicating the preferred direction for the perpendicular anisotropy. Data taken on templates with l_c of 29 nm (circles) and 75 nm (triangles) are compared to a reference sample on a planar substrate (squares). Both the coercivity (H_c) and the remanence (M_r) decrease with increasing cone size in the out-of-plane direction. The coercivity at $\theta_H = 0°$ decreases from 0.70 kOe (planar) past 0.41 kOe (l_c = 29 nm cones) down to 0.28 kOe (l_c = 75 nm cones). The in-plane values for H_c are all similar. Overall, the angular dependence of H_c, and M_r/M_s reduces with increasing cone size suggesting that the spatial variation of the anisotropy axis orientation increases with increasing ion energy. This is a clear proof for a tilted easy axis which is following the morphology of the nanocone pattern similar to the observations on magnetically capped spherical particles.[347]

The local magnetic properties were investigated using magnetic force microscopy (MFM) at room

temperature. The reference sample on a planar GaSb substrate was found to be in the multi-domain state, with a domain size of about 200 nm (not shown), which is typical for [Co/Pd] multilayer samples.[356] MFM images taken after ac-demagnetization of the [Co/Pd]$_8$ multilayers on templates with l_c of 29 nm and 75 nm are shown in Figs. 3.35(a) and 3.35(b), respectively. The sample with smaller cones (l_c = 29 nm) [Fig. 3.35(a)] is in a multi-domain magnetic state, where the domain size is in the range of 115(15) nm. The positions of the magnetic domain walls correlate with the locations of the cones, suggesting a pinning mechanism in the magnetization reversal process.[288] For the sample with cones of l_c = 75 nm [Fig.3.35(b)] a clear dark and bright MFM contrast is observed on the cone locations, indicating that individual magnetic structures are in a single-domain state. Furthermore, the MFM images suggest that neighbouring cap structures are more magnetically exchange decoupled. The decoupling mechanism might be similar to the one observed for magnetic caps on arrays of spherical particles. Here a thickness gradient in the [Co/Pd] multilayers results in a transition within the magnetic film from ferromagnetic (at the top of the cap) to paramagnetic closer to the base of the cone.[350]

Summary We have investigated the changes in the magnetic properties of exchange coupled [Co/Pd]$_8$ multilayers with perpendicular magnetic anisotropy on templates of ion-eroded self-assembled GaSb nanocones. Macroscopic magnetic measurements performed using vector VSM magnetometry indicate that all samples possess the magnetic easy axis perpendicular to the cone surface. The remanence as well as the coercivity decrease with increasing characteristic length and height. This due to a larger angular spread of easy axis which are following the morphology of the pattern. In addition, the MFM characterization shows, that in the case of small cone structures the underlying cone pattern results in a pinning of magnetic domain walls. Moreover, there is a clear correlation between the morphology and the positions of magnetic domain walls (please note that the film is exchange coupled). For the largest nanocones, exchange decoupled magnetic caps are achieved with single domain areas confined to the cones' apexes.

Chapter 4.

Summary and Outlook

The question that this thesis set out to address was: "Can morphology-induced changes and ion-irradiation induced changes to the magnetic properties of perpendicular recording media be used to help realise bit patterned media?" In this section we summarise the results of this work in the context of this question.

Due to the focus on bit patterned media, the materials initially chosen for this work were typical perpendicular recording media (e.g. CoCrPt:SiO$_2$, CoCrPt, [Co/Pd], [Co/Pt]). These materials are characterised by a high out-of-plane anisotropy and a controlled granular exchange decoupling ([Co/Pd] and [Co/Pt] are strongly coupled, CoCrPt:SiO$_2$ is strongly decoupled). The focus on BPM also affected the choice of the patterning technique, all of the morphology-dependent studies presented used IET to achieve a self-assembled nanocone structure on the GaSb(001) substrate surface. Compared to nanoimprinted or e-beam lithography structures, the order is relatively poor, for our research this system was a good choice because it would be relatively easy to obtain such structures on an industrial scale. For these investigations, the focus was on the static and dynamic magnetic properties which were studied using a variety of magnetometry techniques (e.g. VNA-FMR, TRMOKE, PMOKE, and vVSM). This study also relates the magnetic properties directly to the structural characteristics of the systems (measured by AFM, MFM, SEM, and TEM).

These systems are difficult to measure because when using a prestructured template the material is inhomogeneous and so effects like damping and inhomogeneous linebroadening (ILB) are strongly enhanced. One drawback found to the choice of the PMR materials was that its high anisotropy makes it difficult to obtain measurements using VNA-FMR and TRMOKE. As a consequence of this, a Py system was prepared which gave the opportunity to obtain dynamic measurements of a nanostructured film, in addition this well-known system could be simulated.

The sample systems studied here and the key results obtained, are summarised as follows:

- Cr (5 nm)/Py (20 nm)/Cr (3 nm) on GaSb(001) nanocones:
  - Focus: The effect of structuring on a strongly exchange coupled system with an in-plane shape anisotropy.
  - Results: Increased isotropic behavior and decreased $4\pi M_{\mathrm{eff}}$ with respect to l_c; increasing α and a vortex behaviour above a critical cone size; inhomogeneous linebroadening is decreased for the in-plane VNA-FMR measurement;
- [Co/Pt] and [Co/Pd] multilayers on GaSb(001) nanocones:
  - Focus: The effect of structuring a PMR media which has a strong exchange coupling.

– Results: Decreasing H_c and M_r/M_s with respect to l_c; exchange decoupled single domain particle at larger l_c;

• Granular CoCrPt:SiO$_2$ on GaSb(001) nanocones:

– Focus: The effect of structuring a PMR media which has a strong exchange decoupling.

– Results: Decreasing H_c and M_r/M_s with respect to l_c; exchange decoupled single domain particle at larger l_c;

• Planar granular CoCrPt:SiO$_2$ (Co$^+$ ion-irradiated) and Planar granular CoCrPt (two different anisotropies):

– Focus: Ability to change exchange-coupling of PMR media and to test the dynamic aspects.

– Results: VNA-FMR and TRMOKE measurements were successful (damping could be determined); increasing Co$^+$ implantation reduces the SFD, H_c, M_s, and M_r;

The results listed above are summarised in detail within the respective subsections. In the following we focus on the key results from this work.

Substrate Preparation   All nanocone patterns used in this work were produced by the IET using a sputter energy from 100 eV up to 1200 eV and different fluences. This preparation technique allows the tailoring of l_c, which in turn effects the aspect ratio and the cone shape (larger cones have a longer straight region on the sidewall). As was shown in chapter 3, the periodicity l_c depends on the sputter energy, whereas the spatial order is fluence- and flux-dependent. SEM and AFM images reveal a uniform distribution of the nanocones on the surface. In addition, TEM investigations revealed the presence of an amorphous GaSb cap layer, formed due to the sputter process.

Film Preparation   For the small cone sizes ($l_c < 40$ nm) it was observed that the different materials grow in different ways. Py grows as a uniform polycrystalline film which follows the underlying structure. The same behaviour was observed for the [Co/Pd] and [Co/Pt] multilayer films. Whereas the granular CoCrPt:SiO$_2$ film tends to form bunches of grains on the cone tips. For the medium sized cones ($l_c < 80$ nm). For these cones we have Py, [Co/Pd], and [Co/Pt] multilayer films, which grow in a similar way as for the small cone sizes. For the largest cones ($l_c > 80$ nm) there are only CoCrPt:SiO$_2$ samples. It was determined for these samples that the thickness of the coating changes as a function of the location on the nanocones. The coating is thinnest in lower regions in between the cones, whereas the largest grains grow on top of the cone ends. This effect is due to a shadowing during the deposition. This gradient in the coverage contributes to the exchange decoupling between the cones, or in other words, it enhances the interdot exchange decoupling. Also an increasing l_c increases the interdot exchange decoupling, which was observed for the CoCrPt:SiO$_2$ and [Co/Pd] multilayer samples on nanocones by MFM measurements.

Topological and Magnetic Structuring   The granular CoCrPt:SiO$_2$ and the exchange coupled [Co/Pd] multilayer films show a comparable behaviour. The MFM images obtained from the PMR recording media on the cone patterns show that in the case of smaller cones, the underlying nanocone structure results in a pinning of the magnetic domain walls. Moreover, this investigation yields a clear correlation between the topological features of the patterned substrate and the location of the domains. The MFM images for larger cones indicate that the individual magnetic structures are in a single-domain state. In addition, MFM images confirm that neighbouring cap structures are more magnetically exchange decoupled than observed for the smaller nanocone pattern.

Orientation of $\vec{M}$ Relative to the Underlying Structure   The analysis of the magnetometry results for CoCrPt:SiO$_2$ and [Co/Pd] showed that the magnetisation must follow the curvature of the nanocone structured substrate. This is indicated by the decrease of H_c and M_r/M_s. The same result was also shown by in-plane MOKE scans for the samples of Py on nanocones. Furthermore, from data obtained with the VNA-FMR (polar measurement) confirms these results for the Py samples. Moreover, these results could be corroborated by OOMMF (Py) and Stoner-Wohlfarth (CoCrPt:SiO$_2$) simulations.

Transition to Isotropic Behaviour   It was observed for all prestructered samples that by increasing characteristic length the anisotropy of the magnetic system can be decreased. In the case of Py the in-plane shape anisotropy is reduced, whereas for the PMR samples the effect of the out-of-plane crystalline anisotropy is altered.

Particular Observations Relating to Py on Nanocones   It could be shown that for cones with an $l_c \geq 40$ nm a vortex state is formed during the reversal process (in the ip geometry). A further interesting observation is the increase in the Gilbert damping, also for cones with a $l_c \geq 40$ nm (in the ip geometry). These two observations might be linked. The remaining question is, how does the vortex state dissipate more energy to the lattice or is there any other effect involved. Also it was shown that in case of the ip geometry VNA-FMR measurements, the inhomogeneous linebroadening is significantly larger compared to the oop geometry.

Technical Issues   One issue concerns the results for the series of Py on nanocones. Here, the α and ΔB_0 results showed that these measurements cannot be analysed using the commonly used resonance condition formula.[193] The reason for this problem lies in the morphology, which violates the assumption used in the derivation of this formula which is of a homogeneously magnetised infinite continuous film. Therefore a new formula has to be derived for the analysis of the dynamic magnetic properties for the case of a magnetic film on a nanocone structure. In particular, the creation of such a model is crucial to further the study of damping and the inhomogeneous linebroadening in 3D magnetic structures for applications such as bit patterned media.

Another issue that was identified is based on a discussion with Dr. Olav Hellwig. The much higher perpendicular anisotropy of conventional PMR media stacks are believed to be the reason why measurements with the VNA-FMR on the CoCrPt:SiO$_2$ and [Co/Pd] samples did not work. In addition, the intergranular exchange decoupling, which is enhanced by the SiO$_2$ additive, induces a broadening in the ferromagnetic resonance spectrum.

The nanocone structuring restricts the application of TRMOKE measurements due to the roughness, because at a certain cone dimension, the roughness spreads the reflection thus the intensity is too low for detection. Within the investigations of the planar CoCrPt, for the c06 sample the results of FMR and TRMOKE measurements are in agreement and these values could also be compared with values typically found in the literature. Except for the analysis of the damping, which revealed that the applied field used to bias the sample was insufficient to ensure the spins collinear and therefore a damping constant could not be determined. As well as this, improvements such as increasing the applied field range of the TRMOKE setup will allow a larger range of samples to be studied. Also, using samples with substrates (e.g. Si) which have an improved heat dissipation helps keep the average temperature low during the measurement.

Outlook In general a step back to more simple structures could help to find the right answer to the newly opened questions. With regards to the simulations of the Py on nanocone system, it was found that the behaviour of the magnetisation reversal is quite complex. Although the system can be successfully studied using micromagnetic modelling (e.g. OOMMF), the simulations for a single cone already take a long time to run and give only a picture of what is happening in the specific system configuration simulated. The in-plane simulations showed an unexpected behaviour of coercivity, which might be caused by the simulation of a single cone rather than a complete array. In order to create a more practical simplified model which describes the important contributions to the switching process in a more general way, it is probably necessary to first study simpler systems.

The analysis of the nanocone structured samples revealed a magnetic configuration of a high complexity due to factors like the orientation of the magnetisation following the surface profile, and thus such systems require new models of the linewidth for facilitating the analysis. Therefore, the first investigations should focus on the description of a simple 2D system, like one consisting of well defined stripes covered with magnetic material, where the equation for α and ΔB_0 can possibly still be evaluated with only a small change to the current linewidth formula [see Equation (2.47)]. If this works out it should be possible to develop a model from the existing formula for a system such as an individual cube or a well ordered cluster of cubes covered by a well defined magnetic film. These systems should be chosen in order to simplify the simulations, which will improve, apart from the derivation of the previously mentioned equation, the understanding of the magnetic properties of such a system.

As was mentioned in the subsection about the VNA-FMR setup, a new microresonator FMR setup has been developed recently which has the capability to measure even the smallest samples on the nanometre length scale. [177] This technique gives access to an more detailed picture of small magnetic structures. The underlying substrate pattern that would be needed for the microresonator studies should be prepared by e-beam lithography or nanoimprinting, because the accuracy of structures made by these techniques a is significantly better. For these measurements a low anisotropy material should be used due to the problems identified measuring the structured PMR materials. Nevertheless, in principle the techniques used in this thesis are well-suited for these studies, and therefore these results represent a good first step towards characterisation and understanding of the effects of morphology on the magnetic properties of thin film systems.
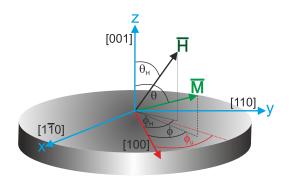
Fig. A.1 Polar coordinate system for an infinite uniformly magnetised single film (limiting case of an ellipsoid).

Chapter A.

Derivations of the General Resonance Conditions

Here, the derivations of the general resonance conditions for the ferromagnetic resonance with respect to the crystallographical structures, i.e. fcc tetragonally distorted (fct) and the hexagonally closed packed (hcp) structure is evaluated by making use of the formula by Baselgia [193]:

$$\left(\frac{\omega}{\gamma}\right)^2 = \frac{1}{M_s{}^2}\left[F_{\theta\theta}\left[\frac{F_{\phi\phi}}{\sin^2\theta} + \frac{\cos\theta}{\sin\theta}F_\theta\right] - \left[\frac{F_{\theta\phi}}{\sin\theta} - \frac{\cos\theta}{\sin\theta}\frac{F_\phi}{\sin\theta}\right]^2\right].$$ (A.1)

The polar coordinate system is shown in Fig.+A.1, which was chosen due to the symmetry of the system. The polar coordinates are:

$$x = \sin\theta\cos\phi$$ (A.2)
$$y = \sin\theta\sin\phi$$ (A.3)
$$z = \cos\theta$$ (A.4)

General Resonance Condition for a fcc Tetragonally Distorted System

Derivations

We will start with the derivation of the Gibbs free energy density for a fcc tetragonally distorted system F^{fct}. We list here all components of F^{fct}:[77,113,357]

1. Magnetocrystalline anisotropy in a fcc tetragonally distorted symmetry

$$F_{\text{tetragonal}} = K_{2\perp}\sin^2\theta - \frac{K_{4\perp}}{2}\cos^4\theta - \frac{K_{4\parallel}}{8}\sin^4\theta\left[3 + \cos\left(4\phi\right)\right] - K_{2\parallel}\sin^2\theta\cos^2(\phi - \phi_u)$$ (A.5)

2. Shape anisotropy

$$F_{\text{dipole}}^{\text{shape}} = 2\pi M_s^2\cos^2\theta$$ (A.6)

3. Zeeman term:

$$F_{\text{Zeeman}} = -\vec{M}\cdot\vec{H}_0 = -M_sH_0\left[\sin\theta\sin\theta_H\cos\left(\phi - \phi_H\right) + \cos\theta\cos\theta_H\right]$$ (A.7)

$$F^{\text{fct}} = F_{\text{Zeeman}} + F_{\text{uni}}^{\text{shape}} + F_{\text{uni}}^{\parallel} + F_{\text{tetragonal}}$$ (A.8)

The complete free energy density looks as follows

$$F^{\text{fct}} = -M_sH_0\left[\sin\theta\sin\theta_H\cos\left(\phi - \phi_H\right) + \cos\theta\cos\theta_H\right]$$
$$- \left(2\pi M_s^2 - K_{2\perp}\right)\sin^2\theta - K_{2\parallel}\sin^2\theta\cos^2\left(\phi - \phi_u\right) - \frac{K_{4\perp}}{2}\cos^4\theta - \frac{K_{4\parallel}}{8}\left[3 + \cos\left(4\phi\right)\right]\sin^4\theta$$ (A.9)

The parameter H_0 represents the applied field. This free energy density we have to differentiate with respect to θ and ϕ

1. First derivation with respect of θ

$$
\begin{aligned}
F_\theta^{\text{fct}} = \frac{\partial F^{\text{fct}}}{\partial \theta} = & - M_s H_0 \left[\cos\theta \sin\theta_H \cos(\phi - \phi_H) - \sin\theta \cos\theta_H \right] \\
& - 2 \left(2\pi M_s^2 - K_{2\perp} \right) \cos\theta \sin\theta \\
& - 2 K_{2\|} \cos\theta \sin\theta \cos^2(\phi - \phi_u) \\
& + 2 K_{4\perp} \cos^3\theta \sin\theta \\
& - \frac{K_{4\|}}{2} \left[3 + \cos(4\phi) \right] \sin^3\theta \cos\theta
\end{aligned}
\tag{A.10}
$$

2. Second derivation with respect of θ and we calculated $2(2\pi M_s^2 - K_{2\perp}) = (4\pi M_s^2 - 2K_{2\perp})$

$$
\begin{aligned}
F_{\theta\theta}^{\text{fct}} = \frac{\partial^2 F^{\text{fct}}}{\partial \theta^2} & - M_s H_0 \left[-\sin\theta \sin\theta_H \cos(\phi - \phi_H) - \cos\theta \cos\theta_H \right] \\
& + \left(4\pi M_s^2 - 2K_{2\perp} \right) \sin^2\theta - \left(4\pi M_s^2 - 2K_{2\perp} \right) \cos^2\theta \\
& + 2 K_{2\|} \cos^2(\phi - \phi_u) \sin^2\theta - 2 K_{2\|} \cos^2(\phi - \phi_u) \cos^2\theta \\
& + 2 K_{4\perp} \cos^4\theta - 6 K_{4\perp} \cos^2\theta \sin^2\theta \\
& + \frac{K_{4\|}}{2} \left[3 + \cos(4\phi) \right] \sin^4\theta - \frac{3 K_{4\|}}{2} \left[3 + \cos(4\phi) \right] \sin^2\theta \cos^2\theta
\end{aligned}
\tag{A.11}
$$

This equation has to be simplified by the following trigonometric theorems:

$$
\sin^2\theta - \cos^2\theta = \cos(2\theta)
\tag{A.12}
$$

$$
2\cos^4\theta - 6\cos^2\theta \sin^2\theta = \cos(2\theta) + \cos(4\theta)
\tag{A.13}
$$

$$
\frac{1}{2}\sin^4\theta - \frac{3}{2}\cos^2\theta \sin^2\theta = \frac{1}{4}\left[\cos(4\theta) - \cos(2\theta) \right]
\tag{A.14}
$$

So the substituted second derivation is:

$$
\begin{aligned}
F_{\theta\theta}^{\text{fct}} = \frac{\partial^2 F^{\text{fct}}}{\partial \theta^2} = & \ M_s H_0 \left[\sin\theta \sin\theta_H \cos(\phi - \phi_H) + \cos\theta \cos\theta_H \right] \\
& + \left(4\pi M_s^2 - 2K_{2\perp} \right) \cos(2\theta) \\
& + 2 K_{2\|} \cos^2(\phi - \phi_u) \cos(2\theta) \\
& + K_{4\perp} \left[\cos(2\theta) + \cos(4\theta) \right] \\
& + \frac{K_{4\|}}{4} \left[3 + \cos(4\phi) \right] \left[\cos(4\theta) - \cos(2\theta) \right]
\end{aligned}
\tag{A.15}
$$

This expression can now be splitted with respect to the corresponding angles.

$$
\begin{aligned}
F_{\theta\theta}^{\text{fct}} = \frac{\partial^2 F^{\text{fct}}}{\partial \theta^2} = & \ M_s H_0 \left[\sin\theta \sin\theta_H \cos(\phi - \phi_H) + \cos\theta \cos\theta_H \right] \\
& + \left[\left(4\pi M_s^2 - 2K_{2\perp} \right) + 2 K_{2\|} \cos^2(\phi - \phi_u) \right. \\
& \left. + K_{4\perp} - \frac{K_{4\|}}{4} \left[3 + \cos(4\phi) \right] \right] \cos(2\theta) \\
& + \left[K_{4\perp} + \frac{K_{4\|}}{4} \left[3 + \cos(4\phi) \right] \right] \cos(4\theta)
\end{aligned}
\tag{A.16}
$$

3. In a next step we have to calculate the mixed second derivation with respect of θ and ϕ

$$
\begin{aligned}
F_{\theta\phi}^{\text{fct}} = \frac{\partial^2 F^{\text{fct}}}{\partial \theta \partial \phi} = & \ M_s H_0 \left[\cos\theta \sin\theta_H \sin(\phi - \phi_H) \right] \\
& + 4 K_{2\|} \cos\theta \sin\theta \cos(\phi - \phi_u) \sin(\phi - \phi_u) \\
& + 2 K_{4\|} \sin^3\theta \cos\theta \cos(4\phi)
\end{aligned}
\tag{A.17}
$$

4. Now we calculate the first derivation with respect of ϕ

$$
\begin{aligned}
F_\phi^{\text{fct}} = \frac{\partial F^{\text{fct}}}{\partial \phi} = & \ M_s H_0 \left[\sin\theta \sin\theta_H \sin(\phi - \phi_H) \right] \\
& + 2 K_{2\|} \sin^2\theta \cos(\phi - \phi_u) \sin(\phi - \phi_u) \\
& + \frac{K_{4\|}}{2} \sin^4\theta \sin(4\phi)
\end{aligned}
\tag{A.18}
$$

To simplify this equation we use:

$$\cos\left(\phi-\phi_{\mathrm{u}}\right)\sin\left(\phi-\phi_{\mathrm{u}}\right)=\frac{1}{2}\sin\left[2\left(\phi-\phi_{\mathrm{u}}\right)\right] \tag{A.19}$$

So the resulting expression is:

$$\begin{aligned}
F_\phi^{\mathrm{fct}}=\frac{\partial F^{\mathrm{fct}}}{\partial\phi}= \; & M_{\mathrm{s}}H_0\left[\sin\theta\sin\theta_H\sin\left(\phi-\phi_H\right)\right] \\
& + K_{2\|}\sin^2\theta\sin\left[2\left(\phi-\phi_{\mathrm{u}}\right)\right] \\
& + \frac{K_{4\|}}{2}\sin^4\theta\sin\left(4\phi\right)
\end{aligned} \tag{A.20}$$

5. The last derivation we need is the second with respect of ϕ

$$\begin{aligned}
F_{\phi\phi}^{\mathrm{fct}}=\frac{\partial^2 F^{\mathrm{fct}}}{\partial\phi^2}= \; & M_{\mathrm{s}}H_0\left[\sin\theta\sin\theta_H\cos\left(\phi-\phi_H\right)\right] \\
& + 2K_{2\|}\sin^2\theta\cos\left[2\left(\phi-\phi_{\mathrm{u}}\right)\right] \\
& + 2K_{4\|}\sin^4\theta\cos\left(4\phi\right)
\end{aligned} \tag{A.21}$$

Evaluation

Now we apply (A.1). We will evaluate the general formula in steps.

1. Evaluation of the first term:

a) Calculating $\frac{F_{\phi\phi}^{\mathrm{fct}}}{\sin^2\theta}$

$$\begin{aligned}
\frac{F_{\phi\phi}^{\mathrm{fct}}}{\sin^2\theta}= \; & \\
= \; & M_{\mathrm{s}}H_0\left[\frac{1}{\sin\theta}\sin\theta_H\cos\left(\phi-\phi_H\right)\right] \\
& + 2K_{2\|}\cos\left[2\left(\phi-\phi_{\mathrm{u}}\right)\right] \\
& + 2K_{4\|}\sin^2\theta\cos\left(4\phi\right)
\end{aligned} \tag{A.22}$$

b) Calculating $\frac{\cos\theta}{\sin\theta}\cdot F_\theta^{\mathrm{fct}}$

$$\begin{aligned}
\frac{\cos\theta}{\sin\theta}\cdot F_\theta^{\mathrm{fct}}= \; & \\
& - M_{\mathrm{s}}H_0\left[-\frac{\cos^2\theta}{\sin\theta}\sin\theta_H\cos\left(\phi-\phi_H\right)-\cos\theta\cos\theta_H\right] \\
& - \left[4\pi M_{\mathrm{s}}{}^2-2K_{2\perp}\right]\cos^2\theta \\
& - 2K_{2\|}\cos^2\theta\cos^2\left(\phi-\phi_{\mathrm{u}}\right) \\
& + 2K_{4\perp}\cos^4\theta \\
& - \frac{1}{2}K_{4\|}\left[3+\cos\left(4\phi\right)\right]\sin^2\theta\cos^2\theta
\end{aligned} \tag{A.23}$$

c) Now we add term (A.22) and (A.23)

$$\begin{aligned}
\frac{F_{\phi\phi}^{\mathrm{fct}}}{\sin^2\theta}+\frac{\cos\theta}{\sin\theta}\cdot F_\theta^{\mathrm{fct}}= \; & \\
= \; & M_{\mathrm{s}}H_0\left[\frac{1}{\sin\theta}-\frac{\cos^2\theta}{\sin\theta}\sin\theta_H\sin\left(\phi-\phi_H\right)+\cos\theta\cos\theta_H\right] \\
& - \left[4\pi M_{\mathrm{s}}{}^2-2K_{2\perp}\right]\cos^2\theta \\
& + 2K_{2\|}\cos\left[2\left(\phi-\phi_{\mathrm{u}}\right)\right]-2K_{2\|}\cos^2\theta\cos^2\left(\phi-\phi_{\mathrm{u}}\right) \\
& + 2K_{4\perp}\cos^4\theta \\
& + 2K_{4\|}\sin^2\theta\cos\left(4\phi\right)-\frac{1}{2}K_{4\|}\left[3+\cos\left(4\phi\right)\right]\sin^2\theta\cos^2\theta
\end{aligned} \tag{A.24}$$

For a more accurate expression we substitute some terms

$$\frac{1}{\sin\theta}-\frac{\cos^2\theta}{\sin\theta}=\sin\theta \tag{A.25}$$

$$\sin^2\theta=1-\cos^2\theta \tag{A.26}$$

$$-2\cos\left(4\phi\right)-\frac{1}{2}\left[3+\cos\left(4\phi\right)\right]=-\frac{1}{2}\left[3+5\cos\left(4\phi\right)\right] \tag{A.27}$$

So we achieve the following expression:

$$\frac{F_{\phi\phi}^{\text{fct}}}{\sin^2\theta} + \frac{\cos\theta}{\sin\theta}\cdot F_\theta^{\text{fct}} =$$

$$= M_{\text{s}}H_0\left[\sin\theta\sin\theta_H\sin(\phi-\phi_H)+\cos\theta\cos\theta_H\right]$$
$$-\left(4\pi M_{\text{s}}^2-2K_{2\perp}\right)\cos^2\theta$$
$$+2K_{2\|}\cos\left[2\left(\phi-\phi_{\text{u}}\right)\right]$$
$$-2K_{2\|}\cos^2\theta\cos^2\left(\phi-\phi_{\text{u}}\right)$$
$$+2K_{4\perp}\cos^4\theta$$
$$+2K_{4\|}\cos(4\phi)$$
$$-\frac{K_{4\|}}{2}\left[3+5\cos(4\phi)\right]\cos^2\theta$$
$$+\frac{K_{4\|}}{2}\left[3+\cos(4\phi)\right]\cos^4\theta \tag{A.28}$$

In the last step we convert this term by ordering with respect of the θ-angles:

$$\frac{F_{\phi\phi}^{\text{fct}}}{\sin^2\theta} + \frac{\cos\theta}{\sin\theta}\cdot F_\theta^{\text{fct}} =$$

$$= M_{\text{s}}H_0\left[\sin\theta\sin\theta_H\sin(\phi-\phi_H)+\cos\theta\cos\theta_H\right]$$
$$+\left\{-\left(4\pi M_{\text{s}}^2-2K_{2\perp}\right)-2K_{2\|}\cos^2\left(\phi-\phi_{\text{u}}\right)\right.$$
$$\left.-\frac{K_{4\|}}{2}\left[3+5\cos(4\phi)\right]\right\}\cos^2\theta$$
$$+\left\{2K_{4\perp}+\frac{1}{2}K_{4\|}\left[3+\cos(4\phi)\right]\right\}\cos^4\theta$$
$$+\left\{2K_{2\|}\cos\left[2(\phi-\phi_{\text{u}})\right]+2K_{4\|}\cos(4\phi)\right\} \tag{A.29}$$

d) Now we multiply (A.16) and (A.29)

$$F_{\theta\theta}^{\text{fct}}\cdot\left[\frac{F_{\phi\phi}^{\text{fct}}}{\sin^2\theta}+\frac{\cos\theta}{\sin\theta}\cdot F_\theta^{\text{fct}}\right] = \left[M_{\text{s}}H_0\left[\sin\theta\sin\theta_H\cos(\phi-\phi_H)+\cos\theta\cos\theta_H\right]\right.$$

$$+\left(-\left(4\pi M_{\text{s}}^2-2K_{2\perp}\right)-2K_{2\|}\cos^2\left(\phi-\phi_{\text{u}}\right)\right.$$
$$\left.+K_{4\perp}-\frac{K_{4\|}}{4}\left[3+\cos(4\phi)\right]\right)\cos(2\theta)$$
$$\left.+\left(K_{4\perp}+\frac{K_{4\|}}{4}\left[3+\cos(4\phi)\right]\right)\cos(4\theta)\right]$$

$$\left[M_{\text{s}}H_0\left[\sin\theta\sin\theta_H\cos(\phi-\phi_H)+\cos\theta\cos\theta_H\right]\right.$$
$$+\left(-\left(4\pi M_{\text{s}}^2-2K_{2\perp}\right)-2K_{2\|}\cos^2\left(\phi-\phi_{\text{u}}\right)\right.$$
$$\left.-\frac{K_{4\|}}{2}\left[3+5\cos(4\phi)\right]\right)\cos^2\theta$$
$$+\left(2K_{4\perp}+\frac{K_{4\|}}{2}\left[3+\cos(4\phi)\right]\right)\cos^4\theta$$
$$\left.+\left(-2K_{2\|}\cos\left[2\left(\phi-\phi_{\text{u}}\right)\right]+2K_{4\|}\cos(4\phi)\right)\right] \tag{A.30}$$

2. In this part we calculating the second term

a) Evaluation of $\frac{F_{\theta\phi}^{\text{fct}}}{\sin\theta}$

$$\frac{F_{\theta\phi}^{\text{fct}}}{\sin\theta} =$$

$$M_{\text{s}}H_0\frac{\cos\theta}{\sin\theta}\sin\theta_H\cos(\phi-\phi_H)$$
$$+2K_{4\|}\cos\theta\sin^2\theta\sin(4\phi)$$
$$+2K_{2\|}\cos\theta\sin\left[2\left(\phi-\phi_{\text{u}}\right)\right] \tag{A.31}$$

b) Evaluation of $\frac{\cos\theta}{\sin\theta}\frac{F_\phi^{\text{fct}}}{\sin\theta}$

$$\frac{\cos\theta}{\sin\theta}\frac{F_\theta^{\text{fct}}}{\sin\theta} =$$

$$M_{\text{s}}H_0\frac{\cos\theta}{\sin\theta}\sin\theta_H\cos\left(\phi-\phi_H\right)$$

$$+\frac{K_{4\parallel}}{2}\cos\theta\sin^2\theta\sin\left(4\phi\right)$$

$$+K_{2\parallel}\cos\theta\sin\left[2\left(\phi-\phi_{\text{u}}\right)\right] \tag{A.32}$$

c) We square the term of formula (A.31) minus (A.32)

$$\left[\frac{F_{\theta\phi}^{\text{fct}}}{\sin\theta}-\frac{\cos\theta}{\sin\theta}\frac{F_\theta^{\text{fct}}}{\sin\theta}\right]^2 = \left[\frac{3K_{4\parallel}}{2}\sin^2\theta\sin\left(4\phi\right)+K_{2\parallel}\sin\left[2\left(\phi-\phi_{\text{u}}\right)\right]\right]^2\cos^2\theta \tag{A.33}$$

3. In the last step we subtract (A.33) from (A.30) and divide by M_{s}. Then we substitute

$$\left(4\pi M_{\text{s}}-\frac{2K_{2\perp}}{M_{\text{s}}}\right)=4\pi M_{\text{eff}} \tag{A.34}$$

$$\left(\frac{\omega}{\gamma}\right)^2 = \left\{\left(H_0\left[\sin\theta\sin\theta_H\cos\left(\phi-\phi_H\right)+\cos\theta\cos\theta_H\right]\right)\right.$$

$$+\left(-4\pi M_{\text{eff}}-\frac{2K_{2\parallel}}{M_s}\cos^2\left(\phi-\phi_{\text{u}}\right)+\frac{K_{4\perp}}{M_{\text{s}}}-\frac{K_{4\parallel}}{4M_{\text{s}}}\left[3+\cos\left(4\phi\right)\right]\right)\cos\left(2\theta\right)$$

$$+\left.\left(\frac{K_{4\perp}}{M_{\text{s}}}+\frac{K_{4\parallel}}{4M_{\text{s}}}\left[3+\cos\left(4\phi\right)\right]\right)\cos\left(4\theta\right)\right\}$$

$$\cdot\left\{\left(H_0\left[\sin\theta\sin\theta_H\cos\left(\phi-\phi_H\right)+\cos\theta\cos\theta_H\right]\right)\right.$$

$$+\left(-4\pi M_{\text{eff}}-\frac{2K_{2\parallel}}{M_{\text{s}}}\cos^2\left(\phi-\phi_{\text{u}}\right)-\frac{K_{4\parallel}}{2M_{\text{s}}}\left[3+5\cos\left(4\phi\right)\right]\right)\cos^2\theta$$

$$+\left(\frac{2K_{4\perp}}{M_{\text{s}}}+\frac{K_{4\parallel}}{2M_{\text{s}}}\left[3+\cos\left(4\phi\right)\right]\right)\cos^4\theta$$

$$+\left.\left(\frac{2K_{2\parallel}}{M_{\text{s}}}\cos\left[2\left(\phi-\phi_{\text{u}}\right)\right]+\frac{2K_{4\parallel}}{M_{\text{s}}}\cos\left(4\phi\right)\right)\right\}$$

$$-\left\{\left[\frac{K_{2\parallel}}{M_{\text{s}}}\sin\left[2\left(\phi-\phi_{\text{u}}\right)\right]+\frac{3K_{4\parallel}}{2M_{\text{s}}}\sin^2\theta\sin\left(4\phi\right)\right]^2\cos^2\theta\right\} \tag{A.35}$$

General Resonance Condition for hcp-Structures

First all components of the free energy density are derived and subsequenty, the achieved contributions are evaluated. . Firs F^{hcp} is summarised:

1.

$$F_{\text{hex}} = K_{2\perp} \sin^2 \theta + K_{4\perp} \sin^4 \theta + K_{6\perp} \sin^6 \theta + K_{6\parallel} \sin^6 \theta \cos^6 \phi \tag{A.36}$$

This equation has been taken from [358]. There exists a second definition of F_{hex} which is introduced in [77] which is shown below. In this chapter the derivation of equation (A.37) will be calculated.

$$F_{\text{hex}} = K_{2\perp} \sin^2 \theta + K_{4\perp} \sin^4 \theta + K_{6\perp} \sin^6 \theta + K_{6\parallel} \sin^6 \theta \sin(6\phi) \tag{A.37}$$

2.

$$F_{\text{uni}}^{\text{shape}} = 2\pi M_s^2 \left(N_\perp - N_\parallel \right) \cos^2 \theta \tag{A.38}$$

In this equation we have two new parameters. $N_\perp$ and $N_\parallel$ which represents the demagnetization factors in the out-of-plane and inplane direction. Furthermore one has to substitute $\cos^2 \theta$ by $1 - \sin^2 \theta$ and neglect the angle independent term. So this evaluation leads to

$$F_{\text{uni}}^{\text{shape}} = -2\pi M_s^2 \left(N_\perp - N_\parallel \right) \sin^2 \theta \tag{A.39}$$

3.

$$F_{\text{uni}}^\perp = K_{2\perp} \sin^2 \theta \tag{A.40}$$

4.

$$F_{\text{uni}}^\parallel = K_{2\parallel} \sin^2 \theta \cos^2(\phi - \phi_{\text{u}}) \tag{A.41}$$

5.

$$F_{\text{Zeeman}} = -M_s H_0 \left(\sin \theta \sin \theta_H \cos \left(\phi - \phi_H \right) + \cos \theta \cos \theta_H \right) \tag{A.42}$$

Now we summarize the following formulas: (A.36), (A.39), (A.40), (A.41) and (A.42):

$$F^{\text{hcp}} = F_{\text{Zeeman}} + F_{\text{uni}}^{\text{shape}} + F_{\text{uni}}^\parallel + F_{\text{hexagonal}} \tag{A.43}$$

Here we neglect the component (A.40) because it is included in term (A.38).

$$\begin{aligned} F^{\text{hcp}} = &- M_s H_0 \left(\sin \theta \sin \theta_H \cos \left(\phi - \phi_H \right) + \cos \theta \cos \theta_H \right) \\ &- 2\pi M_s^2 \left(N_\perp - N_\parallel \right) \sin^2 \theta \\ &- K_{2\parallel} \sin^2 \theta \cos^2 \left(\phi - \phi_{\text{u}} \right) \\ &+ K_{2\perp} \sin^2 \theta + K_{4\perp} \sin^4 \theta + \left[K_{6\perp} + K_{6\parallel} \sin \left(6\phi \right) \right] \sin^6 \theta \end{aligned} \tag{A.44}$$

This expression can be simplified by ordering the terms in order of $\sin^n \theta$

$$\begin{aligned} F^{\text{hcp}} = &- M_s H_0 \left[\sin \theta \sin \theta_H \cos \left(\phi - \phi_H \right) + \cos \theta \cos \theta_H \right] \\ &- \left[\left(2\pi M_s^2 \left(N_\perp - N_\parallel \right) - K_{2\perp} \right) + K_{2\parallel} \cos^2 (\phi - \phi_{\text{u}}) \right] \sin^2 \theta \\ &+ K_{4\perp} \sin^4 \theta \\ &+ \left[K_{6\perp} + K_{6\parallel} \sin \left(6\phi \right) \right] \sin^6 \theta \end{aligned} \tag{A.45}$$

Derivations

In the following enumeration we will derive expression (A.45) with respect to the polar and azimuth angle to achieve the components for the above mentioned formula derived by Baselgia (see equation (A.1)).

1. First derivation with respect of θ

$$\begin{aligned} F_\theta^{\text{hcp}} = &\frac{\partial F^{\text{hcp}}}{\partial \theta} \\ &- M_s H_0 \left[\cos \theta \sin \theta_H \cos \left(\phi - \phi_H \right) - \sin \theta \cos \theta_H \right] \\ &- \left[\left(2\pi M_s^2 \left(N_\perp - N_\parallel \right) - K_{2\perp} \right) + K_{2\parallel} \cos^2 (\phi - \phi_{\text{u}}) \right] 2 \cos \theta \sin \theta \\ &+ K_{4\perp} 4 \cos \theta \sin^3 \theta \\ &+ \left[K_{6\perp} + K_{6\parallel} \sin \left(6\phi \right) \right] 6 \cos \theta \sin^5 \theta \end{aligned} \tag{A.46}$$

We only multiply the constants, and achieve

$$
\begin{aligned}
F_\theta^{\text{hcp}} = \frac{\partial F^{\text{hcp}}}{\partial \theta} & \\
& - M_{\text{s}} H_0 \left[\cos\theta \sin\theta_H \cos(\phi - \phi_H) - \sin\theta \cos\theta_H \right] \\
& - \left[\left(4\pi M_{\text{s}}^2 \left(N_\perp - N_\parallel \right) - 2K_{2\perp} \right) + 2K_{2\parallel} \cos^2(\phi - \phi_{\text{u}}) \right] \cos\theta \sin\theta \\
& + 4K_{4\perp} \cos\theta \sin^3\theta \\
& + 6 \left[K_{6\perp} + K_{6\parallel} \sin(6\phi) \right] \cos\theta \sin^5\theta
\end{aligned} \tag{A.47}
$$

2. Second derivation with respect of θ

$$
\begin{aligned}
F_{\theta\theta}^{\text{hcp}} = \frac{\partial^2 F^{\text{hcp}}}{\partial \theta^2} & \\
& - M_{\text{s}} H_0 \left[-\sin\theta \sin\theta_H \cos(\phi - \phi_H) - \cos\theta \cos\theta_H \right] \\
& - \left[\left(4\pi M_{\text{s}}^2 \left(N_\perp - N_\parallel \right) - 2K_{2\perp} \right) + 2K_{2\parallel} \cos^2(\phi - \phi_{\text{u}}) \right] \left(\cos^2\theta -^2 \sin\theta \right) \\
& + 4K_{4\perp} \left(3\cos^2\theta \sin^2\theta - \sin^4\theta \right) \\
& + 6 \left[K_{6\perp} + K_{6\parallel} \sin(6\phi) \right] \left(5\cos^2\theta \sin^4\theta - \sin^6\theta \right)
\end{aligned} \tag{A.48}
$$

This can be simplified by

$$
\cos^2\theta - \sin^2\theta = \cos(2\theta) \tag{A.49}
$$

$$
3\cos^2\theta \sin^2\theta - \sin^4\theta = \frac{1}{2} \left(\cos(2\theta) - \cos(4\theta) \right) \tag{A.50}
$$

$$
5\cos^2\theta \sin^4\theta - \sin^6\theta = \frac{1}{16} \left(5\cos(2\theta) - 8\cos(4\theta) + 3\cos(6\theta) \right) \tag{A.51}
$$

By ordering the $\cos n\theta$ terms the second derivative becomes the following expression

$$
\begin{aligned}
F_{\theta\theta}^{\text{hcp}} = \frac{\partial^2 F^{\text{hcp}}}{\partial \theta^2} & \\
& M_{\text{s}} H_0 \left[\sin\theta \sin\theta_H \cos(\phi - \phi_H) + \cos\theta \cos\theta_H \right] \\
& - \Bigg[\left(4\pi M_{\text{s}}^2 \left(N_\perp - N_\parallel \right) - 2K_{2\perp} \right) \\
& \quad + 2K_{2\parallel} \cos^2(\phi - \phi_{\text{u}}) - 2K_{4\perp} - \frac{15}{8} \left[K_{6\perp} + K_{6\parallel} \sin(6\phi) \right] \Bigg] \cos 2\theta \\
& + \left[2K_{4\perp} - 3 \left[K_{6\perp} + K_{6\parallel} \sin(6\phi) \right] \right] \cos(4\theta) \\
& + \left[\frac{9}{8} \left[K_{6\perp} + K_{6\parallel} \sin(6\phi) \right] \right] \cos(6\theta) \Bigg]
\end{aligned} \tag{A.52}
$$

3. First derivation with respect of ϕ

$$
\begin{aligned}
F_\phi^{\text{hcp}} = \frac{\partial F^{\text{hcp}}}{\partial \phi} = & \\
& + M_{\text{s}} H_0 \left[\sin\theta \sin\theta_H \sin(\phi - \phi_H) \right] \\
& + 2K_{2\parallel} \sin(\phi - \phi_{\text{u}}) \cos(\phi - \phi_{\text{u}}) \sin^2\theta \\
& + 6K_{6\parallel} \cos(6\phi) \sin^6\theta
\end{aligned} \tag{A.53}
$$

The simplification of this expression this takes place in the evaluation of the resonance condition.

4. Second derivation with respect of ϕ This expression can be simplified by $-\sin^2(\phi - \phi_{\text{u}}) + \cos(\phi - \phi_{\text{u}}) = \cos\left[2(\phi - \phi_{\text{u}}) \right]$

$$
\begin{aligned}
F_{\phi\phi}^{\text{hcp}} = \frac{\partial^2 F^{\text{hcp}}}{\partial \phi^2} = & \\
& + M_{\text{s}} H_0 \left[\sin\theta \sin\theta_H \cos(\phi - \phi_H) \right] \\
& + 4K_{2\parallel} \cos\left[2(\phi - \phi_{\text{u}}) \right] \sin^2\theta \\
& - 36K_{6\parallel} \sin(6\phi) \sin^6\theta
\end{aligned} \tag{A.54}
$$

At least we calculate the mixed derivation with respect to θ and then to ϕ

5. Mixed derivation with respect of θ and ϕ

$$F_{\theta\phi}^{\mathrm{hcp}} = \frac{\partial^2 F^{\mathrm{hcp}}}{\partial\theta\partial\phi} =$$
$$= M_{\mathrm{s}}H_0 \left[\cos\theta \sin\theta_H \sin\left(\phi - \phi_H\right) \right]$$
$$- 2K_{2\parallel} \cos\left(\phi - \phi_{\mathrm{u}}\right) \sin\left(\phi - \phi_{\mathrm{u}}\right) \cos\theta \sin\theta$$
$$+ 36K_{6\parallel} \cos(6\phi) \cos\theta \sin^5\theta \tag{A.55}$$

Evaluation

Here in this section we are calculating the resonance condition as shown in **A**. We do this in steps, so it is more obvious how the derivation was done. The part of $F_{\theta\theta}^{\mathrm{hcp}}$ has been derived in section **A**. Now we have to calculate only the first and the second bracket of the Baselgia formula:

1. The first bracket of (**A.1**)

$$\left[\frac{F_{\phi\phi}^{\mathrm{hcp}}}{\sin^2\theta} + \frac{\cos\theta}{\sin\theta} \cdot F_{\theta}^{\mathrm{hcp}} \right] \tag{A.56}$$

We split this term into two expressions

a)

$$\frac{F_{\phi\phi}^{\mathrm{hcp}}}{\sin^2\theta} =$$
$$+ M_{\mathrm{s}}H_0 \left[\frac{1}{\sin\theta} \sin\theta_H \cos\left(\phi - \phi_H\right) \right]$$
$$+ 2K_{2\parallel} \cos\left[2\left(\phi - \phi_{\mathrm{u}}\right)\right]$$
$$- 36K_{6\parallel} \sin\left(6\phi\right) \sin^4\theta \tag{A.57}$$

b)

$$\frac{\cos\theta}{\sin\theta} \cdot F_{\theta}^{\mathrm{hcp}} =$$
$$- M_{\mathrm{s}}H_0 \left[\frac{\cos^2\theta}{\sin\theta} \sin\theta_H \cos\left(\phi - \phi_H\right) - \cos\theta \cos\theta_H \right]$$
$$- \left[\left(4\pi M_{\mathrm{s}}^2 \left(N_\perp - N_\parallel\right) - 2K_{2\perp}\right) + 2K_{2\parallel} \cos^2\left(\phi - \phi_{\mathrm{u}}\right) \right] \cos^2\theta$$
$$+ 4K_{4\perp} \cos^2\theta \sin^2\theta$$
$$+ 6 \left[K_{6\perp} + K_{6\parallel} \sin(6\phi) \right] \cos^2\theta \sin^4\theta \tag{A.58}$$

c) We now summarize (**A.57**) and (**A.58**) to achieve the second bracket expression.

$$\left[\frac{F_{\phi\phi}^{\mathrm{hcp}}}{\sin^2\theta} + \frac{\cos\theta}{\sin\theta} \cdot F_{\theta}^{\mathrm{hcp}} \right] =$$
$$+ M_{\mathrm{s}}H_0 \left[\frac{1}{\sin\theta} \sin\theta_H \cos\left(\phi - \phi_H\right) \right]$$
$$- M_{\mathrm{s}}H_0 \left[\frac{\cos^2\theta}{\sin\theta} \sin\theta_H \cos\left(\phi - \phi_H\right) - \cos\theta \cos\theta_H \right]$$
$$- \left[\left(4\pi M_{\mathrm{s}}^2 \left(N_\perp - N_\parallel\right) - 2K_{2\perp}\right) + 2K_{2\parallel} \cos^2\left(\phi - \phi_{\mathrm{u}}\right) \right] \cos^2\theta$$
$$+ 2K_{2\parallel} \cos\left[2\left(\phi - \phi_{\mathrm{u}}\right)\right]$$
$$+ 4K_{4\perp} \cos^2\theta \sin^2\theta$$
$$- 36K_{6\parallel} \sin\left(6\phi\right) \sin^4\theta$$
$$+ 6 \left[K_{6\perp} + K_{6\parallel} \sin(6\phi) \right] \cos^2\theta \sin^4\theta \tag{A.59}$$

There is one substitution we apply

$$\frac{1}{\sin\theta} - \frac{\cos^2\theta}{\sin\theta} = \sin\theta \tag{A.60}$$

Now one has to order the terms by $cos^2\theta$

$$\left[\frac{F_{\phi\phi}^{\mathrm{hcp}}}{\sin^2\theta} + \frac{\cos\theta}{\sin\theta}\cdot F_{\theta}^{\mathrm{hcp}}\right] =$$

$$+ M_{\mathrm{s}}H_0\left[\sin\theta\sin\theta_H\cos\left(\phi-\phi_H\right) + \cos\theta\cos\theta_H\right]$$

$$+ \left[-\left(4\pi M_{\mathrm{s}}^2\left(N_\perp - N_\|\right) - 2K_{2\perp}\right) - 2K_{2\|}\cos^2\left(\phi-\phi_{\mathrm{u}}\right)\right.$$

$$+ 4K_{4\perp}\sin^2\theta + 6\left[K_{6\perp} - K_{6\|}\sin\left(6\phi\right)\right]\sin^4\theta\right]\cos^2\theta$$

$$+ \left[2K_{2\|}\cos\left[2\left(\phi-\phi_{\mathrm{u}}\right)\right] - 36K_{6\|}\sin\left(6\phi\right)\sin^4\theta\right] \tag{A.61}$$

2. The second bracket of (**A.1**)

$$\left[\frac{F_{\theta\phi}^{\mathrm{hcp}}}{\sin\theta} - \frac{\cos\theta}{\sin\theta}\frac{F_{\phi}^{\mathrm{hcp}}}{\sin\theta}\right]^2 \tag{A.62}$$

Even here we are calculating the bracket in two steps

a)

$$\frac{F_{\theta\phi}^{\mathrm{hcp}}}{\sin\theta} =$$

$$= M_{\mathrm{s}}H_0\left[\frac{\cos\theta}{\sin\theta}\sin\theta_H\sin\left(\phi-\phi_H\right)\right]$$

$$- 2K_{2\|}\cos\left(\phi-\phi_{\mathrm{u}}\right)\sin\left(\phi-\phi_{\mathrm{u}}\right)\cos\theta$$

$$+ 36K_{6\|}\cos(6\phi)\cos\theta\sin^4\theta \tag{A.63}$$

We substitute here $\cos\left(\phi-\phi_{\mathrm{u}}\right)\sin\left(\phi-\phi_{\mathrm{u}}\right)$ by $\frac{1}{2}\sin\left[2\left(\phi-\phi_{\mathrm{u}}\right)\right]$ and get

$$\frac{F_{\theta\phi}^{\mathrm{hcp}}}{\sin\theta} =$$

$$= M_{\mathrm{s}}H_0\left[\frac{\cos\theta}{\sin\theta}\sin\theta_H\sin\left(\phi-\phi_H\right)\right]$$

$$- K_{2\|}\sin\left[2\left(\phi-\phi_{\mathrm{u}}\right)\right]\cos\theta$$

$$+ 36K_{6\|}\cos(6\phi)\cos\theta\sin^4\theta \tag{A.64}$$

b)

$$\frac{\cos\theta}{\sin\theta}\frac{F_{\phi}^{\mathrm{hcp}}}{\sin\theta} =$$

$$= M_{\mathrm{s}}H_0\left[\frac{\cos\theta}{\sin\theta}\sin\theta_H\sin\left(\phi-\phi_H\right)\right]$$

$$- 2K_{2\|}\cos\left(\phi-\phi_{\mathrm{u}}\right)\sin\left(\phi-\phi_{\mathrm{u}}\right)\cos\theta$$

$$+ 6K_{6\|}\cos(6\phi)\cos\theta\sin^4\theta \tag{A.65}$$

We apply the same substitution as in (**A.64**)

$$\frac{\cos\theta}{\sin\theta}\frac{F_{\phi}^{\mathrm{hcp}}}{\sin\theta} =$$

$$= M_{\mathrm{s}}H_0\left[\frac{\cos\theta}{\sin\theta}\sin\theta_H\sin\left(\phi-\phi_H\right)\right]$$

$$- K_{2\|}\sin\left[2\left(\phi-\phi_{\mathrm{u}}\right)\right]\cos\theta$$

$$+ 6K_{6\|}\cos(6\phi)\cos\theta\sin^4\theta \tag{A.66}$$

c) We now summarize (**A.64**) and (**A.66**) to achieve the second bracket expression.

$$\left[\frac{F_{\theta\phi}^{\mathrm{hcp}}}{\sin\theta} - \frac{\cos\theta}{\sin\theta}\frac{F_{\phi}^{\mathrm{hcp}}}{\sin\theta}\right]^2 = \left[-K_{2\|}\sin\left[2\left(\phi-\phi_u\right)\right] + 30K_{6\|}\cos(6\phi)\sin^4\theta\right]^2\cos^2\theta \tag{A.67}$$

3. In the last step we subtract equation (A.33) from (A.30) and divide by M_s. Then we substitute

$$\left(4\pi M_\mathrm{s} \left(N_\perp - N_\parallel \right) - \frac{2K_{2\perp}}{M_\mathrm{s}} \right) = 4\pi M_\mathrm{eff} \tag{A.68}$$

$$\left(\frac{\omega}{\gamma} \right)^2 =$$

$$= \left\{ H_0 \left[\sin\theta \sin\theta_H \cos\left(\phi - \phi_H\right) + \cos\theta \cos\theta_H \right] \right.$$

$$- \left[4\pi M_\mathrm{eff} + \frac{2K_{2\parallel}}{M_\mathrm{s}} \cos^2(\phi - \phi_\mathrm{u}) - \frac{2K_{4\perp}}{M_\mathrm{s}} - \frac{15}{8} \left(\frac{K_{6\perp}}{M_\mathrm{s}} + \frac{K_{6\parallel}}{M_\mathrm{s}} \sin\left(6\phi\right) \right) \right] \cos 2\theta$$

$$+ \left[\frac{2K_{4\perp}}{M_\mathrm{s}} - 3 \left(\frac{K_{6\perp}}{M_\mathrm{s}} + \frac{K_{6\parallel}}{M_\mathrm{s}} \sin\left(6\phi\right) \right) \right] \cos(4\theta)$$

$$+ \left[\frac{9}{8} \left(\frac{K_{6\perp}}{M_\mathrm{s}} + \frac{K_{6\parallel}}{M_\mathrm{s}} \sin\left(6\phi\right) \right) \right] \cos(6\theta) \right\}$$

$$\cdot \left\{ H_0 \left[\sin\theta \sin\theta_H \cos\left(\phi - \phi_H\right) + \cos\theta \cos\theta_H \right] \right.$$

$$+ \left[4\pi M_\mathrm{eff} - \frac{2K_{2\parallel}}{M_\mathrm{s}} \cos^2\left(\phi - \phi_\mathrm{u}\right) + \frac{4K_{4\perp}}{M_s} \sin^2\theta + 6 \left[\frac{K_{6\perp}}{M_\mathrm{s}} - \frac{K_{6\parallel}}{M_\mathrm{s}} \sin\left(6\phi\right) \right] \sin^4\theta \right] \cos^2\theta$$

$$+ \left[\frac{2K_{2\parallel}}{M_\mathrm{s}} \cos\left[2\left(\phi - \phi_\mathrm{u}\right)\right] - \frac{36K_{6\parallel}}{M_\mathrm{s}} \sin\left(6\phi\right) \sin^4\theta \right] \right\}$$

$$- \left\{ \left[-\frac{K_{2\parallel}}{M_\mathrm{s}} \sin\left[2\left(\phi - \phi_\mathrm{u}\right)\right] + \frac{30K_{6\parallel}}{M_\mathrm{s}} \cos(6\phi) \sin^4\theta \right]^2 \cos^2\theta \right\} \tag{A.69}$$

Chapter B.

Input Script File for an OOMMF Simulation

Here, the original code for the initial OOMMF script is shown. This script is initialising a simulation for a nanocone with 30 nm diameter and height, as well. The chosen box dimension is $2 \times 2 \times 2 \, \text{nm}^3$. The results for all generated simulations are summarised in the last paragraph of the experimental investigations on Cr (5 nm)/Py (20 nm)/Cr (3 nm) deposited on GaSb nanocones [see section 3.1].

```
# MIF 2.1
# simulation for a 30nm cone 20nm Py on top
# applied field out-of-plane (0.5T)
set PI [expr {4*atan(1.)}]
set MU0 [expr {4*$PI*1e-7}]
proc Cone { Ms x y z } {
    set xrad [expr {2.*$x - 1.}]
    set yrad [expr {2.*$y - 1.}]
    set dist [expr {$xrad*$xrad+$yrad*$yrad}]
    set hoehe_1 [expr {0.394736842105263-sqrt($dist)}]
    set hoehe_2 [expr {1.-sqrt($dist)}]
    if {$z>$hoehe_2} {return 0}
    if {$z<$hoehe_1} {return 0}
    return $Ms}
Specify Oxs_BoxAtlas:atlas{
    xrange {0 76.0E-9}
    yrange {0 76.0E-9}
    zrange {0 76.0E-9}}
Specify Oxs_RectangularMesh:mesh{
    cellsize {2.0e-9 2.0e-9 2.0e-9}
    atlas :atlas}
Specify Oxs_UniformExchange{
A 13E-12}
Specify Oxs_CubicAnisotropy{
  K1  0.
  axis1 {1 0 0}
  axis2 {0 1 0}}
Specify Oxs_Demag{}
Specify Oxs_UZeeman[subst{
comment {Field values in Tesla; scale to A/m}
multiplier [expr {1/$MU0}]
Hrange{
{0.0 0.0 -0.5 0.0 0.0 0.5 100}
{0.0 0.0 0.5 0.0 0.0 -0.5 100}}}]
# x y z Start - x y z End - step numbers +1
Specify Oxs_RungeKuttaEvolve:evolver {
do_precess 1
gamma_LL 2.21e5
alpha 0.5}
Specify Oxs_TimeDriver{
basename TestCone
vector_field_output_format {text %.15g}
scalar_output_format %.15g
evolver :evolver
mesh :mesh
stopping_dm_dt 0.24
Ms { Oxs_ScriptScalarField { atlas :atlas script {Cone 860E3}}}
m0 { Oxs_RandomVectorField { min_norm 1 max_norm 1 }}}
```

Chapter C.

Physical Constants and Units

Physical Constants

Tab. C.1.: Table of physical constants taken from 2010 CODATA recommended values.

Name of constant	Symbol	Value
Planck constant	h	$6.62606957(29) \cdot 10^{-34}$ J ·s
Speed of light (vacuum)	$c_0 = \frac{1}{\sqrt{\mu_o \varepsilon_0}}$	$2.99792458 \cdot 10^8$ m·s^{-1}
Magnetic constant (vacuum permeability)	μ_0	$4\pi \cdot 10^{-7}$ N·A^{-2}
Elementary charge	e_0	$1.602176565(35) \cdot 10^{-19}$ C
Electron rest mass	m_{e}	$9.10938291(40) \cdot 10^{-31}$ kg
Electron g-factor	g_e	$-2.00231930436153(53)$
Magnetic moment of an electron	μ_{e}	$-9.28476430(21) \cdot 10^{-24}$ J·T^{-1}
Electron gyromagnetic ratio	γ	$1.760859708(39) \cdot 10^{-11}$ s^{-1}T^{-1}
Electric constant (vacuum permittivity)	$\varepsilon_0 = \frac{1}{\mu_0 c_0^2}$	8.854187817 F·m^{-1}
Reduced Planck constant	$\hbar = \frac{h}{2\pi}$	$1.054571726(47) \cdot 10^{-34}$ J ·s
Bohr magneton	$\mu_{\mathrm{B}} = \frac{e\hbar}{2m_{\mathrm{e}}}$	$9.27400968(20) \cdot 10^{-24}$ J·T^{-1}

Units

Here, important relations of the conversion of the cgs- into SI - units are listed.[67]
Oersted - Tesla - Gauß: $\mu_0 \cdot 1 \text{ Oe} = 4\pi \times 10^{-7} \frac{\text{V s}}{\text{A m}} \frac{1000}{4\pi} \frac{\text{A}}{\text{m}} = 10^{-4}$ T = 1 Gauss (G)
emu/cm^3 - Gauss: $4\pi \cdot$emu/cm^3=1 G.
Conversion relations for the cgs- and SI units (electrodynamics):

$$\text{magnetic field strength: } \vec{H_{\mathrm{cgs}}} = \sqrt{4\pi\mu_o}\vec{H}_{\mathrm{SI}}$$

$$\text{magnetic flux density: } \vec{B}_{\mathrm{cgs}} = \sqrt{4\pi/\mu_o}\vec{B}_{\mathrm{SI}}$$

$$\text{current density: } \vec{j}_{\mathrm{cgs}} = \frac{\vec{j}_{\mathrm{SI}}}{\sqrt{4\pi/\mu_0}} \tag{C.1}$$

Therefore, arising from (**C.1**) the material parameter magnetization $\vec{M}$ can be written as follows:

$$\vec{H}_{\mathrm{cgs}} = \vec{B}_{\mathrm{cgs}} - 4\pi\vec{M}_{\mathrm{cgs}} \quad \rightleftarrows \quad \vec{H}_{\mathrm{SI}} = \frac{1}{\mu_0}\vec{B}_{\mathrm{SI}} - \vec{M}_{\mathrm{SI}} \tag{C.2}$$

Further units and conversion information can be found elsewhere.[69,359]

Ion Sputter Units

fluence $\widehat{=} \frac{ions}{cm^2}$
flux $\widehat{=} \frac{ions}{cm^2\,s}$

Bibliography

[1] G. Hu, T. Thomson, M. Albrecht, M. E. Best, B. D. Terris, C. T. Rettner, S. Raoux, G. M. McClelland, and M. W. Hart, "Magnetic and recording properties of Co/Pd islands on prepatterned substrates", J. Appl. Phys. **95**, 7013 (2004).

[2] J. Fassbender, T. Strache, M. O. Liedke, D. Marko, S. Wintz, K. Lenz, A. Keller, S. Facsko, I. Monch, and J. McCord, "Introducing artificial length scales to tailor magnetic properties", New J. Phys. **11**, 125002 (2009).

[3] M. Körner, K. Lenz, M. O. Liedke, T. Strache, A. Mücklich, A. Keller, S. Facsko, and J. Fassbender, "Interlayer exchange coupling of Fe/Cr/Fe thin films on rippled substrates", Phys. Rev. B **80**, 214401 (2009).

[4] S. N. Piramanayagam, "Perpendicular recording media for hard disk drives", J. Appl. Phys. **102**, 011301 (2007).

[5] R. Wood, Y. Sonobe, Z. Jin, and B. Wilson, "Perpendicular recording: the promise and the problems", J. Magn. Magn. Mater. **235**, 1 (2001).

[6] J. W. Park, Y. K. Kim, T. H. Lee, H.-S. Oh, and B.-K. Lee, "Optimization of Ru intermediate layer in CoCr-based perpendicular magnetic recording media", Phys. Stat. Sol. A **201**, 1763 (2004).

[7] R. Mukai, T. Uzumaki, and A. Tanaka, "Signal-to-media-noise ratio improvement of CoCrPt-SiO$_2$ granular perpendicular media by stacked Ru underlayer", J. Appl. Phys., 49th Annual Conference on Magnetism and Magnetic Materials **97**, 10N119 (2005).

[8] R. Mukai, T. Uzumaki, and A. Tanaka, "Microstructure improvement of thin Ru underlayer for CoCrPt-SiO$_2$ granular perpendicular media", IEEE Trans. Magn. **41**, 3169 (2005).

[9] J. Z. Shi, S. N. Piramanayagam, C. S. Mah, H. B. Zhao, J. M. Zhao, Y. S. Kay, and C. K. Pock, "Influence of dual-Ru intermediate layers on magnetic properties and recording performance of CoCrPt–SiO$_2$ perpendicular recording media", Appl. Phys. Lett. **87**, 222503 (2005).

[10] S. H. Park, S. O. Kim, T. D. Lee, H. S. Oh, Y. S. Kim, N. Y. Park, and D. H. Hong, "Effect of top Ru deposition pressure on magnetic and microstructural properties of CoCrPt–SiO$_2$ media in two-step Ru layer", Phys. Stat. Sol. A **8**, 1763 (2006).

[11] J. Z. Shi, S. N. Piramanayagam, C. S. Mah, and J. M. Zhao, "Influence of gas pressures on the magnetic properties and recording performance of CoCrPt-SiO$_2$ perpendicular media", J. Magn. Magn. Mater. **303**, e145 (2006).

[12] R. Mukai, T. Uzumaki, and A. Tanaka. "Formation of Grain- Isolated Co$_{80}$Pt$_{20}$ Magnetic Films for Granular-Type Perpendicular Media. In *Magnetics Conference, 2006. INTERMAG 2006. IEEE International*, page 12 (2006).

[13] S. N. Piramanayagam, H. B. Zhao, J. Z. Shi, and C. S. Mah, "Advanced perpendicular recording media structure with a magnetic intermediate layer", Appl. Phys. Lett. **88**, 092501 (2006).

[14] G. Chiarotti. "1.6 Crystal structures and bulk lattice parameters of materials quoted in the volume. In G. Chiarotti, editor, *Landolt-Börnstein - Group III Condensed Matter*, volume 24c: Interaction of Charged Particles and Atoms with Surfaces of *Landolt-Börnstein, New Series - Group III Condensed Matter: Numerical Data and Functional Relationships in Science and Technology*, chapter Interaction of Charged Particles and Atoms with Surfaces, pages 21–26. Springer, Berlin, SpringerMaterials (1986).

[15] G. Bertero, D. Wachenschwanz, S. Malhotra, S. Velu, B. Bian, D. Stafford, Y. Wu, T. Yamashita, and S. X. Wang, "Optimization of granular double-layer perpendicular media", IEEE Trans. Magn. **38**, 1627 (2002).

[16] J. Z. Shi, S. N. Piramanayagam, J. M. Zhao, C. S. Mah, and B. Liu, "High Writability Perpendicular Recording Media With Low Noise Crystalline Soft Underlayer", IEEE Trans. Magn. **43**, 873 (2007).

[17] T. Oikawa, M. Nakamura, H. Uwazumi, T. Shimatsu, H. Muraoka, and Y. Nakamura, "Microstructure and magnetic properties of CoPtCr-SiO$_2$ perpendicular recording media", IEEE Trans. Magn. **38**, 1976 (2002).

[18] H. Uwazumi, K. Enomoto, Y. Sakai, S. Takenoiri, T. Oikawa, and S. Watanabe, "CoPtCr-SiO$_2$ granular media for high-density perpendicular recording", IEEE Trans. Magn. **39**, 1914 (2003).

[19] E. Velu, S. Malhotra, G. Bertero, and D. Wachenschwanz, "Low-noise CoCrPtO perpendicular media with improved resolution", IEEE Trans. Magn. **39**, 668 (2003).

[20] H. Yamane, S. Watanabe, J. Ariake, N. Honda, K. Ouchi, and S. Iwasaki, "Effect of oxygen on magnetic properties of Co-Pt-Cr-SiO$_2$ thin films for perpendicular recording media", J. Magn. Magn. Mater. **287**, 153 (2005).

[21] T. Keitoku, J. Ariake, and N. Honda, "Preparation condition of Co-Pt-Cr-SiO$_2$ films with high coercivity", J. Magn. Magn. Mater. **287**, 172 (2005).

[22] S. N. Piramanayagam, M. J. Liau, J. Z. Shi, and B. C. Lim, "Textured growth of CoFe for soft underlayers in CoCrPt:SiO$_2$ perpendicular magnetic recording media", J. Magn. Magn. Mater. **303**, e152 (2006).

[23] D. Weller, A. Moser, L. Folks, M. E. Best, W. Lee, M. F. Toney, M. Schwickert, J.-U. Thiele, and M. F. Doerner, "High K$_u$ materials approach to 100 Gbits/in^2", IEEE Trans. Magn. **36**, 10 (2000).

[24] D. Weller and A. Moser, "Thermal effect limits in ultrahigh-density magnetic recording", IEEE Trans. Magn. **35**, 4423 (1999).

[25] A. Moser, K. Takano, D. T. Margulies, M. Albrecht, Y. Sonobe, Y. Ikeda, S. Sun, and E. E. Fullerton, "Magnetic recording: advancing into the future", J. Phys. D: Appl. Phys. **35**, R157 (2002).

[26] F. J. A. den Broeder, W. Hoving, and P. J. H. Bloemen, "Magnetic anisotropy of multilayers", J. Magn. Magn. Mater. **93**, 562 (1991).

[27] S. Hashimoto, Y. Ochiai, and K. Aso, "Perpendicular magnetic anisotropy and magnetostriction of sputtered Co/Pd and Co/Pt multilayered films", J. Appl. Phys. **66**, 4909 (1989).

[28] Y. P. Lee, S. K. Kim, J. S. Kang, Y. M. Koo, J. I. Jeong, J. H. Hong, and H. J. Shin, "Properties of Co/Pd multilayers prepared by UHV physical vapor deposition", J. Magn. Magn. Mater. **126**, 316 (1993).

[29] C.-J. Lin, G. L. Gorman, C. H. Lee, R. F. C. Farrow, E. E. Marinero, H. V. Do, H. Notarys, and C. J. Chien, "Magnetic and structural properties of Co/Pt multilayers", J. Magn. Magn. Mater. **93**, 194 (1991).

[30] D. G. Stinson and S. C. Shin, "Magnetization and anisotropy of Co/Pd multilayer thin films", J. Appl. Phys. **67**, 4459 (1990).

[31] T. Suzuki, "Coercivity mechanism in (Co/Pt) and (Co/Pd) multilayers", IEEE Trans. Magn. **31**, 4085 (1995).

[32] S. Tibus, T. Strache, F. Springer, D. Makarov, H. Rohrmann, T. Schrefl, J. Fassbender, and M. Albrecht, "Magnetic properties of granular CoCrPt:SiO$_2$ films as tailored by Co$^+$ irradiation", J. Appl. Phys. **107**, 093915 (2010).

[33] C. T. Rettner, S. Anders, T. Thomson, M. Albrecht, Y. Ikeda, M. E. Best, and B. D. Terris, "Magnetic characterization and recording properties of patterned Co$_7$0Cr$_1$8Pt$_1$2 perpendicular media", IEEE Trans. Magn. **38**, 1725 (2002).

[34] M. T. Georgieva, P. J. Grundy, and N. D. Telling, "Ion irradiation and thermally induced mixing of CoCrPt/Cr multilayered films", Appl. Phys. Lett. **90**, 042509 (2007).

[35] C. Choi, H. Daehoon, A. I. Gapin, and J. Sungho, "Control of M-H Loop Shape in Perpendicular Recording Media by Ion Implantation", IEEE Trans. Magn. **43**, 2121 (2007).

[36] M. Kryder. "Magnetic recording beyond the superparamagnetic limit. In *Magnetics Conference, 2000. INTERMAG 2000 Digest of Technical Papers. 2000 IEEE International*, pages 575–575 (2000).

[37] R. E. Rottmayer, S. Batra, D. Buechel, W. A. Challener, J. Hohlfeld, Y. Kubota, L. Li, B. Lu, C. Mihalcea, K. Mountfield, K. Pelhos, C. Peng, T. Rausch, M. Seigler, D. Weller, and X. M. Yang, "Heat-Assisted Magnetic Recording", IEEE Trans. Magn. **42**, 2417 (2006).

[38] C. A. Ross, "Patterned magnetic recording media", Ann. Rev. Mater. Res. **31**, 203 (2001).

[39] R. Victora. "Perpendicular Recording Media. In M. L. Plumer, J. Ek, D. Weiler, G. Ertl, R. Gomer, H. Luth, and D. L. Mills, editors, *The Physics of Ultra-High-Density Magnetic Recording*, volume 41 of *Springer Series in Surface Sciences*, pages 230–248. Springer, Berlin (2001).

[40] H. Richter, A. Dobin, O. Heinonen, K. Gao, R. Veerdonk, R. Lynch, J. Xue, D. Weller, P. Asselin, M. Erden, and R. Brockie, "Recording on Bit-Patterned Media at Densities of 1 Tb/in^2 and Beyond", IEEE Trans. Magn. **42**, 2255 (2006).

[41] H. J. Richter, A. Y. Dobin, R. T. Lynch, D. Weller, R. M. Brockie, O. Heinonen, K. Z. Gao, J. Xue, R. J. M. v. d. Veerdonk, P. Asselin, and M. F. Erden, "Recording potential of bit-patterned media", Appl. Phys. Lett. **88**, 222512 (2006).

[42] B. Terris, T. Thomson, and G. Hu, "Patterned media for future magnetic data storage", Microsyst. Technol. **13**, 189 (2007).

[43] B. D. Terris, "Fabrication challenges for patterned recording media", J. Magn. Magn. Mater. **321**, 512 (2009).

[44] O. Heinonen and K. Z. Gao. "Extensions of perpendicular recording. In *Eighth Perpendicular Magnetic Recording Conference*, volume 320, page 2885 (2008).

[45] O. Hellwig, J. K. Bosworth, E. Dobisz, D. Kercher, T. Hauet, G. Zeltzer, J. D. Risner-Jamtgaard, D. Yaney, and R. Ruiz, "Bit patterned media based on block copolymer directed assembly with narrow magnetic switching field distribution", Appl. Phys. Lett. **96**, 052511 (2010).

[46] S. Y. Chou, P. R. Krauss, and P. J. Renstrom, "Imprint Lithography with 25-Nanometer Resolution", Science **272**, 85 (1996).

[47] S. Takenoiri, "The current status and future of granular media", J. Magn. Magn. Mater. **321**, 562 (2009).

[48] B. D. Terris and T. Thomson, "Nanofabricated and self-assembled magnetic structures as data storage media", J. Phys. D: Appl. Phys. **38**, R199 (2005).

[49] F. Luo, L. J. Heyderman, H. H. Solak, T. Thomson, , and M. E. Best, "Nanoscale perpendicular magnetic island arrays fabricated by extreme ultraviolet interference lithography", Appl. Phys. Lett. **92**, 102505 (2008).

[50] M. Grobis, E. Dobisz, O. Hellwig, M. E. Schabes, G. Zeltzer, T. Hauet, and T. R. Albrecht, "Measurements of the write error rate in bit patterned magnetic recording at 100–320 Gb/in[sup 2]", Appl. Phys. Lett. **96**, 052509 (2010).

[51] T. Wang, Y. Wang, Y. Fu, T. Hasegawa, H. Oshima, K. Itoh, K. Nishio, H. Masuda, F. S. Li, H. Saito, and S. Ishio, "Magnetic behavior in an ordered Co nanorod array", Nanotechnology **19**, 455703 (2008).

[52] A. Walcarius, E. Sibottier, M. Etienne, and J. Ghanbaja, "Electrochemically assisted self-assembly of mesoporous silica thin films", Nat. Mater. **6**, 602 (2007).

[53] C. Schulze, M. Faustini, J. Lee, H. Schletter, M. U. Lutz, P. Krone, M. Gass, K. Sader, A. L. Bleloch, M. Hietschold, M. Fuger, D. Suess, J. Fidler, U. Wolff, V. Neu, D. Grosso, D. Makarov, and M. Albrecht, "Magnetic films on nanoperforated templates: a route towards percolated perpendicular media", Nanotechnology **21**, 495701 (2010).

[54] I. Bita, J. K. W. Yang, Y. S. Jung, C. A. Ross, E. L. Thomas, and K. K. Berggren, "Graphoepitaxy of Self-Assembled Block Copolymers on Two-Dimensional Periodic Patterned Templates", Science **321**, 939 (2008).

[55] M. Albrecht, G. Hu, I. L. Guhr, T. C. Ulbrich, J. Boneberg, P. Leiderer, and G. Schatz, "Magnetic multilayers on nanospheres", Nat. Mater. **4**, 203 (2005).

[56] S. Facsko, T. Dekorsy, C. Koerdt, C. Trappe, H. Kurz, A. Vogt, and H. L. Hartnagel, "Formation of Ordered Nanoscale Semiconductor Dots by Ion Sputtering", Science **285**, 1551 (1999).

[57] P. Krone, C. Brombacher, D. Makarov, K. Lenz, D. K. Ball, F. Springer, H. Rohrmann, J. Fassbender, and M. Albrecht, "Nanocap arrays of granular CoCrPt:SiO$_2$ films on silica particles: tailoring of the magnetic properties by Co$^+$ irradiation", Nanotechnology **21**, 385703 (2010).

[58] S. Facsko, T. Bobek, H. Kurz, T. Dekorsy, S. Kyrsta, and R. Cremer, "Ion-induced formation of regular nanostructures on amorphous GaSb surfaces", Appl. Phys. Lett. **80**, 130 (2002).

[59] E. Kneller, "Ferromagnetismus", Springer, Berlin (1962).

[60] J. H. van Vleck. "Quantum mechanics - The key to understanding magnetism. In *Nobel Lecture* (1977).

[61] A. Aharoni, "Introduction to the Theory of Ferromagnetism", second edition, Oxford University Press, Oxford (2001).

[62] S. Chikazumi, "Physics of Feromagnetism", second edition, Oxford University Press, Oxford (1997).

[63] C. Kittel, "Introduction to Solid State Physics", seventh edition, John Wiley & Sons, New York (1996).

[64] B. D. Cullity and C. D. Graham, "Introduction to Magnetic Materials", second edition, Wiley-IEEE Press, New York (2008).

[65] N. H. D. Bohr, "Studier over Metallenes Elektrontheori", Ph.D. thesis, Københavns Universitet (1911).

[66] W. Heisenberg, "Zur Theorie des Ferromagnetismus", Z. Phys. A: Hadrons Nucl. **49**, 619 (1928).

[67] J. D. Jackson, "Classical Electrodynamics", third edition, John Wiley & Sons, New York (1999).

[68] F. Nolting, "Grundkurs Theoretische Physik 3: Elektrodynamik", volume three, fifth edition, Springer, Berlin (2002).

[69] A. S. Arrot. "Magnetism in SI Units and Gaussian Units. In J. A. C. Bland and B. Heinrich, editors, *Ultrathin Magnetic Structures I: An Introduction to the Electronic, Magnetic and Structural Properties.*, volume two, chapter 1.2, pages 7–19. Springer, Berlin (1994).

[70] R. Skomski, "Simple Models of Magnetism", Oxford University Press, Oxford (2008).

[71] W. Pauli, "Zur Quantenmechanik des magnetischen Elektrons", Z. Phys. A: Hadrons Nucl. **43**, 601 (1927).

[72] F. Schwabl, "Quantenmechanik für Fortgeschrittene", fourth edition, Springer, Berlin (2005).

[73] S. Blundell, "Magnetism in Condensed Matter", Oxford University Press, Oxford (2001).

[74] A. Wachter, "Relativistische Quantenmechanik", volume one, Springer, Berlin (2005).

[75] P. Bruno, "Physical Origins and Theoretical Models of Magnetic Anisotropy", volume 24. Magnetismus von Festkörpern und Grenzflächen: of *IFF-Ferienkurs*, chapter 24, pages 24.1–24.28, Forschungszentrum Jülich GmbH (1993).

[76] S. Blügel, "Magnetische Anisotropie und Magnetostriktion (Theorie)", volume 30. Magnetische Schichtsysteme of *IFF-Ferienkurs*, chapter C1, pages 1–68, Forschungszentrum Jülich GmbH (1999).

[77] J. Lindner and M. Farle, "Magnetic Anisotropy of Heterostructures", volume 227 of *Springer Tracts in Modern Physics.*, chapter 2, pages 45–96, Springer, Berlin (2007).

[78] J. W. Gibbs, "A Method of Geometrical Representation of the Thermodynamic Properties of Substances by Means of Surfaces", Trans. Conn. Acad. Arts Sci. **2**, 382 (1873).

[79] F. Schwabl, "Statistische Mechanik", third edition, Springer, Berlin (2006).

[80] P. Bruno, "Tight-binding approach to the orbital magnetic moment and magnetocrystalline anisotropy of transition-metal monolayers", Phys. Rev. B **39**, 865 (1989).

[81] T. L. Gilbert, "Formulation, Foundations and Applications of the Phenomenological of Ferromagnetism", Ph.D. thesis, Graduate School of Illinois Institute of Technology (1956).

[82] T. L. Gilbert, "A phenomenological theory of damping in ferromagnetic materials", IEEE Trans. Magn. **40**, 3443 (2004).

[83] C. Bilzer, "Susceptibilité micro-ondes de couches minces ferromagnétiques : métrologie et analyse de la dynamique de l'aimantation", Ph.D. thesis, Université Paris-Sud 11 (2007).

[84] L. Landau and E. Lifshitz, "On the theory of the dispersion of magnetic permeability in ferromagnetic bodies", Physik. Zeits. Sowjetunion **8**, 153 (1935).

[85] L. Néel, "Théorie du traînage magnétique des ferromagnétiques en grains fins avec applications aux terres cuites", Ann. Géophys **5**, 99 (1949).

[86] J. H. van Vleck, "On the Anisotropy of Cubic Ferromagnetic Crystals", Phys. Rev. **52**, 1178 (1937).

[87] J. Stöhr and H. C. Siegmann, "Magnetism, From fundamentals to nanoscale dynamics", Springer, Berlin (2006).

[88] P. Weinberger and L. Szunyogh, "Perpendicular magnetism in magnetic multilayer systems", Comp. Mat. Sci. **17**, 414 (2000).

[89] N. W. Ashcroft and D. Mernim, "Festkörperphysik", third edition, R. Oldenbourg, München (2007).

[90] F. Bloch and G. Gentile, "Zur Anisotropie der Magnetisierung ferromagnetischer Einkristalle", Z. Phys. A: At. Nucl. **70**, 395 (1931).

[91] J. A. Osborn, "Demagnetizing Factors of the General Ellipsoid", Phys. Rev. **67**, 351 (1945).

[92] A. Aharoni, "Demagnetizing factors for rectangular ferromagnetic prisms", J. Appl. Phys. **83**, 3432 (1998).

[93] A. Aharoni, "Local Demagnetization in a Rectangular Ferromagnetic Prism", Phys. Stat. Sol. B **229**, 1413 (2002).

[94] M. Beleggia, D. Vokoun, and M. De Graef, "Demagnetization factors for cylindrical shells and related shapes", J. Magn. Magn. Mater. **321**, 1306 (2009).

[95] M. Beleggia, S. Tandon, Y. Zhu, and M. De Graef, "On the computation of the demagnetization tensor for particles of arbitrary shape", J. Magn. Magn. Mater. **272-276**, E1197 (2004).

[96] M. Beleggia, M. D. Graef, Y. T. Millev, D. A. Goode, and G. Rowlands, "Demagnetization factors for elliptic cylinders", J. Phys. D: Appl. Phys. **38**, 3333 (2005).

[97] M. Sato and Y. Ishii, "Simple and approximate expressions of demagnetizing factors of uniformly magnetized rectangular rod and cylinder", J. Appl. Phys. **66**, 983 (1989).

[98] K. Tang, H. W. Zhang, Q. Y. Wen, and Z. Y. Zhong, "Demagnetization field of ferromagnetic equilateral triangular prisms", Physica B **363**, 96 (2005).

[99] C. R. Mann, "Demagnetization Factors for Cylindrical Rods", Phys. Rev. (Series I) **3**, 359 (1896).

[100] Z. Frait, "The g-factor in pure polycrystalline iron", Czech. J. Phys. **27**, 185 (1977).

[101] M. B. Stearns. "1.1.2.10 g factors and ferromagnetic resonance properties. In H. Wijn, editor, *Landolt-Börnstein*, volume 19a: 3d, 4d and 5d Elements, Alloys and Compounds of *Landolt-Börnstein, New Series - Group III Condensed Matter: Numerical Data and Functional Relationships in Science and Technology*, chapter 1.1.2 Fe, Co, Ni, pages 85–90. Springer, Berlin, SpringerMaterials (1986).

[102] R. A. Reck and D. L. Fry, "Orbital and Spin Magnetization in Fe-Co, Fe-Ni, and Ni-Co", Phys. Rev. **184**, 492 (1969).

[103] C. J. Gadsden and M. Heath, "Ferromagnetic resonance linewidths of nickel single crystals", J.Phys. F: Met. Phys. **7**, L273 (1977).

[104] J. P. Nibarger, R. Lopusnik, Z. Celinski, and T. J. Silva, "Variation of magnetization and the Landé g factor with thickness in Ni–Fe films", Appl. Phys. Lett. **83**, 93 (2003).

[105] D. Markó, "Magnetostatics and Dynamics of Ion Irradiated NiFe/Ta Multilayer Films Studied by VNA-FMR", Ph.D. thesis, Technische Universität Dresden (2010).

[106] C. J. Oates, F. Y. Ogrin, S. L. Lee, P. C. Riedi, G. M. Smith, and T. Thomson, "High field ferromagnetic resonance measurements of the anisotropy field of longitudinal recording thin-film media", J. Appl Phys. **91**, 1417 (2002).

[107] W. Pauli, "Zur Frage der Zuordnung der Komplexstrukturterme in starken und in schwachen äußere Feldern", Z. Phys. A: Hadrons Nucl. **20**, 371 (1923).

[108] W. Heisenberg, "Über eine Abänderung der formalen Regeln der Quantentheorie beim Problem der anomalen Zeemaneffekte", Z. Phys. A: Hadrons Nucl. **26**, 291 (1924).

[109] W. Heisenberg, "Zur Quantentheorie der Multiplettstruktur und der anomalen Zeemaneffekte", Z. Phys. A: Hadrons Nucl. **32**, 841 (1925).

[110] T. Mayer-Kuckuk, "Atomphysik: Eine Einführung", fifth edition, Teubner, Wiesbaden (1997).

[111] W. Demtröder, "Experimentalphysik 3: Atome, Moleküle und Festkörper", second edition, Springer, Berlin (2000).

[112] J. H. Van Vleck, "Theory of the Variations in Paramagnetic Anisotropy Among Different Salts of the Iron Group", Phys. Rev. **41**, 208 (1932).

[113] J. Lindner, "Ferromagnetische Resonanz an ultradünnen magnetischen Einfach- und Mehrfachlagen der 3d-Übergangsmetalle - Statik und Dynamik", Ph.D. thesis, Freie Universität Berlin (2002).

[114] G. E. Pake, "Paramagnetic Resonance: An Introductory Monograph", W.A. Benjamin, San Francisco (1962).

[115] G. E. Pake and T. L. Estle, "The Physical Principles of Electron Paramagnetic Resonance", second edition, Benjamin-Cummings Publishing Company, San Francisco (1973).

[116] A. Abragam and B. Bleaney, "Electron Paramagnetic Resonance of Transition Ions", reprint edition, Oxford University Press, Oxford (2012).

[117] G. Bertotti, "Hysteresis in Magnetism: for Physicists, Materials Scientists, and Engineers (Electromagnetism)", one edition, Academic Press, Waltham (1998).

[118] B. Bertotti and I. D. Mayergoyz, "The Science of Hysteresis", three edition, Academic Press, Waltham (2006).

[119] D. C. Jiles and J. B. Thoelke, "Theory of ferromagnetic hysteresis: determination of model parameters from experimental hysteresis loops", IEEE Trans. Magn. **25**, 3928 (1989).

[120] A. Hubert and R. Schäfer, "Magnetic Domains, The Analysis of Magnetic Microstructures", third corrected printing edition, Springer, Berlin (2000).

[121] R. Schäfer, "XX. Magnetische Mikrostuktur", volume 30. Magnetische Schichtsysteme: Magnetische Mikrostrukturen. of *IFF-Ferienkurs*, chapter B6, pages 1–28, Forschungszentrum Jülich GmbH (1999).

[122] R. J. M. van de Veerdonk, X. Wu, and D. Weller, "Switching field distributions and ΔM measurements for perpendicular media", IEEE Trans. Magn. **38**, 2450 (2002).

[123] R. J. M. van de Veerdonk, X. Wu, and D. Weller, "Determination of switching field distributions for perpendicular recording media", IEEE Trans. Magn. **39**, 590 (2003).

[124] A. Berger, Y. Xu, B. Lengsfield, Y. Ikeda, and E. Fullerton, "ΔH(M,ΔM) method for the determination of intrinsic switching field distributions in perpendicular media", IEEE Trans. Magn. **41**, 3178 (2005).

[125] X. Wu and R. J. M. van de Veerdonk, "Investigation on the Mean Field Assumptions for Switching Field Distribution Measurements", IEEE Trans. Magn. **44**, 336 (2008).

[126] A. Berger, B. Lengsfield, and Y. Ikeda, "Determination of intrinsic switching field distributions in perpendicular recording media (invited)", J. Appl. Phys. **99**, 08E705 (2006).

[127] O. Hellwig, A. Berger, T. Thomson, E. Dobisz, Z. Z. Bandic, H. Yang, D. S. Kercher, and E. E. Fullerton, "Separating dipolar broadening from the intrinsic switching field distribution in perpendicular patterned media", Appl. Phys. Lett. **90**, 162516 (2007).

[128] S. Tibus, "Modification and nanostructuring of magnetic materials by ion irradiation", Ph.D. thesis, Universität Konstanz (2010).

[129] I. N. Bronstein, K. A. Semendjajew, G. Musiol, and H. Muehlig, "Taschenbuch der Mathematik.", seventh edition, Harri Deutsch Verlag, Frankfurt am Main (2008).

[130] D. E. S. Stanescu, "Magnetization dynamics in magnetic nanostructrures", Ph.D. thesis, L'Univesité Joseph Fourier - Grenoble 1 (2003).

[131] I. Radu, G. Woltersdorf, M. Kiessling, A. Melnikov, U. Bovensiepen, J.-U. Thiele, and C. H. Back, "Laser-Induced Magnetization Dynamics of Lanthanide-Doped Permalloy Thin Films", Phys. Rev. Lett. **102**, 117201 (2009).

[132] J.-Y. Bigot, M. Vomir, and E. Beaurepaire, "Coherent ultrafast magnetism induced by femtosecond laser pulses", Nat. Phys. **5**, 515 (2009).

[133] A. Barman, S. Wang, O. Hellwig, A. Berger, E. E. Fullerton, and H. Schmidt, "Ultrafast magnetization dynamics in high perpendicular anisotropy [Co/Pt]$_n$ multilayers", J. Appl. Phys. **101**, 09D102 (2007).

[134] M. Djordjevic, M. Lüttich, P. Moschkau, P. Guderian, T. Kampfrath, R. G. Ulbrich, M. Münzenberg, W. Felsch, and J. S. Moodera, "Comprehensive view on ultrafast dynamics of ferromagnetic films", Phys. Stat. Sol. C **3**, 1347 (2006).

[135] O. Mosendz, "Magnetization Dynamics in ultrathin magnetic films", Ph.D. thesis, Simon Frasier University (2008).

[136] C. Bunce, "Experimental measurement of magnetisation dynamics in Magnetite and HAMR media using TRMOKE", Ph.D. thesis, University of York (2008).

[137] T. Rasing, H. van den Berg, T. Gerrits, and J. Hohlfeld, "Ultrafast Magnetization and Switching Dynamics", volume 87 of *Topics in Applied Physics: Spin Dynamics in Confined Magnetic Structures*, chapter 7, pages 216–255, Springer, Berlin (2003).

[138] C. D. Stanciu, "Laser-Induced Femtosecond Magnetic Recording", Phd thesis, Radboud University Nijmegen (2008).

[139] G. Woltersdorf, M. Buess, B. Heinrich, and C. H. Back, "Time Resolved Magnetization Dynamics of Ultrathin Fe(001) Films: Spin-Pumping and Two-Magnon Scattering", Phys. Rev. Lett. **95**, 037401 (2005).

[140] M. Getzlaff, "Fundamentals of Magnetism", Springer, Berlin (2008).

[141] H. Suhl, "Theory of the magnetic damping constant", IEEE Trans. Magn. **34**, 1834 (1998).

[142] M. L. Plumer and J. van Ek, "Introduction to micromagnetic recording physics", chapter 1, pages 1–32, Springer Series in Surface Sciences., Springer, Berlin, first edition (2001).

[143] M. A. Makeev, R. Cuerno, and A.-L. Barabás, "Morphology of ion-sputtered surfaces", Nucl. Instrum. Methods Phys. Res., Sect. B **197**, 185 (2002).

[144] R. M. Bradley and J. M. E. Harper, "Theory of ripple topography induced by ion bombardment", J. Vac. Sci. Technol. A **6**, 2390 (1988).

[145] M. Navez, C. Sella, and D. Chaperot, "Etude de l'attaque du verre par bombardement ionique", C. R. Acad. Sci. Paris **254**, 240 (1962).

[146] P. Sigmund, "Theory of Sputtering. I. Sputtering Yield of Amorphous and Polycrystalline Targets", Phys. Rev. **184**, 383 (1969).

[147] R. M. Bradley and P. D. Shipman, "Spontaneous Pattern Formation Induced by Ion Bombardment of Binary Compounds", Phys. Rev. Lett. **105**, 145501 (2010).

[148] R. M. Bradley, "Theory of nanodot and sputter cone arrays produced by ion sputtering with concurrent deposition of impurities", Phys. Rev. B **83**, 195410 (2011).

[149] Y. J. Chen, J. P. Wang, E. W. Soo, L. Wu, and T. C. Chong, "Periodic magnetic nanostructures on self-assembled surfaces by ion beam bombardment", J. Appl. Phys. **91**, 7323 (2002).

[150] U. Valbusa, C. Boragno, and F. B. d. Mongeot, "Nanostructuring surfaces by ion sputtering", J. Phys.: Condens. Mat. **14**, 8153 (2002).

[151] W. L. Chan and E. Chason, "Making waves: Kinetic processes controlling surface evolution during low energy ion sputtering", J. Appl. Phys. **101**, 121301 (2007).

[152] V. B. Shenoy, W. L. Chan, and E. Chason, "Compositionally Modulated Ripples Induced by Sputtering of Alloy Surfaces", Phys. Rev. Lett. **98**, 256101 (2007).

[153] A. Keller, A. Biermanns, G. Carbone, J. Grenzer, S. Facsko, O. Plantevin, R. Gago, and T. Metzger, "Transition from smoothing to roughening of ion-eroded GaSb surfaces", Appl. Phys. Lett. **94**, 193103 (2009).

[154] A. Keller and S. Facsko, "Ion-Induced Nanoscale Ripple Patterns on Si Surfaces: Theory and Experiment.", Materials **3**, 4811 (2010).

[155] S. Facsko, H. Kurz, and T. Dekorsy, "Energy dependence of quantum dot formation by ion sputtering", Phys. Rev. B **63**, 165329 (2001).

[156] S. Facsko, T. Bobek, A. Stahl, H. Kurz, and T. Dekorsy, "Dissipative continuum model for self-organized pattern formation during ion-beam erosion", Phys. Rev. B **69**, 153412 (2004).

[157] S. Le Roy, E. Søndergård, I. S. Nerbø, M. Kildemo, and M. Plapp, "Diffuse-interface model for nanopatterning induced by self-sustained ion-etch masking", Phys. Rev. B **81**, 161401 (2010).

[158] T. Bobek, S. Facsko, H. Kurz, T. Dekorsy, M. Xu, and C. Teichert, "Temporal evolution of dot patterns during ion sputtering", Phys. Rev. B **68**, 085324 (2003).

[159] T. Bobek, N. Mikuszeit, J. Camarero, S. Kyrsta, L. Yang, M. A. Niño, C. Hofer, L. Gridneva, D. Arvanitis, R. Miranda, J. J. de Miguel, C. Teichert, and H. Kurz, "Self-Organized Hexagonal Patterns of Independent Magnetic Nanodots", Adv. Mater. **19**, 4375 (2007).

[160] W. Möller, W. Eckstein, and J. P. Biersack, "Tridyn-binary collision simulation of atomic collisions and dynamic composition changes in solids", Comput. Phys. Commun. **51**, 355 (1988).

[161] W. Möller and M. Posselt. "TRIDYN – FZR User Manual". Helmholtz-Zentrum Dresden–Rossendorf, Bautzner Landstraße 400, 01328 Dresden, Germany, 1 edition, April 2002.

[162] D. Bonnenberg, K. A. Hempel, and H. P. J. Wijn. "1.2.1.1 Phase diagrams, lattice parameters. In H. Wijn, editor, *Landolt-Börnstein*, volume 19a: 3d, 4d and 5d Elements, Alloys and Compounds of *Landolt-Börnstein, New Series - Group III Condensed Matter: Numerical Data and Functional Relationships in Science and Technology*, chapter 1.2. Alloys between Fe, Co or Ni:, pages 144–152. Springer, Berlin, SpringerMaterials (1986).

[163] H. Schultz. "Cr (chromium). In H. Ullmaier, editor, *Landolt-Börnstein*, volume 25: Atomic Defects in Metals of *Landolt-Börnstein, New Series - Group III Condensed Matter: Numerical Data and Functional Relationships in Science and Technology*, chapter 2.2.3 Data, pages 122–125. Springer, Berlin, SpringerMaterials (1986).

[164] Collaboration: Authors and Editors of the LB Volumes III/17A-22A-41A1b. "Gallium antimonide (GaSb), lattice parameter, thermal expansion. In O. Madelung, U. Rössler, and M. Schulz, editors, *Landolt-Börnstein*, volume 41A1b: Group IV Elements, IV-IV and III-V Compounds. Part b - Electronic, Transport, Optical and Other Properties of *Landolt-Börnstein, New Series - Group III Condensed Matter: Numerical Data and Functional Relationships in Science and Technology*, chapter Gallium antimonide (GaSb). Springer, Berlin, SpringerMaterials (1986).

[165] K. Schroeder, "Oberflächendiffusion: Mikroskopische Parameter und Modelle zur Kinetik des epitaktischen Wachstums", volume 28. Dynamik und Strukturbildung in kondensierter Materie of *IFF-Ferienkurs*, chapter C2., pages 1–24, Forschungszentrum Jülich GmbH (1997).

[166] E. Bauer, "Phänomenologische Theorie der Kristallabscheidung an Oberflächen. I", Z. Kristallogr. **110**, 372 (1958).

[167] M. Volmer and A. Weber, "Keimbildung in übersättigten Gebilden", Z. Phys. Chem. **119**, 277 (1926).

[168] J. A. Thornton, "Magnetron sputtering: basic physics and application to cylindrical magnetron", J. Vac. Sci. Technol. **15**, 171 (1978).

[169] S. Swann, "Magnetron sputtering", Phys. Technol. **19**, 67 (1988).

[170] J. Musil, "Recent advances in magnetron sputtering technology", Surf. Coat. Tech. **100-101**, 280 (1998).

[171] A. Belkind, A. Freilich, J. Lopez, Z. Zhao, W. Zhu, and K. Becker, "Characterization of pulsed dc magnetron sputtering plasmas", New J. Phys. **7**, 90 (2005).

[172] R. D. Arnell and P. J. Kelly, "Recent advances in magnetron sputtering", Surf. Coat. Tech. **112**, 170 (1999).

[173] P. J. Kelly and R. D. Arnell, "Magnetron sputtering: a review of recent developments and applications", Vacuum **56**, 159 (2000).

[174] C. Kittel, "Interpretation of Anomalous Larmor Frequencies in Ferromagnetic Resonance Experiment", Phys. Rev. **71**, 270 (1947).

[175] S. V. Vonsovskii, "Ferromagnetic resonance; the phenomenon of resonant absorption of a high-frequency magnetic field in ferromagnetic substances", volume 4 of *International series of monographs on solid state physics*, first edition, Pergamon Press, Oxford (1966).

[176] R. Meckenstock, "Untersuchung der magnetischen Eigenschaften von Fe/Ag-Schichtsystemen mit der konventionellen und der ortsaufgelösten ferromagnetischen Resonanz", Ph.D. thesis, Ruhr-Universität Bochum (1997).

[177] A. Banholzer, R. Narkowicz, C. Hassel, R. Meckenstock, S. Stienen, O. Posth, D. Suter, M. Farle, and J. Lindner, "Visualization of spin dynamics in single nanosized magnetic elements", Nanotechnology **22**, 295713 (2011).

[178] M. Sparks, "Ferromagnetic-Relaxation Theory", McGraw-Hill, New York (1964).

[179] J. H. Van Vleck, "Ferromagnetic resonance", Physica **17**, 234 (1951).

[180] C. Kittel, "Ferromagnetic resonance", J. Phys. Radium **12**, 291 (1951).

[181] C. Kittel, "On the Theory of Ferromagnetic Resonance Absorption", Phys. Rev. **73**, 155 (1948).

[182] D. Polder, "On the Quantum Theory of Ferromagnetic Resonance", Phys. Rev. **73**, 1116 (1948).

[183] C. Kittel, "On the Gyromagnetic Ratio and Spectroscopic Splitting Factor of Ferromagnetic Substances", Phys. Rev. **76**, 743 (1949).

[184] D. Polder, "On the theory of ferromagnetic resonance", Physica **15**, 253 (1949).

[185] J. H. van Vleck, "Concerning the Theory of Ferromagnetic Resonance Absorption", Phys. Rev. **78**, 266 (1950).

[186] C. P. Poole Jr., "Electron Spin Resonance: A Comprehensive Treatise on Experimental Techniques", first edition, Interscience Publishers a division of John Wiley & Sons, New York (1967).

[187] C. P. Poole Jr. and H. A. Farach, "Handbook of electron spin resonance", volume 1, AIP Press, College Park (1994).

[188] C. P. Poole Jr. and H. A. Farach, "Handbook of electron spin resonance", volume 2, Springer, Berlin (1999).

[189] J. A. Weil and J. R. Bolton, "Electron Paramagnetic Resonance: Elementary Theory and Practical Applications", second edition, Wiley-Interscience, New York (2007).

[190] M. Brustolon and E. Giamello, editors, "Electron Paramagnetic Resonance: A Practitioner€™s Toolkit", first edition, John Wiley & Sons, New York (2009).

[191] J. H. E. Griffiths, "Ferromagnetic resonance in thin Ni-films", Physica **17**, 253 (1950).

[192] J. Smit and H. G. Beljers, "Ferromagnetic Resonance Absorption in $BaFe_{12}O_{19}$ a highly anisotropic crystal", Philips Res. Rep. **10**, 113 (1955).

[193] L. Baselgia, M. Warden, F. Waldner, S. L. Hutton, J. E. Drumheller, Y. Q. He, P. E. Wigen, and M. Maryško, "Derivation of the resonance frequency from the free energy of ferromagnets", Phys. Rev. B **38**, 2237 (1988).

[194] C. Wen, "Coplanar Waveguide: A Surface Strip Transmission Line Suitable for Nonreciprocal Gyromagnetic Device Applications", IEEE T. Microw. Theory **17**, 1087 (1969).

[195] R. N. Simons, "Coplanar Waveguide Circuits, Components, and Systems", first edition, John Wiley & Sons, Inc, New York (2001).

[196] S. S. Kalarickal, "Ferromagnetic relaxation in (1) metallic thin films and (2) bulk ferrites and composite materials for information storage device and microwave applications", Ph.D. thesis, Colorado State University (2006).

[197] I. Neudecker, "Magnetization Dynamics of Confined Ferromagnetic Systems", Ph.D. thesis, Universität Regensburg (2006).

[198] Z. Celinski, K. B. Urquhart, and B. Heinrich, "Using ferromagnetic resonance to measure the magnetic moments of ultrathin films", J. Magn. Magn. Mater. **166**, 6 (1997).

[199] Y. K. Kim and T. J. Silva, "Magnetostriction characteristics of ultrathin permalloy films", Appl. Phys. Lett. **68**, 2885 (1996).

[200] D. Mills and S. Rezende, "Spin Damping in Ultrathin Magnetic Films", volume 87/2003 of *Topics in Applied Physics: Spin Dynamics in Confined Magnetic Structures*, chapter 2, pages 27–59, Springer, Berlin (2003).

[201] J.-M. L. Beaujour, W. Chen, A. D. Kent, and J. Z. Sun, "Ferromagnetic resonance study of polycrystalline cobalt ultrathin films", J. Appl. Phys. **99**, 08N503 (2006).

[202] H. Suhl, "Ferromagnetic Resonance in Nickel Ferrite Between One and Two Kilomegacycles", Phys. Rev. **97**, 555 (1955).

[203] Y. V. Goryunov, N. N. Garif´yanov, G. G. Khaliullin, I. A. Garifullin, L. R. Tagirov, F. Schreiber, T. Mühge, and H. Zabel, "Magnetic anisotropies of sputtered Fe films on MgO substrates", Phys. Rev. B **52**, 13450 (1995).

[204] D. J. Twisselmann and R. D. McMichael, "Intrinsic damping and intentional ferromagnetic resonance broadening in thin Permalloy films", J. Appl. Phys. **93**, 6903 (2003).

[205] K. Zakeri, I. Barsukov, N. K. Utochkina, F. M. Römer, J. Lindner, R. Meckenstock, U. von Horsten, H. Wende, W. Keune, M. Farle, S. S. Kalarickal, K. Lenz, and Z. Frait, "Magnetic properties of epitaxial $Fe_3Si/MgO(001)$ thin films", Phys. Rev. B **76**, 214421 (2007).

[206] F. Schreiber, J. Pflaum, Z. Frait, T. Mühge, and J. Pelzl, "Gilbert damping and g-factor in Fe_xCo_{1-x} alloy films", Solid State Commun. **93**, 965 (1995).

[207] J. O. Rantschler and C. Alexander, Jr., "Ripple field effect on high-frequency measurements of FeTiN films", J. Appl. Phys. **93**, 6665 (2003).

[208] M. Born, E. Wolf, A. B. Bhatia, P. C. Clemmow, D. Gabor, A. R. Stokes, A. M. Taylor, P. A. Wayman, and W. L. Wilcock, "Principles of Optics: Electromagnetic Theory of Propagation, Interference and Diffraction of Light", seventh edition, Cambridge University Press, Cambridge (1999).

[209] H. Ebert and Y. Perlov, "Magnetooptische Effekte (Theorie)", volume 30. Magnetische Schichtsysteme: Magnetische Mikrostrukturen. of *IFF-Ferienkurs*, chapter C5, pages 1–28, Forschungszentrum Jülich GmbH (1999).

[210] P. S. Bechthold, "Magnetooptische Effekte: Phänomenologische Beschreibung und Anwendung", volume 30. Magnetische Schichtsysteme: Magnetische Mikrostrukturen. of *IFF-Ferienkurs*, chapter C8, pages 1–36, Forschungszentrum Jülich GmbH (1999).

[211] R. Vollmer, "Lineare und nichtlineare Magnetoptik an ultradünnen ferromagnetischen Schichten und Vielfachschichten", volume 30. Magnetische Schichtsysteme: Magnetische Mikrostrukturen. of *IFF-Ferienkurs*, chapter C7, pages 1–34, Forschungszentrum Jülich GmbH (1999).

[212] S. Bader and J. Erskine, "Magneto-Optical Effects in Ultrathin Magnetic Structures", volume II of *Ultrathin Magnetic Structures II*, chapter 4, page 297, Springer, Berlin (2005).

[213] E. R. Moog, C. Liu, S. D. Bader, and J. Zak, "Thickness and polarization dependence of the magnetooptic signal from ultrathin ferromagnetic films", Phys. Rev. B **39**, 6949 (1989).

[214] J. Zak, E. R. Moog, C. Liu, and S. D. Bader, "Fundamental magneto-optics", J. Appl. Phys. **68**, 4203 (1990).

[215] J. Zak, E. R. Moog, C. Liu, and S. D. Bader, "Universal approach to magneto-optics", J. Magn. Magn. Mater. **89**, 107 (1990).

[216] J. Zak, E. R. Moog, C. Liu, and S. D. Bader, "Magneto-optics of multilayers with arbitrary magnetization directions", Phys. Rev. B **43**, 6423 (1991).

[217] S. Bader, "SMOKE", J. Magn. Magn. Mater. **100**, 440 (1991).

[218] J. Zak, E. R. Moog, C. Liu, and S. D. Bader, "Erratum: Magneto-optics of multilayers with arbitrary magnetization directions", Phys. Rev. B **46**, 5883 (1992).

[219] P. Bruno, Y. Suzuki, and C. Chappert, "Magneto-optical Kerr effect in a paramagnetic overlayer on a ferromagnetic substrate: A spin-polarized quantum size effect", Phys. Rev. B **53**, 9214 (1996).

[220] H. Ebert, "Magneto-optical effects in transition metal systems", Rep. Prog. Phys. **59**, 1665 (1996).

[221] Z. Q. Qiu and S. D. Bader, "Surface magneto-optic Kerr effect", Rev. Sci. Instrum. **71**, 1243 (2000).

[222] S. Visnovsky, R. Lopusnik, M. Bauer, J. Bok, J. Fassbender, and B. Hillebrands, "Magnetooptic ellipsometry in multilayers at arbitrary magnetization", Opt. Express **9**, 121 (2001).

[223] M. Grimsditch and P. Vavassori, "The diffracted magneto-optic Kerr effect: what does it tell you?", J. Phys.: Condens. Mat. **16**, R275 (2004).

[224] R. L. Conger and G. H. Moore, "Direct Observation of High-Speed Magnetization Reversal in Films", J. Appl. Phys. **34**, 1213 (1963).

[225] D. A. Thompson and H. Chang, "Nanosecond Microscopic Measurement of Magnetic Film Switching by Kerr Magneto-Optic Apparatus", Phys. Stat. Sol. B **17**, 83 (1966).

[226] M. R. Freeman, "Picosecond pulsed-field probes of magnetic systems (invited)", J. Appl. Phys. **75**, 6194 (1994).

[227] M. D. Kaufmann, "Magnetization dynamics in all-optical pump-probe experiments: spin-wave modes and spin-current damping", Ph.D. thesis, Georg-August-Universität zu Göttingen (2006).

[228] S. S. Kalarickal, P. Krivosik, M. Wu, C. E. Patton, M. L. Schneider, P. Kabos, T. J. Silva, and J. P. Nibarger, "Ferromagnetic resonance linewidth in metallic thin films: Comparison of measurement methods", J. Appl. Phys. **99**, 093909 (2006).

[229] E. Beaurepaire, J.-C. Merle, A. Daunois, and J.-Y. Bigot, "Ultrafast Spin Dynamics in Ferromagnetic Nickel", Phys. Rev. Lett. **76**, 4250 (1996).

[230] B. Koopmans, M. van Kampen, and W. J. M. de Jonge, "Experimental access to femtosecond spin dynamics", J. Phys.: Condens. Mat. **15**, S723 (2003).

[231] S. Michalski, J. Zhou, R. Skomski, and R. D. Kirby, "Coupled precession modes in indirect exchange-coupled [Pt/Co]–Co thin films", J. Appl. Phys. **101**, 09D115 (2007).

[232] S. Mizukami, D. Watanabe, T. Kubota, X. Zhang, H. Naganuma, M. Oogane, Y. Ando, and T. Miyazaki, "Laser-Induced Fast Magnetization Precession and Gilbert Damping for CoCrPt Alloy Thin Films with Perpendicular Magnetic Anisotropy", Appl. Phys. Express **3**, 123001 (2010).

[233] C. Bunce, J. Wu, G. Ju, B. Lu, D. Hinzke, N. Kazantseva, U. Nowak, and R. W. Chantrell, "Laser-induced magnetization switching in films with perpendicular anisotropy: A comparison between measurements and a multi-macrospin model", Phys. Rev. B **81**, 174428 (2010).

[234] S. Mizukami, E. P. Sajitha, D. Watanabe, F. Wu, T. Miyazaki, H. Naganuma, M. Oogane, and Y. Ando, "Gilbert damping in perpendicularly magnetized Pt/Co/Pt films investigated by all-optical pump-probe technique", Appl. Phys. Lett. **96**, 152502 (2010).

[235] S. Mizukami, S. Iihama, N. Inami, T. Hiratsuka, G. Kim, H. Naganuma, M. Oogane, and Y. Ando, "Fast magnetization precession observed in $L1_0$-FePt epitaxial thin film", Appl. Phys. Lett. **98**, 052501 (2011).

[236] M. van Kampen, "Ultrafast spin dynamics in ferromagnetic metals", Ph.D. thesis, Technische Universiteit Eindhoven (2003).

[237] M. van Kampen, C. Jozsa, J. T. Kohlhepp, P. LeClair, L. Lagae, W. J. M. de Jonge, and B. Koopmans, "All-Optical Probe of Coherent Spin Waves", Phys. Rev. Lett. **88**, 227201 (2002).

[238] G. Woltersdorf, "Spin-Pumping and Two-Magnon Scattering In Magnetic Multilayers", Ph.D. thesis, Simon Fraser University (2004).

[239] P. S. Keatley, "Time-Resolved Magneto-Optical Investigations of Picosecond Magnetisation Dynamics in Arrays of Non-Ellipsoidal Ferromagnetic Nano-Elements", Ph.D. thesis, University of Exeter (2008).

[240] A. Kirilyuk, A. V. Kimel, and T. Rasing, "Ultrafast optical manipulation of magnetic order", Rev. Mod. Phys. **82**, 2731 (2010).

[241] T. J. Silva, C. S. Lee, T. M. Crawford, and C. T. Rogers, "Inductive measurement of ultrafast magnetization dynamics in thin-film Permalloy", J. Appl. Phys. **85**, 7849 (1999).

[242] J. Walowski, M. D. Kaufmann, B. Lenk, C. Hamann, J. McCord, and M. Münzenberg, "Intrinsic and non-local Gilbert damping in polycrystalline nickel studied by Ti : sapphire laser fs spectroscopy", J. Phys. D: Appl. Phys. **41**, 164016 (2008).

[243] M. van Kampen, B. Koopmans, J. T. Kohlhepp, and W. J. M. de Jonge. "Laser-induced precession in canted-spin ferromagnets. In *4th International Symposium on Metallic Multilayers*, volume 240, page 291 (2002).

[244] G. Malinowski, K. C. Kuiper, R. Lavrijsen, H. J. M. Swagten, and B. Koopmans, "Magnetization dynamics and Gilbert damping in ultrathin $Co_{48}Fe_{32}B_{20}$ films with out-of-plane anisotropy", Appl. Phys. Lett. **94**, 102501 (2009).

[245] M. Djordjevic, G. Eilers, A. Parge, M. Münzenberg, and J. S. Moodera, "Intrinsic and nonlocal Gilbert damping parameter in all optical pump-probe experiments", J. Appl. Phys. **99**, 08F308 (2006).

[246] S. Foner, "Vibrating Sample Magnetometer", Rev. Sci. Instrum. **27**, 548 (1956).

[247] S. Foner, "The vibrating sample magnetometer: Experiences of a volunteer (invited)", J. Appl. Phys. **79**, 4740 (1996).

[248] S. R. Hoon, "An inexpensive, sensitive vibrating sample magnetometer", Eur. J. Phys. **4**, 61 (1983).

[249] E. O. Samwel, T. Bolhuis, and J. C. Lodder, "An alternative approach to vector vibrating sample magnetometer detection coil setup", Rev. Sci. Instrum. **69**, 3204 (1998).

[250] M. Eisterer, F. Hengstberger, C. S. Voutsinas, N. Horhager, S. Sorta, J. Hecher, and H. W. Weber, "Rotating sample magnetometer for cryogenic temperatures and high magnetic fields", Rev. Sci. Instrum. **82**, 063902 (2011).

[251] A. W. Pacyna, "General theory of the signal induced in a vibrating magnetometer", J. Phys. E: Sci. Instrum. **15**, 663 (1982).

[252] A. W. Pacyna and K. Ruebenbauer, "General theory of a vibrating magnetometer with extended coils", J. Phys. E: Sci. Instrum. **17**, 141 (1984).

[253] J. Clarke and A. I. Braginski, "The SQUID Handbook: Fundamentals and Technology of SQUIDs and SQUID Systems", volume 1, first edition, Wiley-VCH GmbH, Weinheim (2004).

[254] J. Clarke and A. I. Braginski, editors, "The SQUID Handbook: Applications", volume 2, first edition, Wiley-VCH, Weinheim (2006).

[255] B. D. Josephson, "Possible new effects in superconductive tunnelling", Phys. Lett. **1**, 251 (1962).

[256] B. D. Josephson, "The discovery of tunnelling supercurrents", Rev. Mod. Phys. **46**, 251 (1974).

[257] G. Binnig, C. F. Quate, and C. Gerber, "Atomic Force Microscope", Phys. Rev. Lett. **56**, 930 (1986).

[258] F. J. Giessibl, S. Hembacher, H. Bielefeldt, and J. Mannhart, "Subatomic Features on the Silicon (111)-(7×7) Surface Observed by Atomic Force Microscopy", Science **289**, 422 (2000).

[259] A. de Lozanne, "You May Squeeze the Atoms But Don't Mangle the Surface!", Science **291**, 2561 (2001).

[260] R. V. Lapshin, "Feature-oriented scanning methodology for probe microscopy and nanotechnology", Nanotechnology **15**, 1135 (2004).

[261] Q. Zhong, D. Inniss, K. Kjoller, and V. B. Elings, "Fractured polymer/silica fiber surface studied by tapping mode atomic force microscopy", Surf. Sci. Lett. **290**, L688 (1993).

[262] N. A. Geisse, "AFM and combined optical techniques", Mater. Today **12**, 40 (2009).

[263] R. W. Carpick and M. Salmeron, "Scratching the Surface: Fundamental Investigations of Tribology with Atomic Force Microscopy", Chem. Rev. **97**, 1163 (1997).

[264] Y. Martin and H. K. Wickramasinghe, "Magnetic imaging by "force microscopy" with 1000 Å resolution.", Appl. Phys. Lett. **50**, 1455 (1987).

[265] R. D. Gomez, E. R. Burke, and I. D. Mayergoyz, "Magnetic imaging in the presence of external fields: Technique and applications (invited)", J. Appl. Phys. **79**, 6441 (1996).

[266] U. Hartmann, "Magnetic Force Microscopy", Annu. Rev. Mater. Sci. **29**, 53 (1999).

[267] L. Gao, L. Yue, T. Yokota, R. Skomski, S. Liou, H. Takahoshi, H. Saito, and S. Ishio, "Focused ion beam milled CoPt magnetic force microscopy tips for high resolution domain images", IEEE Trans. Magn. **40**, 2194 (2004).

[268] L. Abelmann, S. Porthun, M. Haast, C. Lodder, A. Moser, M. E. Best, P. J. van Schendel, B. Stiefel, H. J. Hug, G. P. Heydon, A. Farley, S. R. Hoon, T. Pfaffelhuber, R. Proksch, and K. Babcock, "Comparing the resolution of magnetic force microscopes using the CAMST reference samples", J. Magn. Magn. Mater. **190**, 135 (1998).

[269] J. Goldstein, D. E. Newbury, D. C. Joy, C. E. Lyman, P. Echlin, E. Lifshin, L. Sawyer, and J. R. Michael, "Scanning Electron Microscopy and X-ray Microanalysis", third correction, second printing edition, Springer, Berlin (2007).

[270] D. B. Williams and C. B. Carter, "Transmission Electron Microscopy: A Textbook for Materials Science", second edition, Springer, Berlin (2009).

[271] B. Fultz and J. M. Howe, "Transmission Electron Microscopy and Diffractometry of Materials", third, second printing edition, Springer, Berlin (2007).

[272] R. A. Shaw, A. B. Kostinski, and M. L. Larsen, "Towards quantifying droplet clustering in clouds", Q. J. Roy. Meteor. Soc. **128**, 1043 (2002).

[273] L. D. Landau and E. M. Lifshitz, "Statistical Physics", volume 5 of *Course of Theoretical Physics*, third edition, Butterworth-Heinemann, Oxford (1980).

[274] R. Böttger, L. Bischoff, S. Facsko, and B. Schmidt, "Quantitative analysis of the order of Bi ion induced dot patterns on Ge", Europhys. Lett. **98**, 16009 (2012).

[275] E. Takeshi, , and S. J. L. Billinge, "Underneath the Bragg Peaks, Structural Analysis of Complex Materials", volume 16 of *Pergamon Materials Series*, first edition, Pergamon, Elsevier, Oxford (2003).

[276] J. Hua, Y. Liu, and Z. Zhang, "Analysis of a 2D "liquid" plasma lattice", Sci. China Ser. G **47**, 129 (2004).

[277] F. Kaatz, A. Bultheel, and T. Egami, "Order parameters from image analysis: a honeycomb example", Naturwissenschaften **95**, 1033 (2008).

[278] K. Rook, A. M. Zeltser, J. O. Artman, D. E. Laughlin, M. H. Kryder, and R. M. Chrenko, "Multilayer Permalloy films grown by molecular-beam epitaxy", J. Appl. Phys. **69**, 5670 (1991).

[279] K. Zakeri Lori, "Magnetic monolayers on semiconducting substrates: an in situ FMR study of Fe-based heterostructures", Ph.D. thesis, Universität Duisburg-Essen (2007).

[280] K. Zakeri, J. Lindner, I. Barsukov, R. Meckenstock, M. Farle, U. von Horsten, H. Wende, W. Keune, J. Rocker, S. S. Kalarickal, K. Lenz, W. Kuch, K. Baberschke, and Z. Frait, "Spin dynamics in ferromagnets: Gilbert damping and two-magnon scattering", Phys. Rev. B **76**, 104416 (2007).

[281] M. L. Schneider, J. M. Shaw, A. B. Kos, T. Gerrits, T. J. Silva, and R. D. McMichael, "Spin dynamics and damping in nanomagnets measured directly by frequency-resolved magneto-optic Kerr effect", J. Appl. Phys. **102**, 103909 (2007).

[282] R. Urban, G. Woltersdorf, and B. Heinrich, "Gilbert Damping in Single and Multilayer Ultrathin Films: Role of Interfaces in Nonlocal Spin Dynamics", Phys. Rev. Lett. **87**, 217204 (2001).

[283] J. P. Nibarger, R. Lopusnik, and T. J. Silva, "Damping as a function of pulsed field amplitude and bias field in thin film Permalloy", Appl. Phys. Lett. **82**, 2112 (2003).

[284] M. L. Schneider, T. Gerrits, A. B. Kos, and T. J. Silva, "Gyromagnetic damping and the role of spin-wave generation in pulsed inductive microwave magnetometry", Appl. Phys. Lett. **87**, 072509 (2005).

[285] M. L. Schneider, T. Gerrits, A. B. Kos, and T. J. Silva, "Experimental determination of the inhomogeneous contribution to linewidth in Permalloy films using a time-resolved magneto-optic Kerr effect microprobe", J. Appl. Phys. **102**, 053910 (2007).

[286] D. Makarov, C. Brombacher, F. Liscio, M. Maret, M. Parlinska, S. Meier, P. Kappenberger, and M. Albrecht, "FePt films on self-assembled SiO_2 particle arrays", J. Appl. Phys. **103**, 053903 (2008).

[287] D. Makarov, E. Bermudez-Urena, O. G. Schmidt, F. Liscio, M. Maret, C. Brombacher, S. Schulze, M. Hietschold, and M. Albrecht, "Nanopatterned CoPt alloys with perpendicular magnetic anisotropy", Appl. Phys. Lett. **93**, 153112 (2008).

[288] D. Makarov, F. Klimenta, S. Fischer, F. Liscio, S. Schulze, M. Hietschold, M. Maret, and M. Albrecht, "Nonepitaxially grown nanopatterned Co–Pt alloys with out-of-plane magnetic anisotropy", J. Appl. Phys. **106**, 114322 (2009).

[289] R. Streubel, D. Makarov, F. Kronast, V. Kravchuk, M. Albrecht, and O. G. Schmidt, "Magnetic vortices on closely packed spherically curved surfaces", Phys. Rev. B **85**, 174429 (2012).

[290] E. Feldtkeller and H. Thomas, "Struktur und Energie von Blochlinien in dünnen ferromagnetischen Schichten", Z. Phys. B: Condens. Mat. **4**, 8 (1965).

[291] R. Ranjan, M. S. Miller, P. K. George, and M. Lu. "Magnetic, recording, and crystalline properties of multilayered longitudinal thin-film media. In *J. Appl. Phys.*, volume 69, page 4727. AIP (1991).

[292] T. P. Nolan, Y. Hirayama, and M. Futamoto. "Improvement of $Co_{71}Cr_{19}Pt_{10}/Ti_{90}Cr_{10}$ perpendicular recording media by independent optimization of film nucleation and growth processes. In *J. Appl. Phys.*, volume 79, page 5359. AIP (1996).

[293] S. N. Piramanayagam, "Perpendicular recording media for hard disk drives", J. Appl. Phys. **102**, 011301 (2007).

[294] S. H. Park, S. O. Kim, H. S. Oh, S. H. Choa, and T. D. Lee, "Grain size reduction of $CoCrPt:SiO_2$ media by oxidation of RuCr intermediate layer grain boundary", Phys. Stat. Sol. C **4**, 4516 (2007).

[295] Y. Song and D. Zhu, editors, "High Density Data Storage, Principle, Technology, and Materials", volume 1, World Scientific Publishing, Singapore (2009).

[296] R. Wood, "Future hard disk drive systems", J. Magn. Magn. Mater. **321**, 555 (2009).

[297] B. A. Gurovich, K. E. Prikhodko, E. A. Kuleshova, A. Yu Yakubovsky, E. Z. Meilikhov, and M. G. Mosthenko, "Magnetic properties of high-density patterned magnetic media", J. Magn. Magn. Mater. **322**, 3060 (2010).

[298] B. C. Stipe, T. C. Strand, C. C. Poon, H. Balamane, T. D. Boone, J. A. Katine, J.-L. Li, V. Rawat, H. Nemoto, A. Hirotsune, O. Hellwig, R. Ruiz, E. Dobisz, D. S. Kercher, N. Robertson, T. R. Albrecht, and B. D. Terris, "Magnetic recording at 1.5 Pb m^{-2} using an integrated plasmonic antenna", Nat. Photon. **4**, 484 (2010).

[299] Y. Sonobe, H. Muraoka, K. Miura, Y. Nakamura, K. Takano, H. Do, A. Moser, B. K. Yen, Y. Ikeda, and N. Supper. "Coupled granular/continuous perpendicular recording media with soft magnetic underlayer. In *J. Appl. Phys.*, volume 91, page 8055 (2002).

[300] S. Kumar, T. Ohkubo, and D. E. Laughlin. "HITPERM soft magnetic underlayers for perpendicular thin film media. In *J. Appl. Phys.*, volume 91, page 8360 (2002).

[301] A. G. Roy and D. E. Laughlin, "Effect of seed layers in improving the crystallographic texture of CoCrPt perpendicular recording media", J. Appl. Phys. **91**, 8076 (2002).

[302] J. Shi, S. Piramanayagam, S. Chow, J. Zhao, and C. Mah. "$CoCrPt-SiO_2$ Perpendicular Recording Media with a Crystalline Soft Underlayer. In *Magnetics Conference, 2006. INTERMAG 2006. IEEE International*, page 622 (2006).

[303] J. Shi, S. Piramanayagam, S. Chow, S. Wang, J. Zhao, and C. Mah, "$CoCrPt-SiO_2$ Perpendicular Recording Media With a Crystalline Soft Underlayer", IEEE Trans. Magn. **42**, 2369 (2006).

[304] S. Piramanayagam, J. Shi, C. Mah, and J. Zhang. "A Novel Perpendicular Recording Medium with a Magnetic Intermediate Layer. In *Magnetics Conference, 2006. INTERMAG 2006. IEEE International*, page 632 (2006).

[305] J. Shi, S. Piramanayagam, J. Zhao, C. Mah, Y. Kay, and C. Ong, "Low-Noise Crystalline Soft Underlayer for $CoCrPt:SiO_2$ Perpendicular Recording Media", IEEE Trans. Magn. **43**, 2100 (2007).

[306] H. S. Jung, U. Kwon, M. Kuo, E. M. T. Velu, S. S. Malhotra, W. Jiang, and G. Bertero, "Effect of Oxygen Incorporation on Microstructure and Media Performance in $CoCrPt-SiO_2$ Perpendicular Recording Media", IEEE Trans. Magn. **43**, 615 (2007).

[307] S. Yumoto and N. Ohshima, "A study of the structural properties of sputtered CoCrPt based on x-ray diffraction, small angle x-ray scattering, XAFS, and transmission electron microscopy measurements", J. Appl. Phys. **75**, 6160 (1994).

[308] S. Yumoto and N. Ohshima, "Study on sputtering power dependence of the structural properties of sputtered CoCrPt", J. Appl. Phys. **77**, 2321 (1995).

[309] Y. Xu, J. P. Wang, C. K. Pock, C. Xiaomin, Z. S. Shan, and T. C. Chong, "Controlling the preferred orientation in granular CoCrPt:C thin films for high-areal density magnetic recording", IEEE Trans. Magn. **37**, 1491 (2001).

[310] Y. Xu, Z. S. Shan, J. P. Wang, and C. T. Chong, "Magnetic and reversal properties of HCP-CoCrPt: C granular films with CrTi underlayer", J. Magn. Magn. Mater. **232**, 103 (2001).

[311] Y. Xu, J. P. Wang, Z. S. Shan, H. Jiang, Y. S., C. T. Chong, and L. Lu, "Structural and magnetic properties of $HCP-CoCrPt-SiO_2$ granular media", J. Magn. Magn. Mater. **225**, 359 (2001).

[312] M. Shima and C. A. Ross, "Development of microstructure in Cr and Cr/CoCrPt films made by pulsed laser deposition", J. Appl. Phys. **93**, 945 (2003).

[313] J. H. Judy, "Advancements in PMR thin-film media", J. Magn. Magn. Mater. **287**, 16 (2005).

[314] S. N. Piramanayagam, H. B. Zhao, J. Z. Shi, and C. S. Mah, "Palladium-based intermediate layers for $CoCrPt–SiO_2$ perpendicular recording media", Appl. Phys. Lett. **88**, 092506 (2006).

[315] W. Shen, A. Das, M. Racine, R. Cheng, J. H. Judy, and J. Wang. "Magnetic Anisotropy Enhancement for hcp Structured Co Alloy Thin Films through Pt Doping. In *Magnetics Conference, 2006. INTERMAG 2006. IEEE International*, page 171 (2006).

[316] A. Vogel, S. Wintz, J. Kimling, M. Bolte, T. Strache, M. Fritzsche, M.-Y. Im, P. Fischer, G. Meier, and J. Fassbender, "Domain-Wall Pinning and Depinning at Soft Spots in Magnetic Nanowires", IEEE Trans. Magn. **46**, 1708 (2010).

[317] A. Vogel, S. Wintz, T. Gerhardt, L. Bocklage, T. Strache, M.-Y. Im, P. Fischer, J. Fassbender, J. McCord, and G. Meier, "Field- and current-induced domain-wall motion in permalloy nanowires with magnetic soft spots", Appl. Phys. Lett. **98**, 202501 (2011).

[318] D. Watanabe, S. Mizukami, M. Oogane, H. Naganuma, Y. Ando, and T. Miyazaki. "Fabrication of MgO-based magnetic tunnel junctions with CoCrPt perpendicularly magnetized electrodes. In *J. Appl. Phys.*, volume 105, page 07C911. AIP (2009).

[319] N. Inaba, Y. Uesaka, and M. Futamoto, "Compositional and temperature dependence of basic magnetic properties of CoCr-alloy thin films", IEEE Trans. Magn. **36**, 54 (2000).

[320] H. S. Jung, E. M. T. Velu, S. S. Malhotra, G. Bertero, and U. Kwon, "Comparison of media properties between hard/soft stacked composite and capping layer perpendicular recording media", J. Magn. Magn. Mater. **320**, 3151 (2008).

[321] T. W. Clinton, N. Benatmane, J. Hohlfeld, and E. Girt. "Comparison of a near-field ferromagnetic resonance probe with pump-probe characterization of CoCrPt media. In *J. Appl. Phys.*, volume 103, page 07F546. AIP (2008).

[322] M. Igarashi, T. Kambe, K. Yoshida, Y. Hosoe, and Y. Sugita. "A method of measuring anisotropy field of polycrystalline thin-film media. In *J. Appl. Phys.*, volume 85, pages 4720–4722 (1999).

[323] N. Inaba, H. Asanuma, S. Igarashi, S. Mori, F. Kirino, K. Koike, and H. Morita, "Damping Constants of Ni-Fe and Ni-Co Alloy Thin Films", IEEE Trans. Magn. **42**, 2372 (2006).

[324] S. Mizukami, D. Watanabe, T. Kubota, X. Zhang, H. Naganuma, M. Oogane, Y. Ando, and T. Miyazaki, "Time-Resolved Kerr Effect in Very Thin Films of CoCrPt Alloys", IEEE Trans. Magn. **47**, 3897 (2011).

[325] J. Fassbender, D. Ravelosona, and Y. Samson, "Tailoring magnetism by light-ion irradiation", J. Phys. D: Appl. Phys. **37**, R179 (2004).

[326] J. Fassbender and J. McCord, "Control of saturation magnetization, anisotropy, and damping due to Ni implantation in thin $Ni_{81}Fe_{19}$ layers", Appl. Phys. Lett. **88**, 252501 (2006).

[327] J. Fassbender and J. McCord, "Magnetic patterning by means of ion irradiation and implantation", J. Magn. Magn. Mater. **320**, 579 (2008).

[328] A. Maziewski, P. Mazalski, Z. Kurant, M. Liedke, J. McCord, J. Fassbender, J. Ferré, A. Mougin, A. Wawro, L. T. Baczewski, A. Rogalev, F. Wilhelm, and T. Gemming, "Tailoring of magnetism in Pt/Co/Pt ultrathin films by ion irradiation", Phys. Rev. B **85**, 054427 (2012).

[329] M. Martín-González, F. Briones, J. García-Martín, J. Montserrat, L. Vila, G. Faini, A. Testa, D. Fiorani, and H. Rohrmann, "Nano-patterning of perpendicular magnetic recording media by low-energy implantation of chemically reactive ions", J. Magn. Magn. Mater. **322**, 2762 (2010).

[330] S. N. Piramanayagam and K. Srinivasan, "Stacked CoCrPt:SiO$_2$ Layers for perpendicular recording media", J. Magn. Magn. Mater. **321**, 485 (2009).

[331] S. N. Piramanayagam, J. Z. Shi, C. K. Pock, H. B. Zhao, C. S. Mah, Y. S. Kay, J. Zhang, J. R. Shi, and J. M. Zhao, "Recording media research for future hard disk drives", Thin Solid Films **505**, 71 (2006).

[332] S. N. Piramanayagam, J. Z. Shi, H. B. Zhao, C. S. Mah, and J. Zhang, "Investigations on nano-structured perpendicular recording media for high density data storage", IEEE Trans. Magn. **41**, 3190 (2005).

[333] C. Chappert, H. Bernas, J. Ferre, V. Kottler, J.-P. Jamet, Y. Chen, E. Cambril, T. Devolder, F. Rousseaux, V. Mathet, and H. Launois, "Planar Patterned Magnetic Media Obtained by Ion Irradiation", Science **280**, 1919 (1998).

[334] G. L. W. Cross, "The production of nanostructures by mechanical forming", J. Phys. D: Appl. Phys. **39**, R363 (2006).

[335] Y. Hirayama, I. Tamai, I. Takekuma, and R. Nakatani, "Role of underlayer for segregated structure formation of CoCrPt-SiO$_2$ granular thin film", J. Phys.: Conf. Ser. **165**, 012033 (2009).

[336] K. Srinivasan, S. N. Piramanayagam, R. Sbiaa, and R. W. Chantrell, "Microstructure and switching mechanism of stacked CoCrPt:SiO$_2$ perpendicular recording media", J. Magn. Magn. Mater. **320**, 3041 (2008).

[337] K. Srinivasan, S. N. Piramanayagam, R. W. Chantrell, and Y. S. Kay, "Thermal stability and the magnetization process in CoCrPt:SiO$_2$ perpendicular recording media", J. Magn. Magn. Mater. **320**, 3036 (2008).

[338] J. D. Dutson, M. Hashimoto, Y. Inaba, S. J. Greaves, H. Muraoka, and K. O'Grady, "Magnetic and Recording Properties of $(CoCrPt)_{1-x}(SiO_2)_x$ Media", IEEE Trans. Magn. **43**, 814 (2007).

[339] S. Günther. "Kobalt-Platin-Multilagen auf vorstrukturierten Substraten. Master's thesis, Technische Universität Chemnitz (2011).

[340] E. C. Stoner and E. P. Wohlfarth, "A mechanism of magnetic hysteresis in heterogeneous alloys", IEEE Trans. Magn. **27**, 3475 (1991).

[341] J. W. Lau, R. D. McMichael, S. H. Chung, J. O. Rantschler, V. Parekh, and D. Litvinov, "Microstructural origin of switching field distribution in patterned Co/Pd multilayer nanodots", Appl. Phys. Lett. **92**, 012506 (2008).

[342] D. Makarov, S. Tibus, C. T. Rettner, T. Thomson, B. D. Terris, T. Schrefl, and M. Albrecht, "Magnetic strip patterns induced by focused ion beam irradiation", J. Appl. Phys. **103**, 063915 (2008).

[343] O. Hellwig, T. Hauet, T. Thomson, E. Dobisz, J. D. Risner-Jamtgaard, D. Yaney, B. D. Terris, and E. E. Fullerton, "Coercivity tuning in Co/Pd multilayer based bit patterned media", Appl. Phys. Lett. **95**, 232505 (2009).

[344] C. Teichert, "Self-organized semiconductor surfaces as templates for nanostructured magnetic thin films", Appl. Phys. A-Mater. **76**, 653 (2003).

[345] C. T. Rettner, S. Anders, J. E. E. Baglin, T. Thomson, and B. D. Terris, "Characterization of the magnetic modification of Co/Pt multilayer films by He$^+$, Ar$^+$, and Ga$^+$ ion irradiation", Appl. Phys. Lett. **80**, 279 (2002).

[346] T. Hauet, O. Hellwig, S.-H. Park, C. Beigne, E. Dobisz, B. D. Terris, and D. Ravelosona, "Influence of ion irradiation on switching field and switching field distribution in arrays of Co/Pd-based bit pattern media", Appl. Phys. Lett. **98**, 172506 (2011).

[347] T. C. Ulbrich, D. Makarov, G. Hu, I. L. Guhr, D. Suess, T. Schrefl, and M. Albrecht, "Magnetization Reversal in a Novel Gradient Nanomaterial", Phys. Rev. Lett. **96**, 077202 (2006).

[348] T. Eimüller, T. C. Ulbrich, E. Amaladass, I. L. Guhr, T. Tyliszczak, and M. Albrecht, "Spin-reorientation transition in Co/Pt multilayers on nanospheres", Phys. Rev. B **77**, 134415 (2008).

[349] T. C. Ulbrich, D. Assmann, and M. Albrecht, "Magnetic properties of Co/Pt multilayers on self-assembled particle arrays", J. Appl. Phys. **104**, 084311 (2008).

[350] T. C. Ulbrich, C. Bran, D. Makarov, O. Hellwig, J. D. Risner-Jamtgaard, D. Yaney, H. Rohrmann, V. Neu, and M. Albrecht, "Effect of magnetic coupling on the magnetization reversal in arrays of magnetic nanocaps", Phys. Rev. B **81**, 054421 (2010).

[351] J. K. n. Moser, V. Kunej, H.-F. Pernau, E. Scheer, and M. Albrecht, "Magnetoresistive effects in Co/Pd multilayers on self-assembled nanoparticles (invited)", J. Appl. Phys. **107**, 09C506 (2010).

[352] J. Fidler, T. Schrefl, D. Suess, O. Ertl, M. Kirschner, and G. Hrkac, "Full micromagnetics of recording on patterned media", Phys. B: Condens. Mat. **372**, 312 (2006).

[353] P. Kappenberger, F. Luo, L. J. Heyderman, H. H. Solak, C. Padeste, C. Brombacher, D. Makarov, T. V. Ashworth, L. Philippe, H. J. Hug, and M. Albrecht, "Template-directed self-assembled magnetic nanostructures for probe recording", Appl. Phys. Lett. **95**, 023116 (2009).

[354] P. F. Carcia, "Perpendicular magnetic anisotropy in Pd/Co and Pt/Co thin-film layered structures", J. Appl. Phys. **63**, 5066 (1988).

[355] W. B. Zeper, H. W. van Kesteren, B. A. J. Jacobs, J. H. M. Spruit, and P. F. Carcia, "Hysteresis, microstructure, and magneto-optical recording in Co/Pt and Co/Pd multilayers", J. Appl. Phys. **70**, 2264 (1991).

[356] J. Šimšová, R. Gemperle, V. Kamberský, S. Porthun, P. de Haan, and C. Lodder, "Domain structure of Co/Pd multilayers", IEEE Trans. Magn. **30**, 784 (1994).

[357] K. Lenz, "Magnetische Anisotropie und Dämpfungsmechanismen in ultradünnen 3d-Ferromagneten. Eine FMR-Studie", Ph.D. thesis, Freie Universität Berlin (2005).

[358] M. Farle, "Ferromagnetic resonance of ultrathin metallic layers", Rep. Prog. Phys. **61**, 755 (1998).

[359] P. C. Scholten. "Which SI? In *Proceedings of the Seventh International Conference on Magnetic Fluids*, volume 149, page 57 (1995).

Publications

Articles

- **D. K. Ball**, S. Günther, M. Fritzsche, K. Lenz, G. Varvaro, D. Makarov, A. Mücklich, S. Facsko, M. Albrecht, and J. Fassbender, ”*Morphology-induced magnetic properties of [Co/Pd] multilayers grown on arrays of GaSb nanocones*”, in submission.
- P. Krone, C. Brombacher, D. Makarov, K. Lenz, **D. K. Ball**, F. Springer, H. Rohrmann, J. Fassbender, and M. Albrecht, ”*Nanocap arrays of granular CoCrPt:SiO$_2$ films on silica particles: tailoring of the magnetic properties by Co$^+$ irradiation*”, Nanotechnology 38, **21** (2010), 385703 (7pp), `DOI:10.1088/0957-4484/21/38/385703`.
- M. Piantek, J. Miguel, A. Krüger, C. Navió, M. Bernien, **D. K. Ball**, K. Hermann and W. Kuch, ”*Temperature, Surface, and Coverage-Induced Conformational Changes of Azobenzene Derivatives on Cu(001)*”, J. Phys. Chem. C 113, **47**, pp. 20307-20315 (2009), `DOI:10.1021/jp907641f`.

Talks

- **D. K. Ball**, M. Fritzsche, J. Osten, K. Lenz, S. Facsko, A. Mücklich, and J. Fassbender, ”*Tailoring the magnetic damping and anisotropy of Permalloy deposited on GaSb nanocones.*”, nominated talk for the ”Best student presentation award” by the IEEE Magnetic Society at the Intermag 2012, IEEE International Magnetic Conference, 05/08/2012, Vancouver, Canada.
- **D. K. Ball**, Michael Körner, Monika Fritzsche, T. Strache, P. Krone, S. Tibus, A. Mücklich, D. Makarov, K. Lenz, M. Albrecht, and J. Fassbender, ”*Investigating the Magnetic Properties of Tailored Bit Patterned Media Using Ferromagnetic Resonance.*”, invited talk at the group seminar in the group of Prof. Dr. Dirk Grundler TU Munich, 06/09/2010, Munich, Germany.

Posters

- **D. K. Ball**, S. Günther, M. Fritzsche, G. Varvaro, D. Makarov, K. Lenz, J. Fassbender, and M. Albrecht, ”*Magnetic properties of granular CoCrPt:SiO$_2$ recording media deposited on GaSb nanocones.*”, IEEE International Magnetic Conference Intermag 2011, 05/26/2011, Taipei, Taiwan (Student travel grant awarded from the IEEE Magnetic society).
- **D. K. Ball**, S. Günther, M. Fritzsche, G. Varvaro, D. Makarov, K. Lenz, J. Fassbender, and M. Albrecht, ”*Granular CoCrPt:SiO$_2$ recording media on assemblies of GaSb nanocones.*”, 75th Annual Meeting of the DPG and DPG Spring Meeting, 03/15/2011, Dresden, Germany.
- **D. K. Ball**, M. O. Liedke, K. Lenz, R. Yilgin, M. Fritzsche, A. Keller, S. Facsko, and J. Fassbender, ”*Magnetic Anisotropy of Thin Magnetic Films on Nanometer Scale Silicon Ripples.*”, Nanofair 2012 - 9$^{\text{th}}$ International Nanotechnology Symposium, 07/06/2010, Dresden, Germany.
- **D. K. Ball**, M. Bernien, M. Piantek, J. Kurde, M. Haryono, S. Hain, A. Grohmann, H. Wende and W. Kuch, ”*X-ray absorption spectroscopy of spin-crossover complexes on metallic surfaces.*”, 72. Annual Meeting of the DPG and DPG Spring Meeting of the Condensed Matter Division, 02/26/2011, Berlin, Germany.

Acknowledgements

First of all, I want to thank both the referees of my doctoral thesis, Prof. Dr. Jürgen Fassbender[1,2] and Prof. Dr. Manfred Albrecht[3].

Moreover, I want to thank Prof. Dr. Jürgen Fassbender[1,2], for giving me the opportunity to research and write this doctoral thesis and also for his interest and support of my work.

Furthermore, I want to thank my supervisor and friend Dr. Kilian Lenz[1] for his extensive support of my doctoral thesis, as well as for creating a stimulating atmosphere in his junior research group "Magnetization Dynamics".

Also I want to thank everyone who contributed to this work in terms of sample preparations, additional measurements, simulations, discussions, and any other kinds of support. In particular I would like to thank:

- The Team
    - Dr. Christopher Bunce[1]
    - Dr. Jürgen Lindner[1]
    - Dr. Stefan Facsko[1]
    - Dr. Volker Sluka[1]
    - Dr. Alina Deac[1]
    - Dr. Ciaran Fowley[1]
    - Dr. Andreas Neudert[1]
    - Dr. Rantej Bali[1]
    - Dr. Christine Baumgart[1]
    - Dr. Adrian Keller[1]
    - Dr. Daniel Markó[1]
    - Dr. Arndt Mücklich[1]
    - Dr. Mykhaylo Ozerov [1]
    - Dr. Sergei Zvyagin[1]
    - Michael Körner[1,2]
    - Julia Osten[1,2]
    - Monika Fritzsche[1,2]
    - Sebastian Wintz[1,2]
    - Anja Banholzer[1]
    - Thomas Strache[1]
    - Kerstin Bernert[1]
    - Matthias Wieser[1,2]
    - Manuel Langer[1]
    - Andreas Henschke[1]

- The Cooperation Partners:
    - Dr. Denys Makarov[4]
    - Dr. Olav Hellwig[5]
    - Dr. Gaspare Varvaro[6]
    - Dr. Stefan Tibus[7]
    - Dr. Philipp Krone[3]
    - Stefan Günther[3]

In addition, I would like to remark on the enjoyable and cooperative atmosphere within the FWIN division which was a great pleasure.

And last but not least my family, Mirjam and Joshua.

---

[1]Institute of Ion Beam Physics and Materials Research, Helmholtz-Zentrum Dresden-Rossendorf e.V., P.O. Box 510119, 01314 Dresden, Germany

[2]Institute for Physics of Solids, TU Dresden, Zellescher Weg 16, 01069 Dresden, Germany

[3]Institut für Physik, TU Chemnitz, 09107 Chemnitz, Germany

[4]Leibniz Institute for Solid State and Materials Research Dresden, Helmholtzstraße 20, 01069 Dresden, Germany

[5]San Jose Research Centre, HGST, a Western Digital Company, 3403 Yerba Buena Road, San Jose, CA 95135, USA

[6]Institute of Structure of Matter, National Research Council, 00016 Monterotondo Scalo, Roma, Italy

[7]University Konstanz, 78457 Konstanz, Germany

Erklärung

Diese Dissertation wurde am Institut für Ionenstrahlphysik und Materialforschung des Helmholtz-Zentrums Dresden–Rossendorf e.V. unter der wissenschaftlichen Betreuung von Prof. Dr. Jürgen Faßbender angefertigt.

Hiermit versichere ich, dass ich die vorliegende Arbeit ohne unzulässige Hilfe Dritter und ohne Benutzung anderer, als der angegebenen Hilfsmittel angefertigt habe; die aus fremden Quellen direkt oder indirekt übernommenen Gedanken sind als solche kenntlich gemacht. Die Arbeit wurde bisher weder im Inland noch im Ausland in gleicher oder ähnlicher Form einer anderen Prüfungsbehörde vorgelegt.

Ich versichere weiterhin, dass bislang keine Promotionsverfahren stattgefunden haben.

Ich erkenne die Promotionsordnung der Fakultät Mathematik und Naturwissenschaften an der Technischen Universität Dresden vom 23.02.2011 an.

Dresden, April 29, 2013

David Klaus Ball